ORIGINAL: ENGLISH

GARTEUR TP–198

April 2024

CLASSIFICATION: OPEN

GARTEUR AD/AG-59
IMOLA: Improving the MOdelling of LAminar separation bubbles

P. Catalano[1], D. de Rosa[1], M. Miozzi[2], S. Hein[3], J. A. Franco[3], F. Tocci[3], V. D'Alessandro[4], L. Bernardos[5], G. Delattre[5], R. Tognaccini[6], Z. Hu[7], Y. Hoarau[8], A. Marouf[8], M. Righi[8]

[1]CIRA, [2]CNR-INM, [3]DLR, [4]Marche Polytechnic University, [5]ONERA, [6]University of Napoli "Federico II", [7]University of Southampton, [8]University of Strasbourg

GARTEUR aims at stimulating and co-ordinating co-operation between
Research Establishments and Industry in the areas of Aerodynamics,
Flight Mechanics, Systems and Integration, Helicopters and Structures & Materials.

Contents

1 Introduction

Aerodynamic performances of aerial vehicles are largely influenced by the Reynolds number. The different flow regimes occurring in a wide range of Reynolds numbers are well described by Carmichael [1].

The regime at Reynolds number lower than 10^2 is of interest for devices used to reduce the turbulence level of wind tunnels, but not for airfoil-like machines. The regime of Reynolds number up to 10^4 regards insects and small model airplanes. The flow is strongly laminar and not able to sustain adverse pressure gradients. Some interesting solutions are adopted in nature in order to prevent the separation. The dragonfly has a saw tooth single surface airfoil. It is thought that eddies are formed in the troughs and keep the flow attached. The fly has a large number of fine hair-like elements that promote an eddy-induced energy transfer and prevent separation.

The range of Reynolds number between 10^4-10^5 is typical of flying animals and large model airplanes. At the lower end of this regime, natural laminar regime is possible provided that the lift coefficient of the flying machine remains quite low (≈ 0.5). Higher lift coefficients would produce a flow separation without re-attachment with a drop in lift and a rise of the drag coefficient. Carmichael [1] has pointed out that, under natural laminar flow separation, the distance between the separation and the re-attachment point expressed in terms of Reynolds number is about 50000. Thus, if a separation occurs at Reynolds number lower than 50000, the distance to the trailing edge is insufficient for the re-attachment of the flow. At higher Reynolds number, re-attachment is possible, but the bubble is of significant length with an important impact on the performance.

The next Reynolds number regime, up to 10^6, is of interest of large soaring birds but also of large radio controlled model aircraft, ultra-light gliders, and human powered aircraft. Airfoils for wind turbines also operate in this regime. Laminar flow is possible and the performances of the airfoils are improved with respect to lower Reynolds numbers.

Large aircraft fly at Reynolds numbers of order of magnitude 10^7-10^8. It is still possible to obtain large regions of laminar flows. The flight altitude has to be high in order to keep the Reynolds number per unit length reasonably low. Favorable pressure gradients are necessary and are obtained through a careful design of the wing sections. Devices to stabilize the boundary layer are also used. Reynolds numbers still higher are typically for large water-immersed vehicles such as tankers and nuclear submarines.

1.1 Laminar Separation Bubbles

A laminar separation bubble (LSB) occurs when the flow separates in the laminar regime. The turbulence developing inside the re-circulation region enhances the momentum transport and the flow re-attaches. The laminar separation bubble is one of the main critical aspects of flows at low Reynolds number, of order of magnitude 10^4-10^5, but results to be crucial also for flows at high Reynolds numbers. In fact, very tiny laminar separation bubbles are present in airfoil used for turbine applications operating at Reynolds number of the order of magnitude of 10^6.

Laminar separation bubbles in a wide range of Reynolds numbers have been analysed in the project. Incompressible, but also compressible and transonic flows at low-Reynolds number have been taken into consideration. The interest for the compressible aerodynamics of low-Reynolds number flow has recently grown for the possible use of flying machines for exploring the Martian surface. The challenge of this technological solution lies entirely in the specific environmental conditions these aircraft will be required to operate in. Mars atmosphere is 95% constituted by CO_2 and the force of gravity is about 1/3 than the Earth's. The reduced atmospheric pressure and density, together with the low temperatures, produce flight conditions characterised by very low Reynolds numbers, about 2% of those on the Earth, in combination with high Mach numbers, 1.5 times higher than the terrestrial ones. Mars airplane is expected to perform a flight at low Reynolds number in the range of $10^4 - 10^5$ at relatively high speed to produce enough lift to sustain its weight as well as to ensure a stable flight in gusty atmosphere.

Laminar instability analysis methods have been also investigated in the project. The focus has been placed on their capability in modelling flow instabilities as they convect through a LSB. Laminar separation bubbles involve low velocity reversed flow and instabilities methods based on the parabolised stability equations (PSE) may not be appropriate because assume that disturbance flow information only propagates in the main stream direction. However, recent works have indicated that PSE methods are generally quite robust even in the presence of laminar separation bubbles. An assessment of the results by the PSE theory with local parallel linear stability theory (LST), as well as with more advanced results gained from the full unsteady DNS and linear Navier Stokes (LNS) model is between the goals of the project.

2 Objectives

The main goal of the action group has been to improve the modelling of the numerical methods used in the reproduction of the laminar separation bubbles. Incompressible flows in a wide range of Reynolds numbers have been analysed. An investigation of the main issues that flows at low Reynolds numbers could present in transonic conditions has also been performed.

The focus is placed on the methods based on the Reynolds Averaged Navier Stokes (RANS) equations. A crucial point in applying the RANS approach is the turbulence modelling. The most critical issues to be addressed are the determination of the transition location and the production of the turbulent kinetic energy. In fact, the presence of separation bubbles means that the separation is laminar and the transition points are very difficult to be set. The turbulence models are instead calibrated for separation in the turbulent flow regime, and need the transition points to be known ”a priori”. The other critical point is represented by the levels of turbulence inside the recirculation region of the bubble. A proper modelling of the production of the turbulent kinetic energy inside the recirculation region of the bubble should ensure a better reproduction of the pressure recovery and of the bubble length.

Common test cases have been performed by AG 59 participants and the comparison of the different methods and models has allowed to individuate the advices for the numerical simulation of the laminar separation bubbles. The quantities of interest are:

- The determination of the transition location;
- The enhancement of the production of the turbulent kinetic energy in the separated flow inside the recirculation region;
- Evolution of the bubble with the incidence and with turbulence level;
- Possible burst of the bubble at high incidence and consequences on the stall characteristics;
- Critical evaluation of the laminar boundary-layer instability analysis methods for the treatment of laminar separation bubbles.

The attention of the AG has been also devoted to low-Reynolds number flows in transonic regime. These flows have an unusual specification that could occur in non-Earth (i.e. Martian) atmosphere. The execution of a common test-case with available models has allowed for the assessment of the current methods and for the individuation of the main issues to be addressed for this kind of flows.

Boundary layer instability analysis tools have also been compared with the RANS results to ascertain deficiencies of the turbulent onset point; moreover, the RANS embedded turbulence/transition models have also provided significant insight into the efficacy of the boundary-layer instability and hence transition criteria.

3 Methods and Models

3.1 CIRA and University of Napoli "Federico II"

The interest of CIRA in the project has been the development and assessment of a methodology for low-Reynolds number flows.

A low-Reynolds variation of the well-known κ-ω SST turbulence model has been proposed by introducing in the blending functions a dependence on the Reynolds numbers [2]. An empirical criterion for imposing the transition was also proposed [3]. The formation, the evolution with the incidence, and even the burst of a laminar separation bubble has been reproduced by the RANS equations with a satisfactory agreement with the LES results [4]. The method proposed for detecting laminar separation bubbles was applied not only to airfoils at low Reynolds numbers but to flows at high Reynolds number, The NREL airfoils S809 and S827 were considered [5]. The tiny bubbles shown by these airfoils were not reproduced unless a transition location inside the bubble is provided "a priori".The choice of a proper location, where the production of the turbulent kinetic energy is switched on, has resulted to be crucial. The production of the turbulent kinetic energy inside the separated flow region should be properly modelled in order to enhance the levels of turbulence and the pressure recovery inside the bubble.

A transition model based on the intermittency function γ [6] has been recently implemented in the in-house developed code UZEN [7, 8]. This model can be particularly suited for the simulation of the laminar separation bubbles since it allows for simulations without an "a-priori" knowledge of the transition location.

3.1.1 γ Transition Model

The transition model proposed by [6] is composed of the intermittency transport equation which is defined as follows:

$$\frac{\partial \rho\gamma}{\partial t} + \frac{\partial \rho U_j \gamma}{\partial x_j} = P_\gamma - D_\gamma + \frac{\partial}{\partial x_j}\left[\left(\mu + \frac{\mu_t}{\sigma_\gamma}\right)\frac{\partial \gamma}{\partial x_j}\right] \tag{1}$$

The transition source term P_γ and the destruction/relaminarization term D_γ are defined as:

$$P_\gamma = F_{length}\rho S \gamma (1-\gamma) F_{onset} \tag{2}$$

$$D_\gamma = c_{a2}\rho\Omega\gamma F_{turb}(c_{e2}\gamma - 1) \tag{3}$$

where S is the strain rate magnitude and Ω is the magnitude of the absolute vorticity rate.

Transition onset is controlled by the triggering functions F_{onset} and F_{turb} that act in the production and destruction terms of γ equation, respectively.

$$F_{onset1} = \frac{Re_V}{C_{onset1} Re_{\theta_c}}; \quad F_{onset2} = min(F_{onset1}, 2.0) \tag{4}$$

$$F_{onset3} = max\left(1 - \left(\frac{R_T}{3.5}\right)^3, 0\right); \quad F_{onset} = max(F_{onset2} - F_{onset3}, 0) \tag{5}$$

$$F_{turb} = e^{-\left(\frac{R_T}{2}\right)^4}; \quad R_T = \frac{\rho k}{\mu\omega}; \quad Re_V = \frac{\rho d_w^2 S}{\mu}; \quad Re_{\theta_c} = f(Tu_L, \lambda_{\theta L}) \tag{6}$$

Critical Reynolds number Re_{θ_c} In the current model, there is no transport equation for the transitional Reynolds number Re_{θ_t}, used to compute the critical Reynolds number Re_{θ_c} as in [9, 10] but an algebraic formula was developed:

$$Re_{\theta_c}(Tu_L, \lambda_{\theta L}) = C_{TU1} + C_{TU2}\exp\left[-C_{TU3}Tu_L F_{PG}(\lambda_{\theta L})\right] \tag{7}$$

The C_{TU1} constant defines the minimal value of the critical Re_{θ_c} number. The sum of $C_{TU1} + C_{TU2}$ defines its maximal value, while C_{TU3} controls how fast Re_{θ_c} decreases as the turbulence intensity Tu increases. The original set of constants reported in table 1 was implemented. [11, 12] proposed a new set of values for C_{Tu1}, C_{Tu2} and C_{onset1} variables. Their work was based on an experimental/numerical rebuilding for wind turbine applications, leading to the rescaling reported in table 1 and valid for a free-stream Reynolds number in the range $3 \times 10^6 \leq Re_\infty \leq 15 \times 10^6$. This set was additionally implemented in the solver.

Table 1: Re_{θ_c} constants

	C_{TU1}	C_{TU2}	C_{onset1}
Original values	100.00	1000.00	2.2
Modified values	163.00	1002.25	$\min\{4.84, \max[2.2, 1.388\ln(Re_\infty \times 10^{-6}) + 0.705]\}$

Turbulence Model Coupling Transition model was coupled with the "Standard" $\kappa - \omega$ SST turbulence model [13]. The transport equation for turbulent dissipation ω is kept as in the original formulation, while the transport equation for turbulent kinetic energy κ is modified as follows:

$$\frac{\partial}{\partial t}(\rho k) + \frac{\partial}{\partial x_j}(\rho u_j k) = \tilde{P}_k + P_k^{lim} - \tilde{D}_k + \frac{\partial}{\partial x_j}\left((\mu + \sigma_k \mu_t)\frac{\partial k}{\partial x_j}\right) \tag{8}$$

$$\tilde{P}_k = \gamma P_k \tag{9}$$

$$\tilde{D}_k = max(\gamma, 0.1)D_k \tag{10}$$

$$\mu_t = \rho\frac{a_1 k}{max(a_1\omega, F_2 S)} \tag{11}$$

where P_k and D_k are the production and destruction terms from the turbulent kinetic energy equation in the original SST turbulence model and P_k^{lim} is an additional production term:

$$P_k^{lim} = 5C_k max(\gamma - 0.2, 0)(1-\gamma)F_{on}^{lim} max(3C_{SEP}\mu - \mu_t, 0)S\Omega \tag{12}$$

$$F_{on}^{lim} = min(max(\frac{Re_V}{2.2Re_{\theta_c}^{lim}} - 1, 0), 3) \tag{13}$$

$$Re_{\theta_c}^{lim} = 1100 \quad C_k = 1.0 \quad C_{SEP} = 1.0 \tag{14}$$

3.1.2 Proposed Model

Catalano and de Rosa applied the γ model to laminar separation bubbles [14]. The bubble is found with a good estimation of the length, but the minimum of the C_f and the pressure recovery in the reattachment region are underestimated. Bernardos has proposed the LSST $\kappa - \omega$ model based on a function f_{tr} able to boost the production of the turbulence kinetic energy κ in the bubble [15]. Excellent results have been achieved. However, the model is coupled to the the AHD–Gleyzes transition prediction criterion because the function f_{tr} requires the knowledge of the separation, and transition points.

Actually, the Menter's intermittency function at the wall γ_w and the Bernardos' transition function f_{tr} exhibit a similar qualitative behaviour, as shown in figure 1. The physical phenomena simulated by the two functions must be correlated, with the difference that γ_w is an order of magnitude smaller than f_{tr}, thus leading to an insufficient production of turbulence. The basic idea of the developed model has been to amplify Menter's intermittency function in order to fit the values of f_{tr} at the wall. The purpose is twofold. Taking advantage of the γ function for information on the transition, and of the capability of the Bernardos' transition function f_{tr} in boosting the production of turbulence in the rear part of the bubble.

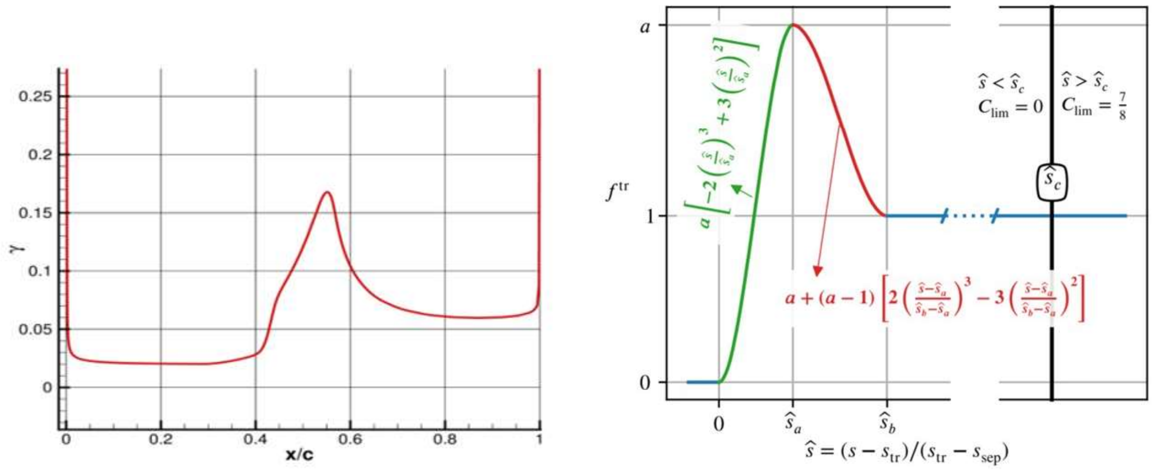

(a) Intermittency function γ at the wall (SD 7003 airfoil $Re = 6.0 \times 10^4$, $\alpha = 4°$)

(b) Function f_{tr} [15]

Figure 1: Intermittency function $\gamma_{\mathbf{w}}$ and $\mathbf{f_{tr}}$ function [15]

Preliminary simulations have been performed for the flow around the SD7003 airfoil at Reynolds number 6.0×10^4, the Eppler 387 airfoil at Reynolds number 3.0×10^5, and the NACA 0015 airfoil at Reynolds number 1.8×10^5. A C topology grids with 1328×192 cells for the EPPLER 387 and NACA 0015 and 1512×192 cells for the SD 7003 airfoil have been employed. It has been verified that the values of y^+ are under one for all the three airfoils.

The intermittency function at the wall γ_w has been computed for each bubble, as well as the separation, transition and reattachment locations. An interesting correlation has been found between transition and reattachment locations and the γ_w function. The transition occurs when the first derivative of the intermittency function $\gamma_w^{'}$, reaches a local maximum value. The reattachment occurs near the location where $\gamma_w^{'}$ has his absolute minimum value. No correlation has been found for the separation location. The intermittency function has a constant behaviour where the flow separation occurs. This correlation has been verified for all the simulations performed.

Determination of a fitting function A fitting function F_{fit}, that permits to recover f_{tr} from γ_w, has been determined in a four-step approach :

1. the results of the simulations with Menter's $\kappa - \omega - \gamma$ model were used to estimate the separation, and transition needed as an input to compute Bernardos' transition function f_{tr};
2. a fitting of the intermittency function at the wall γ_w with Bernardos' transition function was performed for each LSB computed;
3. a mean fitting function was determined for each airfoil and interpolated with a parabola;
4. the final $F_{fitting}$ was determined as the mean parabola between the three parabolas obtained for the three airfoil (figure 2). The $F_{fitting}$ is described by the following equation: $z = a\,\bar{x}^2 + b\,\bar{x} + c$, where a translation is performed through $\bar{x} = x - x_0$, to make the first zero of the parabola coincident with the transition point x_{tr}. The coefficients of the parabola are reported in table 2.

a	b	c
-140.8227	251.6973	-96.7556

Table 2: Coefficients for the fitting function.

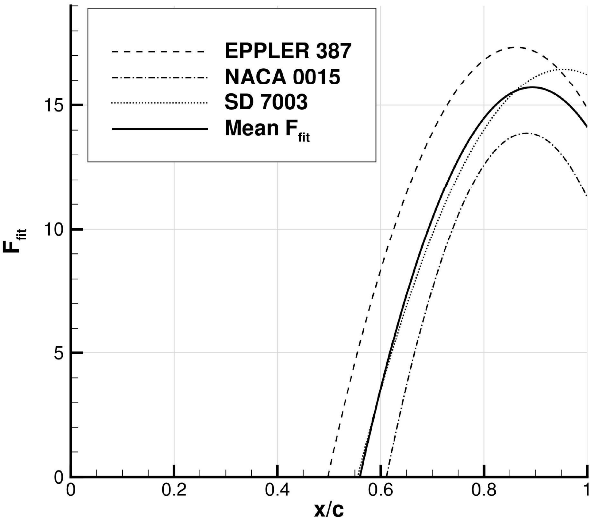

Figure 2: Mean interpolating parabola of the fitting functions.

The proposed model [16] is a merging of the two models. The basis is the Menter $\kappa - \omega$ SST turbulence model coupled with γ transition model, with the modification of the production terms for κ and ω, that are now multiplied by the fitting function $F_{fitting}(x, x_{tr})$.

$$\begin{aligned}\frac{\partial(\rho\kappa)}{\partial t}+\frac{\partial(\rho\kappa u_j)}{\partial x_j} &= \gamma\, F_{fitting}\, P_k - P_k^{lim} - max(\gamma, 0.1)\cdot D_k \\ &+ \frac{\partial}{\partial x_j}\left[(\mu+\sigma_k\mu_t)\frac{\partial\kappa}{\partial x_j}\right] \qquad (15)\end{aligned}$$

$$\frac{\partial(\rho\omega)}{\partial t}+\frac{\partial(\rho\omega u_j)}{\partial x_j} = \gamma\, F_{fitting}\,\frac{\omega}{\kappa}\tau_{ij}\frac{\partial u_i}{\partial x_j} - \beta\rho\omega^2 + \frac{\partial}{\partial x_j}\left[(\mu+\sigma_\omega\mu_t)\frac{\partial\omega}{\partial x_j}\right] + 2(1-F_1)\rho\sigma_{\omega_2}\frac{1}{\omega}\frac{\partial\kappa}{\partial x_j}\frac{\partial\omega}{\partial x_j} \qquad (16)$$

$$\frac{\partial(\rho\gamma)}{\partial t}+\frac{\partial(\rho\gamma u_j)}{\partial x_j} = P_\gamma - E_\gamma + \frac{\partial}{\partial x_j}\left[(\mu+\frac{\mu_t}{\sigma_\gamma})\frac{\partial\omega}{\partial x_j}\right] \qquad (17)$$

The fitting function has the role of enhancing the turbulence production in the bubble zone, just as Bernardos' transition function. The $F_{fitting}(x, x_{tr})$ is dependent on the transition location with x_{tr} retrieved by the intermittency function γ_w.

3.2 CNR-INM

The Institute of Marine Engineering of National Research Council of Italy (CNR-INM) has made available to AG59 members experimental data for the NACA 0015 airfoil at Reynolds number 1.8×10^5. The data include quantitative maps of the friction coefficient at three angles of attack: 3°, 5°, and 10°.

3.2.1 Theoretical background

When a fluid flows around an immersed body with slightly different temperature, it modifies the body's surface temperature distribution. This modification is quantified by the efficiency in heat exchange of the local flow structures that develop within the (laminar or turbulent) boundary layer. There are at least two approaches to understand the connection between skin friction and temperature distribution on the body's surface. One approach relates the evolution of the temperature distribution to the action of the skin-friction field through the energy equation in its asymptotic form at the wall. The other approach considers the transport of temperature disturbances at the wall as a passive scalar, which unveils the relationship chain connecting the celerity of propagation of thermal blobs with the celerity of propagation of velocity disturbances and eventually with the friction velocity.

The energy equation approach leads to a single-snapshot optical flow-like methodology, called the OF algorithm, which can provide time-resolved, relative skin friction fields. This algorithm requires a temperature field that only originates from the interaction between the colder or warmer fluid and the warmer or colder wall, respectively. Thus, temperature gradients that are not induced by the boundary layer may introduce bias in the skin friction estimation. In contrast, the approach adopted in this analysis considers the transport of the fluctuating component of the temperature field as a passive scalar. Following [17] , Miozzi et al. [18] proposed a physically motivated convection velocity of a passive scalar, which depends on the spectral information in only one direction, either space or time, and on a local derivative in the remaining direction. In practice, the method consists on minimizing the dissimilarity between the observed behavior and the ideal wave one, conforming to the Taylor hypothesis. In other words, it means finding the characteristic velocity of the reference frame where waves experience the least change if compared to the Taylor hypothesis. This quantity represents the absolute value of the celerity of propagation of the velocity fluctuations. Following the seminal findings of [19], enforced by [20, 17], it is in a linear relationship with the friction velocity u_τ. The proposed method estimates the propagation celerity of temperature fluctuations U_T, and because of its relationship with the friction velocity $\mathbf{u}_\tau$ [21], it estimates the friction coefficient C_f. DLR and CNR-INM cooperated to develop and apply different methodologies to extract skin-friction fields from temperature maps using Temperature Sensitive Paint (TSP) [22]. Sensors relying on this technology yield global temperature data from the whole coated surface, with elevate resolution in space and time [23, 24].

3.2.2 Experimental Setup

The experiments were conducted in the CEIMM cavitation tunnel (CNR-INM, Rome, IT), which is a closed-loop water facility with a square test section that has side $B = 600\,\text{mm}$, length $L_S = 2.6\,\text{m}$, and optical access. The nozzle contraction ratio is $5.96 : 1$.

The aluminum-made hydrofoil has a symmetric NACA 0015 profile, with a chord length of $C = 120\,\text{mm}$ and a span width equal to the test-section side ($L = B = 600\,\text{mm}$). This corresponds to an aspect ratio and blockage factor of $B/C = 5$ and $C/B = 0.2$, respectively. The model is mounted in the middle of the tunnel transverse side and rotated around its geometric center to set the profile at the investigated angles of attack [25].

The hydrofoil is coated with a TSP functional set of layers. When excited at a wavelength of 405 nm, the TSP emits light at 610 nm with an intensity inversely proportional to the local temperature, undergoing the thermal quenching [23]. The emission is captured by a Photron SA-X fast camera, equipped with Nikkor 50 mm $f/1.4$ optics, holding a long-wave pass filter with a cut-point at 600 nm. The camera captures the emission at a frequency $f_r = 1000\,\text{Hz}$, providing time- and spatially-resolved information about the efficiency of the boundary layer in modifying the temperature statistics distribution. To enhance the signal-to-noise ratio of the thermal fingerprints of the flow structures on the model surface, the body of the hydrofoil is pierced spanwise by three ducts where externally heated water (warmer than the tunnel water) is forced to flow.

The tests reported here investigate the temperature of the hydrofoil's surface at a chord-based Reynolds number $Re = 1.8 \times 10^5$ and Angles of Attack $AoA = [5°,\ 10°]$. At these experimental conditions, the flow uniformity is less than 3% for the vertical component and 1% for the axial one. The components of the freestream turbulence level within the TSP test section, $U' = U_{\text{rms}}/U_\infty$ and $V' = V_{\text{rms}}/U_\infty$, are less than 2% in the central region of the test section, and lower of 1% in the investigated region for the streamwise one.

3.3 DLR

3.3.1 Numerical methods

The instability of steady flows to small amplitude perturbations can be analysed using the modal approach. Given an operator that describes the evolution of small perturbations, this approach considers the temporal or spatial development of individual eigenmodes of that operator. The resulting linear stability theory relies on the decomposition of all flow quantities $\boldsymbol{q}$ into a steady basic flow $\overline{\boldsymbol{q}}$ plus an unsteady disturbance flow component $\tilde{\boldsymbol{q}}$ according to:

$$\boldsymbol{q}(\boldsymbol{x}, t) = \overline{\boldsymbol{q}}(\boldsymbol{x}) + \epsilon \tilde{\boldsymbol{q}}(\boldsymbol{x}, t), \qquad \epsilon \ll 1, \tag{18}$$

where $\boldsymbol{x}$ is the space coordinate vector and t is time. Substituting (18) into the Navier-Stokes (NS) equations, subtracting the equations satisfied by the steady flow, and dropping the terms of order higher than ϵ yields the Linearized Navier-Stokes (LNS) equations. Different assumptions can be made for the form of the basic flow and the disturbances in (18), which then result in the governing equations associated with LST, PSE and AHLNS.

Local stability theory In LST the flow is assumed to be parallel thus not accounting for the growth of the boundary layer. In the classical LST, the basic flow is considered homogeneous along two out of the three spatial directions, here streamwise x and spanwise z direction. Therefore, the flow is only dependent on the wall-normal coordinate, and the perturbation has the following form:

$$\begin{aligned}\tilde{\boldsymbol{q}}(x,y,z,t) &= \hat{\boldsymbol{q}}(y)e^{i\Theta(x,z,t)} + c.c.\\ \Theta(x,z,t) &= \alpha x + \beta z - \omega t,\end{aligned} \tag{19}$$

where ω is the angular frequency, c.c. denotes the complex conjugate, and α, β are the wavenumbers in streamwise and spanwise direction, respectively.

Parabolized stability equations A more general representation of the disturbances is given by:

$$\begin{aligned}\tilde{\boldsymbol{q}}(x,y,z,t) &= \hat{\boldsymbol{q}}(x,y)e^{i\Theta(x,z,t)} + c.c.\\ \Theta(x,z,t) &= \int_{x_0}^{x} \alpha(x')dx' + \beta z - \omega t.\end{aligned} \tag{20}$$

If a flow varies slowly in one spatial direction, say x, then a scale separation $1/Re$ is introduced between the weak variation in the x direction and the strong variation in the y direction. The normal basic flow velocity component and the streamwise dependence of the basic and disturbance flow scale with $1/Re$, where Re is based on a length scale l^* proportional to the boundary-layer thickness, $l^* = \sqrt{x^*\nu^*/U^*}$ ($*$ denotes dimensional quantities). With the above scaling and ansatz (20) introduced into the LNS equations, considering only terms that scale with powers of Reynolds number up to $1/Re$, we obtain the stability analysis approach based on PSE. The effects of small flow non-parallelism are consistently taken into account and due to the fact that the disturbance characteristics predicted by such a method are influenced by local and upstream flow conditions, this theory is called nonlocal. For a complete explanation about the PSE methodology, the readers are referred to [26]. Stability calculations were performed with the spatial nonlocal linear stability code NOLOT, which was developed in cooperation between DLR and the Swedish defence research agency FOI and has been extensively validated [27].

Adaptive harmonic linearized Navier-Stokes methodology The AHLNS equations are obtained in a similar way to the PSE formulation as regards the wave-like character of the disturbances which are divided into an amplitude function and wave function as Eq. (20). However, differently from the PSE approach, the streamwise wavenumber α and the amplitude function $\hat{\boldsymbol{q}}$ are allowed to vary rapidly in streamwise direction. The assumption of slowly varying flow in streamwise direction is removed also for the basic flow, so that all the terms of the LNS equations are kept. A multi-zonal approach is then applied, which exploits AHLNS where the streamwise variations of the basic flow and amplitude function are not small and PSE elsewhere. In the following, results obtained using this multi-zonal approach will be labeled as AHLNS results. For a detailed description of this methodology the readers are referred to Franco et al. [28].

Direct numerical simulation Direct Numerical Simulations (DNS) were performed using the Nek5000 code [29] which is based on the Spectral Element Method (SEM). The SEM decomposes the physical domain into (spectral) elements where the flow field solution is given by a sum of Lagrange interpolants defined by an orthogonal basis of Legendre polynomials up to degree P within each element. The results presented here were obtained with a polynomial order $P = 9$ within the spectral elements.

3.3.2 Geometry-induced separation bubble

In two-dimensional (2-D) flows the boundary-layer transition scenario is dominated by Tollmien-Schlichting (TS) instabilities. Common wing-surface irregularities, such as two-dimensional steps, gaps or waviness can cause separation, denoted geometry-induced separation, and alter the growth characteristics of TS waves [30]. In the past, LST and PSE, together with the e^N method, have been successfully applied for transition prediction in cases without surface irregularities where the local streamwise flow gradients were small. However, the validity of the assumptions of such methods becomes questionable with the increased gradients locally induced by the surface irregularities. AHLNS removes some of the inherent limitations present in LST and PSE, and it has been already applied successfully in the presence of surface irregularities by Franco et al. [31, 32]. In the following the spatial linear instability analysis of TS waves is presented briefly through the results provided by LST, PSE, AHLNS and DNS in the presence of different 2-D irregularities on a flat plate in an incompressible flow [33]. Even if limited to a single frequency ($\mathrm{F} = 2\pi f^* \nu^* / {U^*_\infty}^2 = 49.34 \times 10^{-6}$), comparison with DNS allows to evaluate the accuracy and applicability of the different approaches.

Laminar basic flows The surface irregularities are located on a flat plate without pressure gradient at Reynolds number based on the centre position of the irregularity $Re_{x_c} = 4 \cdot 10^5$. The Blasius length scale $l^*_c = x^*_c / \sqrt{Re_{x_c}}$ at this location is chosen for non-dimensionalization. With this scaling, the center of the irregularities is located at $x_c = 632.46$. The non-dimensional height or depth of the geometric features is $h = 0.808$ ($Re_h = 511$) and the non-dimensional width of the humps and gap is $b = 31.62$ ($Re_b = 2 \cdot 10^4$). We refer the reader to [34] for further details on the basic flow characteristics. Fig. 3 shows the steady laminar basic flow for three of the surface imperfections studied: a smooth hump, a rectangular hump and a smooth gap. For LST, the basic state is approximated as locally parallel, an assumption that does not hold, in particular in the vicinity of the irregularity where the flow is deflected reaching higher value of the wall-normal velocity (Fig. 3). Besides violating the nonparallel assumption, the local distortion of the boundary layer induced by the irregularities might conflict with the PSE requirement of a slowly changing basic flow in the streamwise direction. As expected, the rectangular hump introduces stronger localized streamwise gradients compared to the smooth hump and smooth gap as shown in Fig. 4 where the derivative $\partial \overline{u} / \partial x$ is plotted.

Instability analysis The amplification curves of the DNS results presented in [34] allow a quantitative comparison with LST, PSE, and AHLNS through the relation:

$$\ln \left(A_u / A_{ref}\right)_{DNS} = \int_{x_{ref}}^{x} \sigma(x') dx', \tag{21}$$

where A_u is the maximum amplitude along the wall-normal coordinate ($A_u(x) = \max_y |\hat{u}(x, y)|$) and σ is the spatial disturbance growth rate. In LST, the spatial growth rate is computed from the imaginary part of the complex streamwise wavenumber, $\sigma = -\alpha_i$. In PSE and AHLNS, it is given by $\sigma = -\alpha_i + \Re(\frac{1}{\xi}\frac{\partial \xi}{\partial x})$, where $\hat{u}$ at the wall-normal location where it reaches its maximum value, has been chosen among the possible choices for ξ. The comparison between LST, PSE, AHLNS,

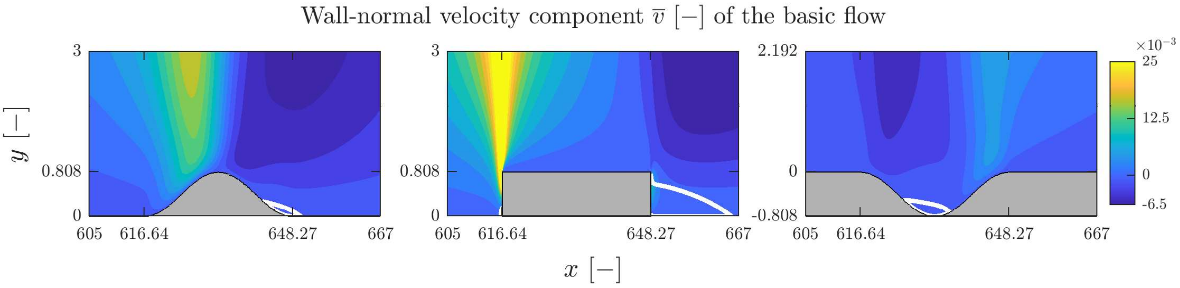

Figure 3: Coloured contours of the non-dimensional wall-normal velocity component $\overline{v}$ and iso-line (white) of the non-dimensional streamwise velocity component $\overline{u} = 0$ for the basic flows (the axes are not to scale). From left to right: smooth hump, rectangular hump and smooth gap.

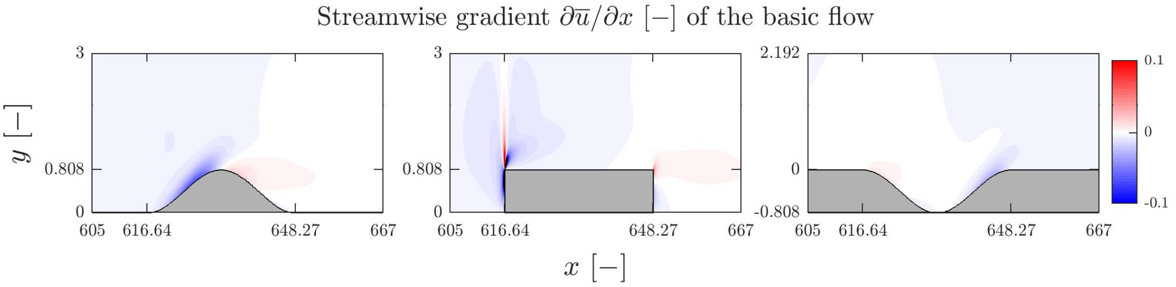

Figure 4: Coloured contours of the non-dimensional streamwise derivative of the streamwise velocity component $\overline{u}$ for the basic flow (the axes are not to scale). From left to right: smooth hump, rectangular hump and smooth gap.

and DNS is shown in Fig. 5 for a smooth hump, rectangular hump and smooth gap. The AHLNS amplification curves are in excellent agreement with those obtained by DNS for all the surface irregularities considered here, demonstrating the validity of this methodology to study the effect of surface irregularities on the spatial development of convective boundary-layer instabilities. PSE is able to predict the development of TS waves over the smooth hump and gap with some deviations in the region of the irregularities which, anyway, do not cause large differences far downstream where the same growth rate of the flat plate is recovered. The grid convergence of the PSE results could be obtained only for the smooth irregularities and, therefore, the PSE curve is not plotted for the rectangular hump. For the latter, it is worth mentioning that the PSE results were considerably affected not only by the step-size restriction, i.e. the number of points, but also by the distribution of the points where the PSE computation is done, especially in the vicinity of the irregularity [33]. For all investigated cases, LST is over-predicting the growth in the area of the separation bubble induced by the irregularities. As a result, the amplification level far downstream is higher compared to DNS and AHLNS.

The LST and PSE computations required several seconds, respectively. The AHLNS computations took around minutes and come at a fraction of the cost of DNS which are orders of magnitude more expensive. The AHLNS approach, given the excellent agreement with DNS for all the cases,

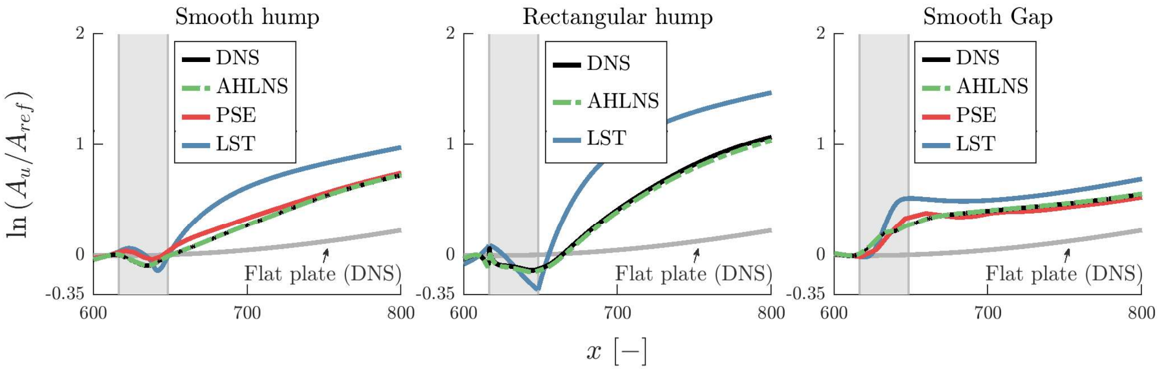

Figure 5: Natural logarithm of the normalized disturbance amplitude for TS waves at $F = 49.34 \times 10^{-6}$. The grey area indicates the location of the humps and gap. A_{ref} represents the maximum amplitude of $\hat{u}$ along y at $x_{ref} = 610$.

proves to be a perfectly suited tool for the boundary-layer instability analysis in the presence of large streamwise gradients. Moreover, with a moderate computational effort compared to DNS, it is well suited for parametric studies. The use of PSE should be avoided in the presence of sharp corners, where the assumption of slowly varying basic flow with respect to x is violated but it could still be valid for smooth irregularities such as the ones studied here. However, we remind the reader that PSE could also provide wrong spatial amplification in the presence of smooth irregularities if they introduce stronger streamwise gradients. Moreover, PSE requires some attention due to its step-size restriction with respect to the resolution required in the vicinity of the irregularities [33]. Besides these mere numerical considerations, one should always keep in mind that, when the characteristic length scale of the perturbation in the streamwise direction, i.e. the TS wavelength, is of the same order or larger as the corresponding characteristic length scale of the streamwise flow variation induced by the surface irregularity, the applicability of PSE is dubious. LST shows large differences from the DNS results in all the cases studied. This disagreement is due to the inherent weaknesses of the LST modelling assumptions in the presence of surface irregularities which induce strong local distortions of the boundary layer.

3.4 ONERA

The interest of ONERA in this project was to evaluate recently proposed numerical approaches for modeling the laminar-to-turbulent transition of laminar separation bubbles. Full details on numerical and physical models can be found on published literature [35, 15].

In this work, the Reynolds-averaged Navier Stokes (RANS) equations were resolved using the elsA code [36] developed at ONERA. elsA is a hybrid structured/unstructured finite-volume solver for compressible flows. However, structured meshes were exclusively employed in this work since the chosen transition models are not implemented in unstructured meshes yet.

Turbulent regions were modelled using the $k-\omega$ turbulence model. Specifically, Wilcox2006-klim [37] model was used, unless otherwise stated.

The transitional flow was modeled using the laminar separation transition triggering (LSTT) technique proposed by Bernardos et al. [35]. This technique consists in progressively activating the turbulence model in the streamwise direction of the separated flow by enhancing the production of turbulence. This enhancement of production of turbulence is accomplished by locally boosting the production term of kinetic energy of turbulence, k, using a positive weighting factor, f^{tr}, that can be greater than one, and locally disabling the shear-stress limiter and the production of specific dissipation of turbulence, ω. This is summarized by the modeling equations (22).

$$\frac{\partial \rho k}{\partial t} + \frac{\partial \rho k \overline{u}_j}{\partial x_j} = f^{\mathrm{tr}}(-\overline{\rho u_i' u_j'})\frac{\partial \overline{u}_i}{\partial x_j} - \beta_k \rho \omega k + \frac{\partial}{\partial x_j}\left[(\mu + \sigma_k \mu_t)\frac{\partial k}{\partial x_j}\right] \tag{22a}$$

$$\begin{aligned}\frac{\partial \rho \omega}{\partial t} + \frac{\partial \rho \omega \overline{u}_j}{\partial x_j} =& \min(f^{\mathrm{tr}},\, 1)\alpha_\omega \frac{\omega}{k}(-\overline{\rho u_i' u_j'})\frac{\partial \overline{u}_i}{\partial x_j} - \beta_\omega \rho \omega^2 + \frac{\partial}{\partial x_j}\left[(\mu + \sigma_\omega \mu_t)\frac{\partial \omega}{\partial x_j}\right] \\ &+ \sigma_d \frac{\rho}{\omega}\max\left(\frac{\partial k}{\partial x_j}\frac{\partial \omega}{\partial x_j}, 0\right)\end{aligned} \tag{22b}$$

$$(-\overline{\rho u_i' u_j'}) \approx 2\mu_t \overline{S}_{ij}^d - \frac{2}{3}\rho k \delta_{ij} \tag{22c}$$

$$\mu_t = \frac{\rho k}{\max\left\{\omega; C_{\mathrm{lim}}\sqrt{\frac{2\lambda_1 \overline{S_{ij}}\,\overline{S_{ij}} + 2\lambda_2 F_2^2 \overline{\Omega_{ij}}\,\overline{\Omega_{ij}}}{(\lambda_1 + \lambda_2)\beta_k}}\right\}} \tag{22d}$$

The non-local law of the progressive activation of the turbulence model, f^{tr}, follows a simple polynomial form (cubic polynomial) in the main streamwise direction. The shear-stress limiter delay mechanism, C_{lim}, is the heaviside function. Both coefficients are shown in Fig. 6.

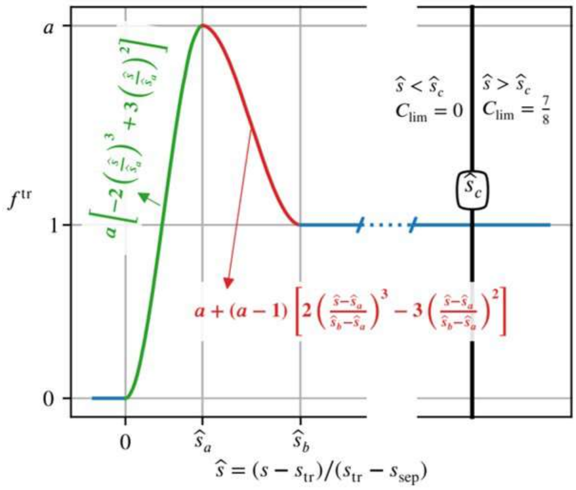

Figure 6: LSTT triggering functions.

The closure coefficients of the polynomial are calibrated using a reference flow computed using DNS technique [35] in order to accurately fit a skin-friction distribution of a laminar separation bubble. Results are summarized in 3.

The LSTT activation shown in Fig. 6 requires knowledge of both the transition point and the laminar separation point, respectively s_{tr} and s_{sep}. The former is obtained using transition criteria like AHD-Gleyzes as shown in [15]. The latter is obtained by direct evaluation of the skin friction vector with respect to the boundary layer velocity vector, such that $\vec{U}_e \cdot \vec{\tau}_w < 0$ determines the separated region.

	$\hat{s}_a$	$\hat{s}_b$	$\hat{s}_c$	a
Wilcox 2006	0.182	0.414	5.83	2.15
Kok	0.200	0.620	5.83	2.23
Menter SST	0.312	0.544	5.83	2.20
Wilcox 1988	0.086	0.487	3.78	1.85

Table 3: LSTT closure coefficients for several $k-\omega$ turbulence models proposed by Bernardos et al. [35].

We note that both f^{tr} and C_{lim} are curvilinear abscissa functions (dependent on s). In this formulation, curvilinear abscissa supported on wall surfaces are user-defined quantities. In practice, sutructured grid directions on wall surfaces are used as curvilinear abscissa. However, in order to apply these functions on system (22), a 3D extrusion of these quantities must be performed. This can be accomplished by using a minimum orthogonal interference algorithm. Propagation of these quantities can be done either across the entire computational domain, or it can be confined within a prescribed distance of the boundary-layer thickness, δ. In this work, negligible difference was found between infinite extrusion and confined extrusion.

3.5 Marche Polytechnic University

The interest of UNIVPM research team was to investigate the effectiveness of Spalart–Allmaras equation coupled with local correlation based (LCTM) transition models. Specifically, we consider two different approaches consisting in the adoption of one or two equations for transition modeling. The complete set of our flow governing equations can be written as

$$\begin{aligned}
&\frac{\partial u_j}{\partial x_j} = 0,\\
&\frac{\partial u_i}{\partial t} + \frac{\partial}{\partial x_j}\left(u_i u_j\right) + \frac{\partial p}{\partial x_i} - \frac{\partial}{\partial x_j}\left(\left(\nu+\nu_t\right) S_{ij}\right) = 0,\\
&\frac{\partial \tilde{\nu}}{\partial t} + \frac{\partial}{\partial u_j}\left(u_j\tilde{\nu}\right) - \mathrm{P}_{\tilde{\nu}} + \mathrm{D}_{\tilde{\nu}} - \frac{c_{b2}}{\sigma}\frac{\partial \tilde{\nu}}{\partial x_j}\frac{\partial \tilde{\nu}}{\partial x_j} - \frac{1}{\sigma}\frac{\partial}{\partial x_j}\left[\left(\nu+\tilde{\nu}\right)\frac{\partial \tilde{\nu}}{\partial x_j}\right] = 0,
\end{aligned} \tag{23}$$

where u_j are the velocity vector components, $p = P/\rho$ is the pressure divided by the density, d is the distance form the nearest wall and ν is the kinematic viscosity. The turbulent viscosity, ν_t, is computed according to the $\tilde{\nu}$ variable as

$$\nu_t = f_{v1}\tilde{\nu}, \tag{24}$$

the following closure functions are introduced to close $\tilde{\nu}$ equation (eq. 23):

$$\begin{aligned}
&f_{v1} = \frac{\chi^3}{\left(\chi^3 + c_{v1}^3\right)}, && f_{v2} = 1 - \frac{\chi}{\left(1+\chi f_{v1}\right)},\\
&g = r + c_{w2}\left(r^6 - r\right), && f_w = g\left[\frac{1+c_{w3}^6}{g^6 + c_{w3}^6}\right]^{\frac{1}{6}},\\
&\tilde{S} = \left[\Omega + \min\left(0, S-\Omega\right)\right] + \frac{\tilde{\nu}}{k^2 d^2} f_{v2}, && r = \begin{cases} r_{max} & \frac{\tilde{\nu}}{\tilde{S}k^2d^2} < 0 \\ \min\left(\frac{\tilde{\nu}}{\tilde{S}k^2d^2}, r_{max}\right) & \frac{\tilde{\nu}}{\tilde{S}k^2d^2} \geq 0 \end{cases},
\end{aligned} \tag{25}$$

where $\chi = \tilde{\nu}/\nu$ is the dimensionless turbulent variable, $\Omega_{ij} = \sqrt{2W_{ij}W_{ij}}$ is the vorticity tensor module, $S = \sqrt{2D_{i}jD_{i}j}$ is the strain rate tensor module, and $\tilde{S}$ is a function of both the vorticity magnitude Ω and $\tilde{\nu}$. Finally, to complete the SA model, the following (standard) closure constants are adopted:

$$c_{b1} = 0.1355, \quad c_{b2} = 0.622, \quad c_{v1} = 7.1, \tag{26}$$

$$\sigma = 2/3, \quad c_{w1} = \frac{c_{b1}}{k^2} + \frac{(1 + c_{b2})}{\sigma}, \tag{27}$$

$$c_{w2} = 0.3, \quad c_{w3} = 2, \quad k = 0.41. \tag{28}$$

3.5.1 γ–$\widetilde{\mathrm{Re}}_{\theta,t}$–SA transition model

In this approach, we use two transport equations to model the transition:

$$\begin{aligned} &\frac{\partial \gamma}{\partial t} + \frac{\partial}{\partial x_j}(u_j \gamma) = \mathrm{P}_\gamma - \mathrm{D}_\gamma + \frac{\partial}{\partial x_j}\left[\left(\nu + \frac{\nu_t}{\sigma_f}\right)\frac{\partial \gamma}{\partial x_j}\right], \\ &\frac{\partial \widetilde{\mathrm{Re}}_{\theta,t}}{\partial t} + \left(u_j \widetilde{\mathrm{Re}}_{\theta,t}\right) = \mathrm{P}_{\theta,t} + \frac{\partial}{\partial x_j}\left[\sigma_{\theta,t}(\nu + \nu_t)\frac{\partial \widetilde{\mathrm{Re}}_{\theta,t}}{\partial x_j}\right]. \end{aligned} \tag{29}$$

The source terms in the γ equation are defined as:

$$\begin{aligned} \mathrm{P}_\gamma &= c_{a1} S \left[\gamma \mathrm{F}_{\text{onset}}\right]^{0.5}(1 - c_{e1}\gamma)\,\mathrm{F}_{\text{length}}, \\ \mathrm{D}_\gamma &= c_{a2}\Omega\gamma \mathrm{F}_{\text{turb}}(c_{e2}\gamma - 1), \end{aligned} \tag{30}$$

in P_γ the term $\mathrm{F}_{\text{onset}}$ is computed as:

$$\mathrm{F}_{\text{onset}} = \max\left(\mathrm{F}_{\text{onset},2} - \mathrm{F}_{\text{onset},3}, 0\right) \tag{31}$$

with

$$\begin{aligned} \mathrm{F}_{\text{onset},2} &= \min\left(\max\left(\mathrm{F}_{\text{onset},1}, \mathrm{F}_{\text{onset},1}{}^4\right), 4\right), \\ \mathrm{F}_{\text{onset},3} &= \max\left(2 - \left(\frac{\mathrm{R_T}}{2.5}\right)^3, 0\right), \\ \mathrm{F}_{\text{onset},1} &= \frac{\mathrm{Re}_\nu}{2.193\mathrm{Re}_{\theta,c}}. \end{aligned} \tag{32}$$

In eq. 32 the terms Re_ν and $\mathrm{R_T}$ are obtained as follows:

$$\mathrm{Re}_\nu = \frac{Sd^2}{\nu}, \qquad \mathrm{R_T} = \frac{\nu_t}{\nu}. \tag{33}$$

The aspects concerning the terms $\mathrm{F}_{\text{length}}$ and $\mathrm{Re}_{\theta,c}$ are described in Sec. 3.5.1. As regards, D_γ the coefficient F_{turb} is defined as:

$$\mathrm{F}_{\text{turb}} = \exp\left(-\frac{\mathrm{R_T}}{4}\right)^4. \tag{34}$$

For the source terms in the transport equation for $\widetilde{\mathrm{Re}}_{\theta,t}$, $\mathrm{P}_{\theta,t}$, the following equation is adopted:

$$\mathrm{P}_{\theta,t} = \frac{c_{\theta,t}}{\mathrm{T}}\left(\mathrm{Re}_{\theta,t} - \widetilde{\mathrm{Re}}_{\theta,t}\right)(1 - \mathrm{F}_{\theta,t}). \tag{35}$$

In eq. 35 the last term $\mathrm{F}_{\theta,t}$ is defined as:

$$\mathrm{F}_{\theta,t} = \min\left(\max\left(\exp\left(-\frac{u_j u_j}{375\Omega\nu\widetilde{\mathrm{Re}_{\theta,t}}}\right)^4, 1-\left(\frac{\gamma-1/c_{e2}}{1-1/c_{e2}}\right)^2\right), 1.0\right). \tag{36}$$

The term T which appears in $\mathrm{P}_{\theta,t}$ is defined as follows: $500\nu/\left|\mathbf{u}\right|^2$. Finally, the $\mathrm{Re}_{\theta,t}$ handling in eq. 35 is further discussed, together with the $\mathrm{F}_{\mathrm{length}}$ coefficient, in the next subsection.
For the transition model, the following closure constants are adopted:

$$c_{a1} = 2.0, \quad c_{a2} = 0.06, \quad c_{e1} = 1.0, \tag{37}$$

$$c_{e2} = 50, \quad c_{\theta,t} = 0.03, \quad \sigma_f = 1.0, \tag{38}$$

$$\sigma_{\theta,t} = 2.0. \tag{39}$$

Empirical correlations in the model

Like other γ–$\widetilde{\mathrm{Re}_{\theta,t}}$ approaches available in the literature, the present model contains three empirical correlations needed to compute $\mathrm{Re}_{\theta,t}$, $\mathrm{Re}_{\theta,c}$ and $\mathrm{F}_{\mathrm{length}}$.
In our approach, the correlation developed by by Menter et al. [38] for $\mathrm{Re}_{\theta,t}$ is adopted:

$$\mathrm{Re}_{\theta,t} = \begin{cases} \left(1173.51 - 589.428 \cdot Tu + 0.2196/Tu^2\right) F\left(\lambda_\theta\right) & Tu \leq 1.3 \\ 331.5\left(Tu - 0.5668\right)^{-0.671} F\left(\lambda_\theta\right) & Tu > 1.3 \end{cases}, \tag{40}$$

$$F\left(\lambda_\theta\right) = \begin{cases} 1 + \left[12.986\lambda_\theta + 123.66\lambda_\theta^2 + 405.689\lambda_\theta^3\right]\exp\left(-\left(\frac{Tu}{1.5}\right)^{1.5}\right) & \lambda_\theta \leq 0 \\ 1 + 0.275\left[1 - \exp\left(-35\lambda_\theta\right)\right]\exp\left(-\frac{Tu}{0.5}\right) & \lambda_\theta > 0 \end{cases}. \tag{41}$$

It is important to note that the correlations in eq. 40, 41 contain the turbulence intensity Tu. In the framework of the k–ω model, Tu can be computed using the solution to k equation. Here, we adopt the approach introduced in [39]. Specifically, $Tu = Tu_\infty$ is set for all the points of the flow field.
Moreover $\mathrm{Re}_{\theta,t}$ is computed by iterating on the value of θ_t, since $\mathrm{Re}_{\theta,t}$ is a function of θ_t itself because of the presence of λ_θ. Differently for $\mathrm{Re}_{\theta,c}$ and $\mathrm{F}_{\mathrm{length}}$ we use the correlations introduced by Malan et al. [40]:

$$\mathrm{Re}_{\theta,c} = \min\left(0.615\widetilde{\mathrm{Re}_{\theta,t}} + 61.5, \widetilde{\mathrm{Re}_{\theta,t}}\right), \tag{42}$$

It is important to note that the correlations in eq. 40, 41 contain the turbulence intensity Tu. In the framework of the k–ω model, Tu can be computed using the solution to k equation. Here, we adopt the approach introduced in [39]. Specifically, $Tu = Tu_\infty$ is set for all the points of the flow field.
Moreover $\mathrm{Re}_{\theta,t}$ is computed by iterating on the value of θ_t, since $\mathrm{Re}_{\theta,t}$ is a function of θ_t itself because of the presence of λ_θ. Differently for $\mathrm{Re}_{\theta,c}$ and $\mathrm{F}_{\mathrm{length}}$ we use the correlations introduced by Malan et al. [40]:

$$\mathrm{Re}_{\theta,c} = \min\left(0.615\widetilde{\mathrm{Re}_{\theta,t}} + 61.5, \widetilde{\mathrm{Re}_{\theta,t}}\right), \tag{43}$$

$$\mathrm{F}_{\mathrm{length}} = \min\left(\exp\left(7.168 - 0.01173\widetilde{\mathrm{Re}_{\theta,t}}\right) + 0.5, 300\right). \tag{44}$$

$\tilde{\nu}$ equation coupling with γ–$\widetilde{\mathrm{Re}_{\theta,t}}$ model

The production and destruction terms that appear in the $\tilde{\nu}$ transport equation are suitably defined as follows:

$$\begin{aligned} \mathrm{P}_{\tilde{\nu}} &= \gamma_{\mathrm{eff}} c_{b1} \tilde{S} \tilde{\nu}, \\ \mathrm{D}_{\tilde{\nu}} &= c_{w1} f_w \left(\frac{\tilde{\nu}}{d} \right)^2 . \end{aligned} \tag{45}$$

The term γ_{eff} in eq. 45 is devoted to model the separation-induced transition and it is defined as follows:

$$\gamma_{\mathrm{eff}} = \max\left(\gamma, \gamma_{\mathrm{sep}}\right) \tag{46}$$

with

$$\gamma_{\mathrm{sep}} = \min\left(2.0 \cdot \max\left[0, \left(\frac{\mathrm{Re}_{\nu}}{3.235 \mathrm{Re}_{\theta,c}}\right) - 1\right] \mathrm{F}_{reattach}, 2.0\right) \mathrm{F}_{\theta,t} \tag{47}$$

and

$$\mathrm{F}_{reattach} = \exp\left(-\frac{\mathrm{R}_{\mathrm{T}}}{20}\right)^4 . \tag{48}$$

3.5.2 γ–$\widetilde{\mathrm{Re}_{\theta,t}}$–SA20 transition model

This version of the γ–$\widetilde{\mathrm{Re}_{\theta,t}}$ transition model exactly replicates exactly the framework above described. The only difference, compared to the γ–$\widetilde{\mathrm{Re}_{\theta,t}}$–SA model, is the c_{w2} coefficient which controls the strength of the near–wall destruction term in $\tilde{\nu}$ equation, [41]. In this case, c_{w2} is replaced by the function

$$c_{w2LRe} = c_{w4} + \frac{c_{w5}}{\left(\frac{\chi}{40} + 1\right)^2} \tag{49}$$

with $c_{w4} = 0.21$ and $c_{w4} = 1.5$.
This approach was presented by Spalart and Garbaruk, [42], to reduce destruction term in the SA equation in the near–wall region to increase the skin friction.

3.5.3 $\log\gamma$–SA transition model

We also consider a second strategy to include transitional effects into the Spalart–Allmaras turbulence model. Specifically, in our approach only one equation for $\tilde{\gamma} = \log\gamma$, eq. 50, is solved to model laminar–to–turbulent transition. This method, formerly introduced by Ilinca and Pelletier, [43], is very attractive because it allows guaranteeing the positivity of the intermittency. Moreover the logarithmic distribution of a variable ensures a much smoother behaviour with the respect to the use of the primitive variable itself. This is a focal point of our approach, because the baseline model formulation exhibits blow–up of the computations.
The transport equation for $\tilde{\gamma}$ is obtained by changing $\gamma = \exp(\tilde{\gamma})$ in the intermittency equation reported in Liu et al. [44]:

$$\frac{\partial \tilde{\gamma}}{\partial t} + \frac{\partial}{\partial x_j}\left(u_j \tilde{\gamma}\right) = \mathrm{P}_{\tilde{\gamma}} - \mathrm{D}_{\tilde{\gamma}} + \frac{\partial}{\partial x_j}\left[\left(\nu + \nu_t\right) \frac{\partial \tilde{\gamma}}{\partial x_j}\right] + \left(\nu + \nu_t\right) \frac{\partial \tilde{\gamma}}{\partial x_j} \frac{\partial \tilde{\gamma}}{\partial x_j} . \tag{50}$$

Production and destruction terms for $\tilde{\gamma}$ equation have the following expressions:

$$\mathrm{P}_{\tilde{\gamma}} = \mathrm{F}_{\mathrm{length}} S \left(1 - e^{\tilde{\gamma}}\right) \mathrm{F}_{\mathrm{onset}} \qquad \mathrm{D}_{\tilde{\gamma}} = c_{a2} \Omega \mathrm{F}_{\mathrm{turb}} \left(c_{e2} e^{\tilde{\gamma}} - 1\right) \mathrm{F}_{\mathrm{onset}} . \tag{51}$$

$\mathrm{F_{onset}}$ term in eq. 51 is defined as in the γ–$\widetilde{\mathrm{Re}_{\theta,t}}$ framework. Differently, $\mathrm{F_{onset,2}}$ and $\mathrm{F_{onset,3}}$ are re–calculated as follows:

$$\begin{aligned}\mathrm{F_{onset,2}} &= \min\left(\mathrm{F_{onset,1}}, 2.0\right), \\ \mathrm{F_{onset,3}} &= \max\left(1 - \left(\frac{\mathrm{R_T}}{3.5}\right)^3, 0\right).\end{aligned} \tag{52}$$

As regards $\mathrm{F_{turb}}$, the following relation in adopted for this LCTM model:

$$\mathrm{F_{turb}} = \exp\left(-\frac{\mathrm{R_T}}{2}\right)^4. \tag{53}$$

We want also to remark that the constants c_{a2} and c_{e2} assume the same values reported in eq. 37. The parameter $\mathrm{F_{length}}$ is fixed at 0.5 as in Lit et al. [44] in order to achieve a smooth growth of the intermittency. On the other hand, $\mathrm{Re}_{\theta,c}$ is here defined as:

$$\mathrm{Re}_{\theta,c} = f_{local}\left(Tu_l\right) f_{far}\left(Tu_\infty\right), \tag{54}$$

where

$$\begin{aligned}f_{local}\left(Tu_l\right) &= 803.73\left(Tu_l + 0.6067\right)^{-1.027}, \\ f_{far}\left(Tu_\infty\right) &= -3.162 Tu_\infty^2 - 0.4565 Tu_\infty + 1.7.\end{aligned} \tag{55}$$

Looking at eqs. 54, 55, it is very easy to note that both the local turbulence intensity and the far–field turbulence information are involved. This is an interesting feature of the $\log\gamma$–SA correlation based transition model. Indeed, a local turbulence intensity controlling term, f_{local}, is adopted to reflect the effect of local turbulence intensity variation on $\mathrm{Re}_{\theta,c}$. The formulation of Cakmakcioglu [?] is used for the local turbulence intensity, Tu_l.

The integration of the $\log\gamma$ model and the Spalart–Allmaras turbulence model is handled using a scheme similar to the γ–$\widetilde{\mathrm{Re}_{\theta,t}}$ one. The production term of the modified turbulent viscosity, $\mathrm{P}_{\tilde{\nu}}$, is treated exactly as in eq. 45. However, for the coefficient γ_{sep} we use a correlation similar to one suggested by Liu et al. [44]:

$$\gamma_{sep} = \min\left(8.0 \max\left[0.0, \left(\frac{\mathrm{Re}_\nu}{2\mathrm{Re}_{\theta,c}}\right) - 1\right], \gamma_{lim}\right) \tag{56}$$

in the above presented equation, γ_{lim} is a user defined parameter imposed equal to 2.5. As regards the destruction term appearing in turbulence equation, $\mathrm{D}_{\tilde{\nu}}$, we use the same approach proposed by Liu et al. [44]:

$$D_{\tilde{\nu}} = \min\left(\max\left(\gamma, 0.5\right), 1.0\right)\left[c_{w1} f_w \left(\frac{\tilde{\nu}}{d}\right)^2\right]. \tag{57}$$

3.5.4 Boundary conditions

Boundary conditions for $\tilde{\nu}$ are standard: $\tilde{\nu}_\infty = 3\nu$ at the free stream and $\tilde{\nu} = 0$ at the wall, whereas the boundary condition for γ at the wall is a zero normal gradient. At the inlet, the intermittency is set to 1. The boundary condition for $\widetilde{\mathrm{Re}_{\theta,t}}$ at the wall is zero flux; differently, a fixed value condition is adopted at inlet for $\widetilde{\mathrm{Re}_{\theta,t}}$. This value is calculated from the specific empirical correlation based on the inlet turbulence intensity.

All the grid used in the following are able to guarantee a viscous sub-layer scaled first cell height, y^+, of approximately 1. The value of y^+ is estimated as $y^+ = \frac{u_\tau}{\nu} y_c$, where $u_\tau = \sqrt{\tau_w/\rho}$ is the friction velocity, τ_w is the viscous stress component measured at the wall, and y_c is the height of the cells next to the wall.

3.6 University of Strasbourg

The University of Strasbourg interest during the project was to implement different strategies to improve the numerical simulation of the laminar separation bubble. Reynolds Averaged Navier-Stokes "RANS" turbulence models are coupled with additional transport equations to model the correct turbulence development and level in the beginning of the separation and inside the re-circulation. RANS models can capture separations inside turbulent boundary layers, but in this case the recirculation bubble is situated in the laminar region in addition to the transition location. The recirculation length is also a challenging task and therefore a modification of the turbulent production and the dissipation is necessary to ensure better resolution of the laminar transition to turbulence for low Reynolds number applications.

The numerical simulations are carried out with the Navier Stokes Multi-Block NSMB solver [45, 46], which includes an ensemble of the most efficient CFD methods, as well as adapted fluid–structure coupling for moving and deformable structures. These developments can be found in [47], regarding URANS modelling for strongly detached flows [48, 49, 50], for Detached Eddy Simulation (DES) with the NSMB code. University of Strasbourg has computed real-scale high Reynolds number unsteady turbulent flows thanks to advanced turbulence modelling approaches as improved DDES (Delayed Detached Eddy Simulation) and OES (Organised Eddy Simulation) [51], that have proven very efficient for simulating critical flow dynamics around 3D wings, to predict separation bubbles and transition locations. Recent studies carried using NSMB solver and the OES approach captured separation bubbles and the recirculation near the trailing-edge due to the high angles of attack. University of Strasbourg has also recently participated in a European project SMS on the topic dynamic deformation of wings trailing edge (morphing wings) at subsonic and transonic speed ranges. The vibration in the subsonic speed creates small vortices injected directly in the wake. These bubbles interact with the shear-layer instabilities and von Kàrmàn vortices thanks to the OES turbulence model approach that was able to capture this unsteadiness [52, 53]. In addition, in the transonic speeds, the TE vibration interacts with the Shock Wave Boundary Layer (SWBL) region specially in the buffet configurations [54]. University of Strasbourg is participating in parallel in AFC4TR clean sky project, aiming to simulate subsonic flows around tiltrotors by adding ZNMF (Zero Net Mass Flux) piezoactuators acting as jet and coupled directly with the boundary layer helping the reattachment of flow to increase the aerodynamic performances [55]. With all these tools in the project Garteur, the focus will be on the physical understanding of the laminar separation using different turbulence models based on transition.

3.6.1 Description of the solver

NSMB is developed in a consortium composed of different universities and industries and was mainly used for aeronautics and aerospace applications over the past 30 years. NSMB has a parallel and a vectorial structure and it can run on high-performance computers to solve a wide range of industrial aerodynamics design problems. NSMB solves the Reynolds-averaged Navier Stokes equations for compressible flows on multi-block structured grids. NSMB offers all functionalities of a modern CFD code used for aerospace applications, among others, ALE (Arbitrary Lagrangian Eulerian) approach [56], turbulence models, [47], chemistry modelling, grid flexibility, FSI (Fluid-Structure Interactions) coupling such as morphing wings modelling, Chimera overlapping technique. Space discretization schemes include 2nd- and 4th-order central schemes with artificial dissipation and various upwind schemes (Roe, AUSM, Van Leer ...) up to 5th order. Time integration methods are explicit (Runge-Kutta schemes) or implicit (LU-SGS) schemes. Convergence acceleration as multigrid, local time stepping, preconditioning, full multigrid can be used to accelerate the convergence. NSMB also includes a large variety of well tested and validated turbulence models that are standard in the aeronautical industry, like the one-equation Spalart-Allmaras, [57], the Organized Eddy Simulation model, or the two-equation by Menter [58], that have been applied in the present study. In this study RANS simulations are carried out for different test cases.

3.6.2 Turbulence modelling

Transition models are implemented in the 1 equation Spalart-Allmaras model and the 2 equation K-ω-SST model and summarized in the following table: These turbulence models based on transition modelling are used for different selected test cases and compared with fully turbulent models (without transition) in addition to the experimental data. The results are regrouped and compared with the other partners.

Number of additional equations	Turbulence model
0	Spalart-Allmaras Bas-Cakmakcioglu-Mura [59]
1	γ model of Langtry et. al [60]
2	Original γ-R_θ model of Langtry-Menter [61]

Table 4: Coefficients for the fitting function.

3.6.3 DARPA EQUiPS

University of Strasbourg, through a visiting Professor, has also worked on a method based on uncertainty quantification.

Assessing the errors in turbulence modelling is an active research field, as discussed for instance in the review papers [62, 63] and references therein. Several approaches have been put forward over the past few years. For convenience, the DARPA EQUiPS ("Enabling Quantification of Uncertainty in Physics Simulation") module developed for the SU2 CFD suite has been chosen. This module was made available to SU2 users along with a complete tutorial [1].

The EQUiPS module focuses specifically on the estimation of uncertainties arising due to turbulence closure models [64]. The rationale behind this approach directly addresses the limitations of classical turbulence models, primarily those associated with the eddy viscosity hypothesis. The methodology is presented in Ref. [65, 63, 64] and consists in a comprehensive framework providing effective eigenspace perturbations. This allows directly addressing the anisotropy of the turbulent stress tensor and the turbulent production.

The rationale behind the methodology may also be summarized by stating that eddy-viscosity hypothesis prescribes identical eigenvectors for the modeled Reynolds stress tensor and the mean rate of strain tensor; whereas this is true in simple shear flows, it is not necessarily true in complex engineering flows [66, 67, 68].

Within the EQUiPS module, the perturbations added are defined with reference to the barycentric map [69] (figure 7). The EQUiPS module was applied to the transitional SST Langtry-Menter model. Whereas there are no inconsistencies, no other applications are available in the literature. It is also worthwhile mentioning that in the implementation in SU2 the perturbations are introduced via a relaxation factor which cannot be raised above a problem specific threshold.

Five simulations perturbating the Reynolds tensor plus a simulations without any perturbation have been performed for the flow around the SD 7003 airfoil at Re=6.0×10^4 and $\alpha = 4°$. In

---

[1] `https://su2code.github.io/tutorials/UQ_NACA0012/`

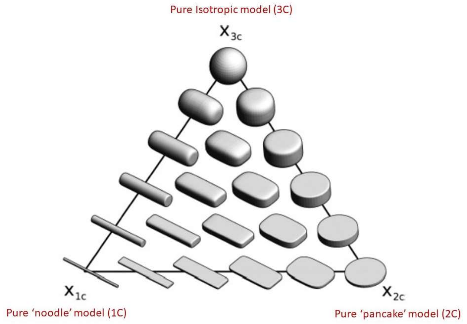

Figure 7: All possible models (with given a set of eigenvectors) of the Reynolds stress tensor

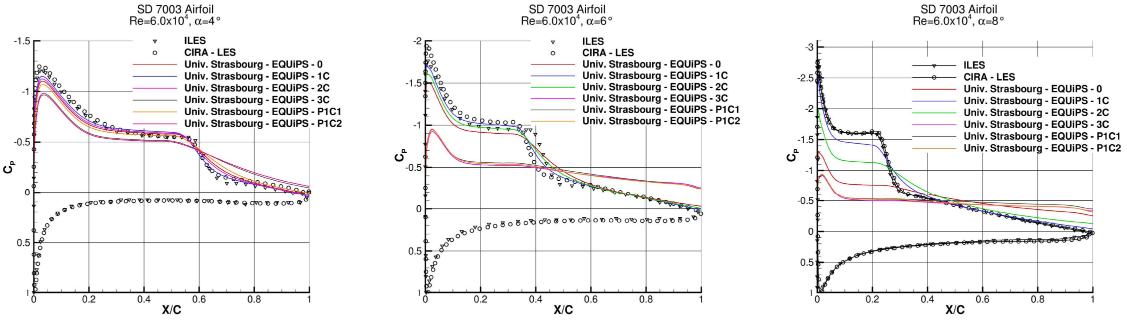

(a) $\alpha = 4^{\circ}$ (b) $\alpha = 6^{\circ}$ (c) $\alpha = 8^{\circ}$

Figure 8: Pressure coefficients over the SD7003 airfoil at $\mathbf{Re}_{\infty} = \mathbf{6.0} \times \mathbf{10^4}$.

the figures 8 and 9, the results obtained without adding any perturbation to the Reynolds stress tensor are indicated with "0". The symbols "1C", "2C" and "3C" concern perturbations of the eigenvalues of the stress tensor, which in practice modify the shape of the Reynolds stress ellipsoid but not its orientation. The symbols "P1C1" and "P1C2" refer to perturbations of the eigenvectors of the stress tensor, which implies modifying the orientation of the Reynolds stress ellipsoid. In particular, "P1C1" aligns the eigenvectors of the Reynolds stress tensor with those of the flow strain rate, besides introducing the eigenvalues perturbation "1C". "P1C2" aligns the eigenvectors of the Reynolds stress tensor with those of the flow strain rate, besides introducing the eigenvalues perturbation "2C". The friction and pressure coefficients obtained by perturbating the eigenvalue corresponding to the pure "noddle" model "1C" are the closest to the reference LES values.

Unsurprisingly, the results presented for the SD7003 airfoil show large differences between the predictions obtained from the five perturbations of the stress tensor eigenspace. It is worth noting that the perturbation maximising turbulence production leads to the earlier transition.

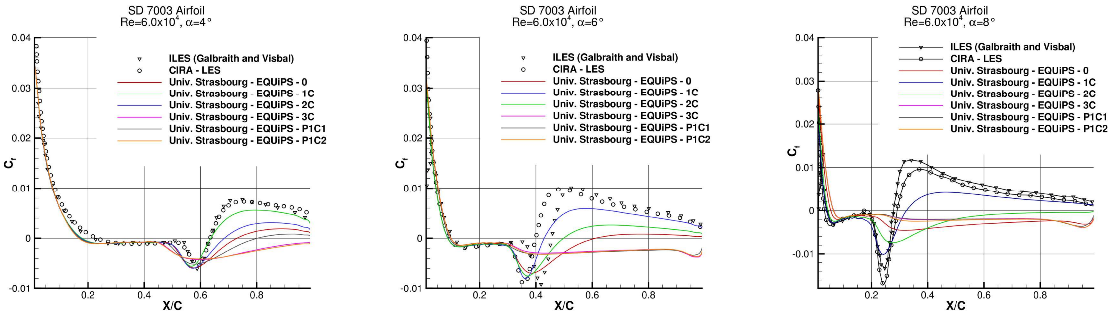

(a) $\alpha = 4°$ (b) $\alpha = 6°$ (c) $\alpha = 8°$

Figure 9: Skin friction coefficients over the SD7003 airfoil at $\mathbf{Re}_\infty = \mathbf{6.0} \times \mathbf{10^4}$.

4 Structure and Activities

The project is structured into four work packages, work package 1 and 2 deal with incompressible flows at low and high Reynolds number respectively, while work package 3 faces with transonic flows at low Reynolds numbers. The issue of instability analysis of laminar separation bubbles is addressed in the last work package.

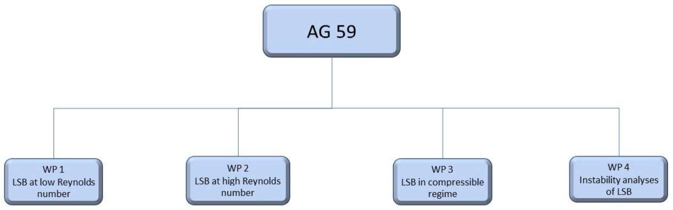

Figure 10: Work Breakdown Structure

Several test cases have been identified for each work package as summarized in the following table.

4.1 WP 1: Laminar separation bubbles at low Reynolds number

The work package 1 faces with the numerical simulation of laminar separation bubbles in the range of Reynolds number 10^4-10^5. The following test cases have been considered.

4.1.1 Backward facing step

The backward facing step flow is a classical test case very useful to analyze the transition inside laminar separation bubble. In fact, the separation point is fixed by the geometry and only the evolution inside the bubble determines the reattachment point. The reference test case is based on the investigations by Armaly et al[70], and a sketch of the geometry is shown in fig. 11.

Table 5: Structure of the AG59 project

WP	Test case
1	Backward facing step
1	SD 7003 airfoil at Re=6.0×10^4
1	Eppler 387 airfoil at Re=2.0×10^5
1	NACA 0015 airfoil at Re=1.8×10^5
2	Flat plate with adverse pressure gradient
2	S809 airfoil at Re=2.0×10^6
3	Triangular airfoil in WT
4	SD7003 airfoil at Re=6.0×10^4
4	NACA 0015 airfoil at Re=1.8×10^5

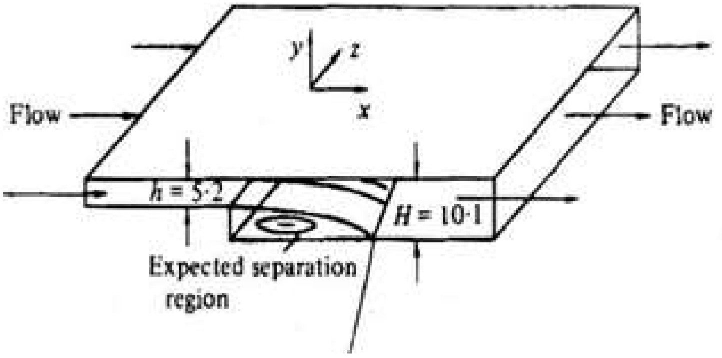

Figure 11: Backward facing step geometry

Figure 12(a) shows the experimental separation and reattachment points as function of the Reynolds number, while fig. 12(b) is representative of the adopted nomenclature. The Reynolds number is defined as $Re = \frac{VD}{\nu}$, where V is the mean inlet velocity, ν is the dynamic viscosity and $D = 2h$ is the reference length equal to twice the height h of the inlet channel, as in fig. 11.

CIRA and Univ. of Strasbourg performed simulations at $Re = 1500$, 1800 and 2000, while Univ. of Southampton covered a wider range from $Re = 1095$ to 6000. The adopted turbulent and transition models and grid data are listed in table 6.

Figure 13 shows the results from CIRA and Univ. of Strasbourg, compared with the experimental data. For the three Reynolds numbers, CIRA solutions do not return the separation bubble on the lower side, providing only the separation/reattachment points labelled x_1, x_4 and x_5. The computed values are always upstream with respect to the corresponding experimental data. Simulations performed by Univ. of Strasbourg compute the bubbles on the lower and upper side of the channel for all cases. The locations are downstream the experimental data regardless of the adopted turbulence and transition models, noteworthy the $\kappa - \omega$ SST model in coupling with the $\gamma - Re_\theta$ model, available only at $Re = 1500$, predicts closer values to the experiments.

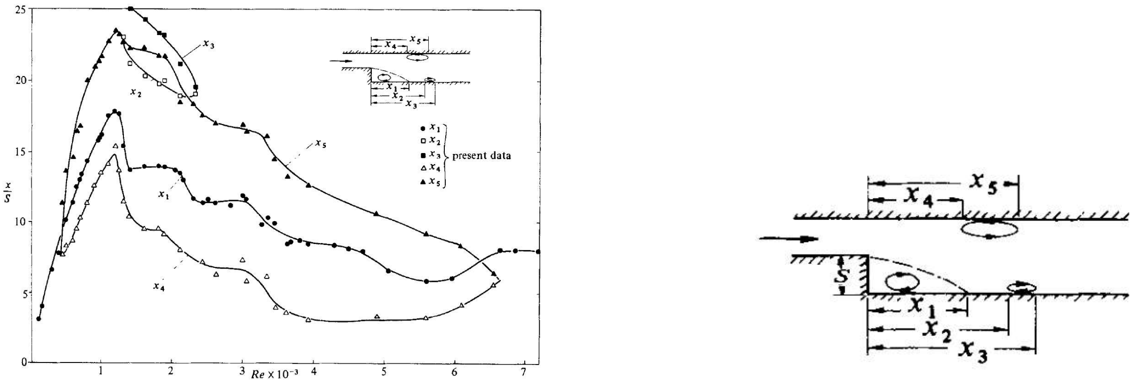

(a) Experimental values (b) Nomenclature

Figure 12: Measured location of separation and reattachment points vs Reynolds number

	CIRA	SOTON	UNISTRA
GRID	Structured	?	Structured
No of cells	$115K$	?	$30K$
Tu_∞	1.5%	?	1.29%
Turbulent and transition model	$\kappa - \omega SST + \gamma$	?	SA+γ SA+$\gamma - Re_\theta$ $\kappa - \omega SST + \gamma - Re_\theta$

Table 6: BFS settings for turbulent and transition models

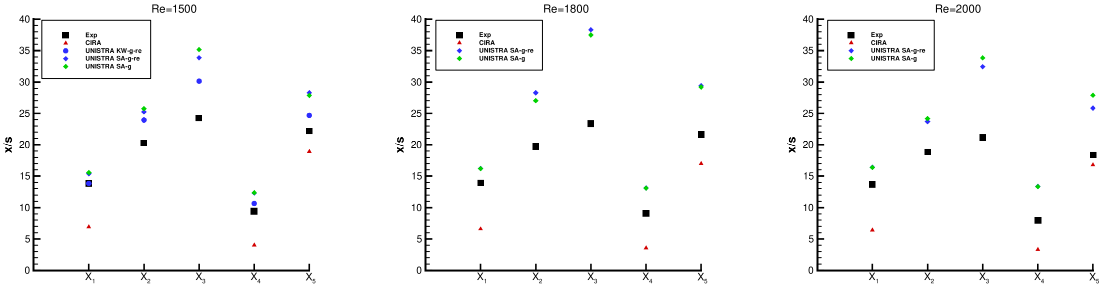

(a) $Re = 1500$ (b) $Re = 1800$ (c) $Re = 2000$

Figure 13: Experimental data vs CFD

The results from Univ. of Southampton are shown in fig. 14. For these cases, it is not possible to state a common trend, being it always downstream or upstream with respect to the experimental data. Considering the case at $Re = 1295$, the agreement is fairly good and in line with the prediction of Univ. of Southampton at $Re = 1500$.

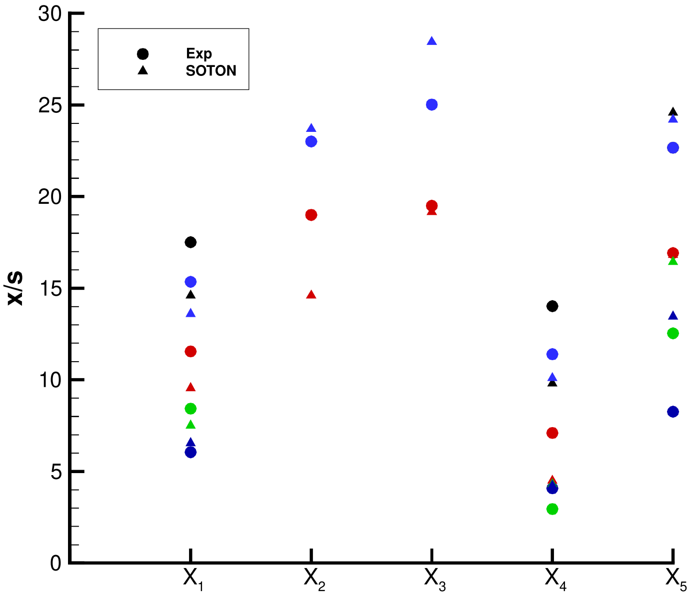

Figure 14: BFS text case. $Re = 1095$: black, $Re = 1295$: blue, $Re = 2500$: red, $Re = 4000$: green, $Re = 6000$: purple.

4.1.2 SD7003 airfoil

The incompressible flow around the Selig-Donovan (SD) 7003 airfoil at Reynolds number of 6.0×10^4 presents very interesting characteristics. A long laminar separation bubble is present on the upper surface of the airfoil. This bubble moves upstream as the incidence increases. At high incidence ($\alpha > 10°$), both the separation and the re-attachment point of the bubble do not vary considerably but the recovery of pressure decreases. As α still increases, a separation appears downstream of the bubble in the central part of the upper surface of the airfoil. The flow is characterized by a short bubble in the leading edge zone and by a separated zone in the following turbulent region. Vortices are shed from the laminar separated region in the forward part of the airfoil and flow into the next turbulent separated region. A large vortex is then convected from the airfoil. The stall of the airfoil occurs when the laminar bubble present in the leading edge region and the turbulent separated region join together [3, 4].

Pressure and friction coefficients at several incidences are shown in the figures 15 -18. The results have been achieved by CIRA and UNIVPM by applying several turbulence models and are compared to literature LES data [71, 72, 3, 4, 14]. All the turbulence models employ one (γ) or two (γ and $\Re_\theta$) equations for modelling the transition. UNIVPM makes use of the Spalart-Allamaras while CIRA of the $\kappa - \omega$ SST as "base" model. The results obtained by University of Strasbourg by the EQUiPS model with the "1C" eigenvalue perturbation are also reported.

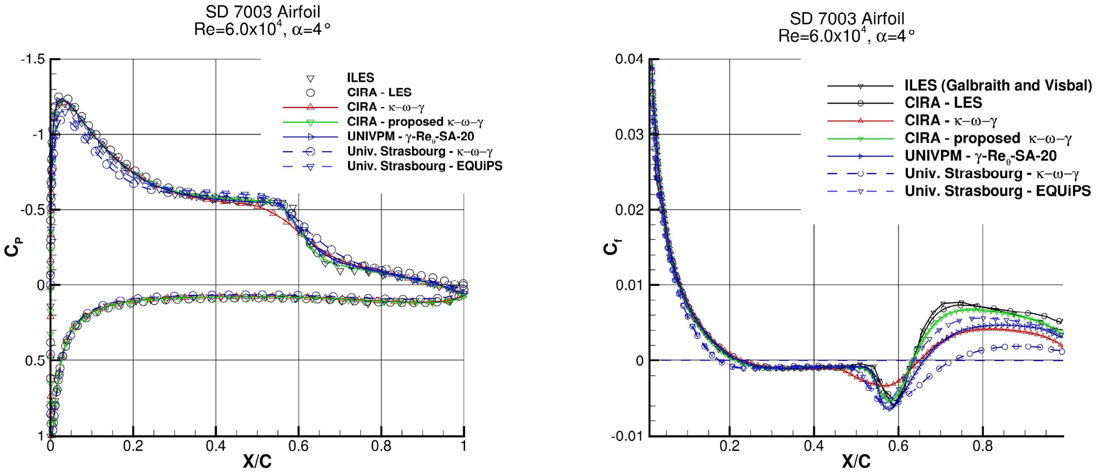

(a) Pressure coefficient (b) Skin friction coefficient

Figure 15: Pressure and friction coefficients over the SD7003 airfoil at $\mathbf{Re}_\infty = \mathbf{6.0} \times \mathbf{10^4}$ and $\boldsymbol{\alpha} = \mathbf{4}^\circ$.

At $\alpha = 4^\circ$, the two LES data are in very good agreement between them. The model proposed by CIRA (section 3.1.2) [16] remarkably improves the results of the $\kappa - \omega - \gamma$ SST model achieving an excellent comparison with LES data for the bubble and for pressure levels. The Spalart Allmars $\gamma - \Re_\theta$-20 (section 3.5.2) model provides a good results for pressure coefficient with a slight over-prediciton of the bubble length and an under-prediction of friction levels in the re-attachment region. A good result is also shown by the EQUiPS model.

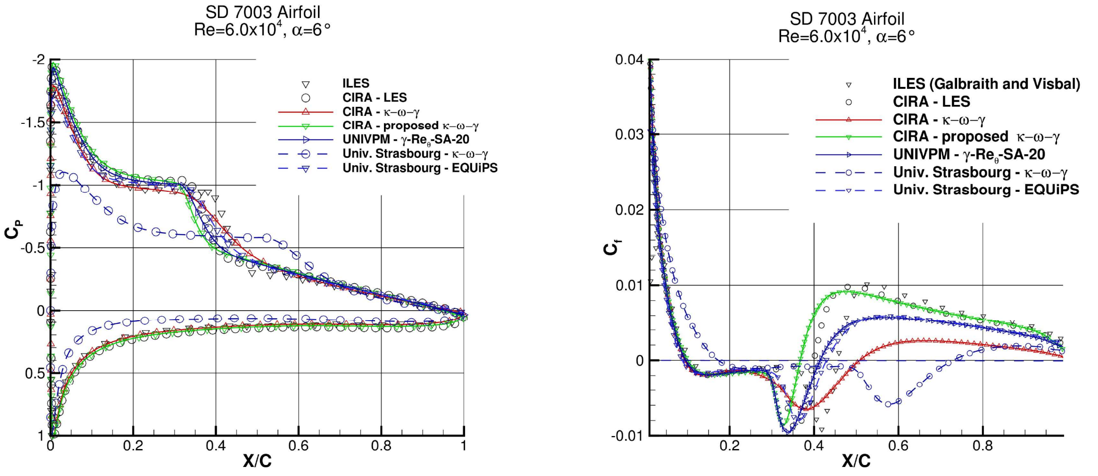

(a) Pressure coefficient (b) Skin friction coefficient

Figure 16: Pressure and friction coefficients over the SD7003 airfoil at $\mathbf{Re}_\infty = \mathbf{6.0} \times \mathbf{10^4}$ and $\boldsymbol{\alpha} = \mathbf{6}^\circ$.

At $\alpha = 6°$, there is a discrepancy between the LES data mainly in the skin friction coefficient. The CIRA proposed model is in good agreement with the large eddy simulation by CIRA with an overprediciton of the bubble length. The UNIVPM results are also in good agreement with the CIRA LES and present a slight overprediction of the bubble length with and underprediction of the friction levels downstream the bubble. The $\kappa - \omega - \gamma$ model by University of Strasbourg has provided a not converged result while the UQUiPS approach has shown a good result very close to the Spalart Allmaras $\gamma - \widetilde{\mathrm{Re}}_{\theta,t}$-20 model.

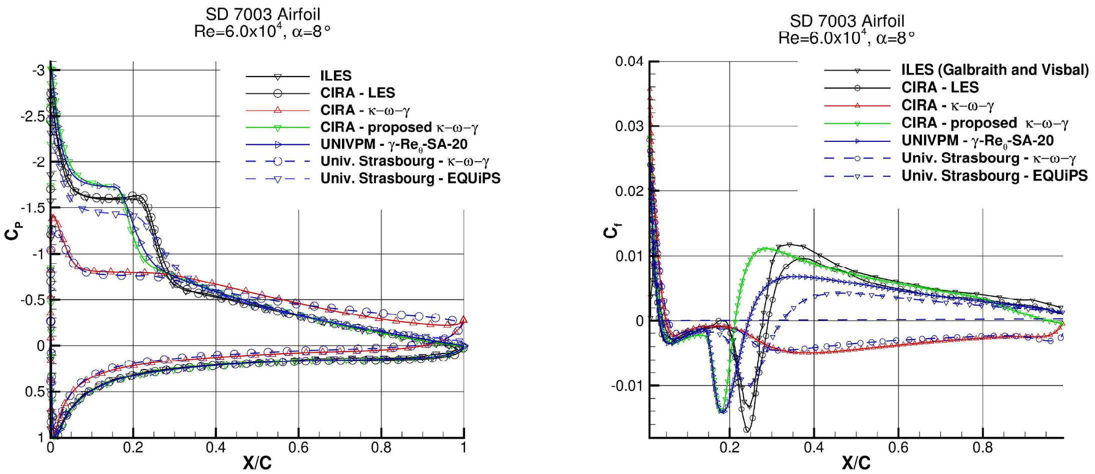

(a) Pressure coefficient

(b) Skin friction coefficient

Figure 17: Pressure and friction coefficients over the SD7003 airfoil at $\mathbf{Re}_\infty = \mathbf{6.0} \times \mathbf{10^4}$ and $\boldsymbol{\alpha} = \mathbf{8}°$.

At $\alpha = 8°$, the two set of LES data are in very good agreement. The “base” $\kappa - \omega - \gamma$ model shows a very poor convergence. Instead, the CIRA proposed model provides a good result. Both UNIVPM and CIRA data overpredict the pressure level on the upper surface of the airfoil whereas the EQUiPS model provides an underestimation of the C_P. However, a difference between all RANS and LES data in present at this incidence in both C_P and C_f distribution with an underprediciton of the bubble length.

At $\alpha = 10°$ only the RANS data by UNIVPM and the CIRA LES results are available. The incidence is crucial because flow is approaching the stall. The laminar bubble is advanced to the leading-edge region and the pressure recovery downstream the bubble is very weak. The flow is about to separate for LES and is already separated in the RANS results.

Three sets of experimental data are available in literature and have been taken as reference for the aerodynamic coefficients. The measurements from Selig *et al.* at University of Princeton in 1989 [73] and at University of Illinois in 1996 [74] and from Ol *et al.* at Horizontal Free-Surface Wind tunnel (HFWT) at Air Force Research Laboratory in 2005 [30]. The data consists of lift and drag coefficient at several incidences.

The comparison with the numerical data is reported in figure 19 in terms of lift coefficient and

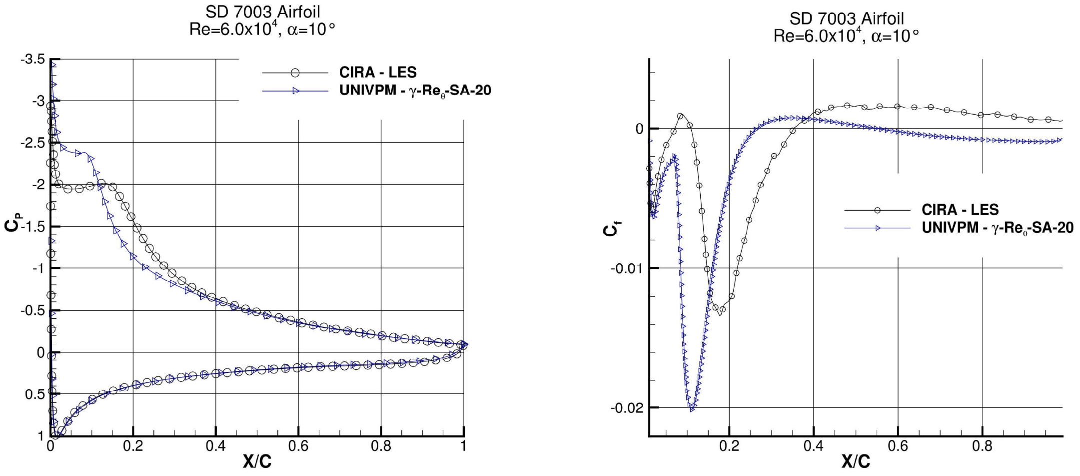

(a) Pressure coefficient

(b) Skin friction coefficient

Figure 18: Pressure and friction coefficients over the SD7003 airfoil at $\mathbf{Re}_\infty = \mathbf{6.0} \times \mathbf{10^4}$ and $\boldsymbol{\alpha} = \mathbf{10}^\circ$.

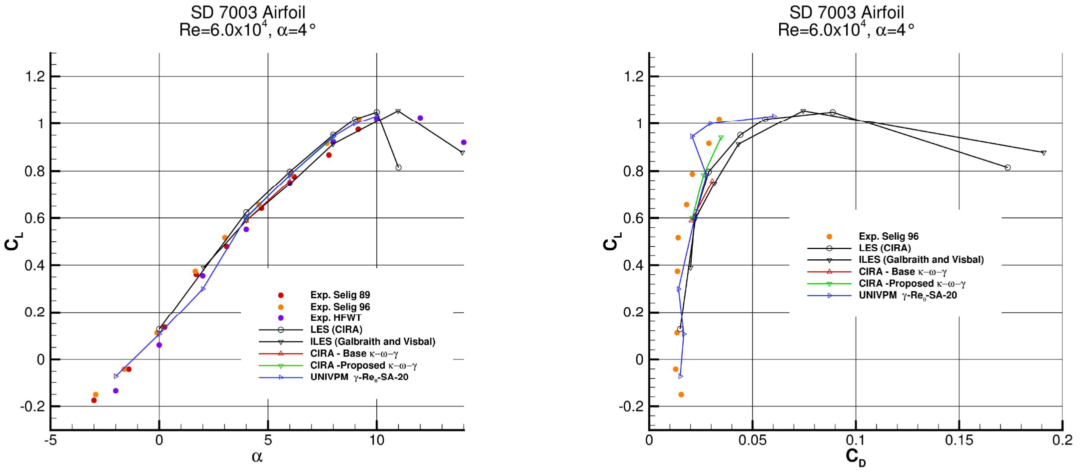

(a) Lift coefficient

(b) Drag polar

Figure 19: Aerodynamic coefficients over the SD7003 airfoil at $\mathbf{Re}_\infty = \mathbf{6.0} \times \mathbf{10^4}$.

drag polar. All the models employed agree well with the experimental data in the linear part of the lift curve. The RANS results by UNIVPM well follow the experiments up to high incidence The behaviour at the stall is present only in the HFWT data and is well predicted by the implicit LES. The LES by CIRA, instead, shows an anticipated stall. The RANS results by UNIVPM well follow the experiments up to high incidence.

The numerical data generally present an overprediction of the experimental drag coefficients.

available only in Selig 1996. The UNIVPM data present a sort of laminar ”bag” at a lift coefficient around $0.9 - 1.0$

4.1.3 E387 airfoil

The E387 airfoil at Re $= 2 \cdot 10^5$ was also studied. The specific case was selected since a large and accurate data set of experimental measurements was published by McGhee et al., [75]. The results reported in the following were computed using a structured C–shaped computational grid having about $2.22 \cdot 10^5$ cells. The inflow and outflow boundaries were placed at about 10 times the airfoil chord, c, from the airfoil. The cells were clustered near the airfoil surface and the viscous sub–layer scaled first cell height next to the wall is such that $O\left(y^+\right) \simeq 1$.
As in the other test cases, different turbulence models have been used. Marche Polytechnic University applied two versions of the Spalart-Allmaras model. Differently, University of Strasbourg used three different transition approaches for both Spalart–Allmaras and k–ω SST turbulence models.
Pressure coefficient obtained are, in general, very consistent with experimental data. This is particularly true for the angles of attack prior to the stall region ($\alpha < 10°$). However, SST k–ω BCM model was not able to predict transition and the related results seem to more similar to a fully turbulent mode.
A particular mention have to be devoted for $\alpha = 8°$. McGhee et al. observed a LSB near to the leading edge at $\alpha = 8.5°$, while a natural transition in boundary layer was evidenced at $\alpha = 8°$. This behaviour may contribute to explain the discrepancy between the all the numerical and experimental data which can be noted in Fig. 21.

The force coefficients, showed in Fig. 22, confirm the very good consistency between almost all the models here adopted and experimental data prior to the stall region. In this case, it is very easy to note as log γ–SA model implementation of Marche Polytechnic University put in evidence the worst behaviour in the stall detection.

4.1.4 NACA0015 airfoil

The NACA 0015 airfoil at $Re = 1.8 \times 10^5$ and $\alpha = 3°$ and $10°$ was also studied. Experimental data recently published [76, 77] and a LES performed at $\alpha = 10°$ [14] are considered as reference. Different turbulence models have been used. CIRA applied the $\kappa - \omega - \gamma$ in the basic form [9] and a proposed version [16] described in the section 3.1.2. Marche Polytechnic University applied two versions of the Spalart-Allmaras model. The flow resulted difficult to be reproduced by the numerical methods, especially at $\alpha = 3°$ with the bubble covering a large portion of the upper surface. This is somehow also confirmed by the experiments, that present a large scatter of the data and a quite complex flow topology at the low incidences [76, 77].

The data for the flow at $\alpha = 10°$ are reported in the figures 24 Also a large eddy simulations [14] is considered for sake of comparison. At this incidence, the flow presents a laminar bubble in the front part of the airfoil followed by a strong pressure recovery. The flow is close to the separation also in the rear region.

The skin friction coefficient is shown in figure 24. The experimental C_f has been extracted from the data, achieved by Temperature Sensitive Paints (TSP), by two unrelated algorithms, and two set of data are reported in figure 24. One is based on the time lag that maximizes the temporal correlation between stream-wise aligned points; the other is based on an optical flow analogy obtained from the asymptotic expansion of the energy equation at the wall [78]. The C_f obtained by the temporal correlation is the one that better agrees with the LES results. The proposed model provides results clearly improved with respect to the base model and in good agreement with both LES and

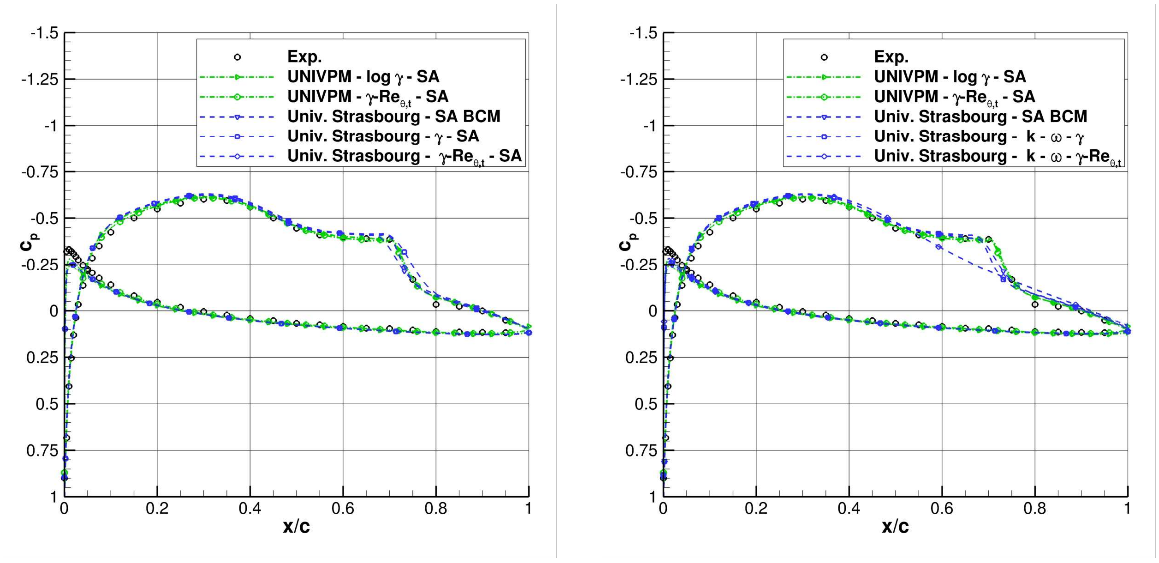

(a) $\alpha = 0°$, SA models. (b) $\alpha = 0°$, SA and k–ω models.

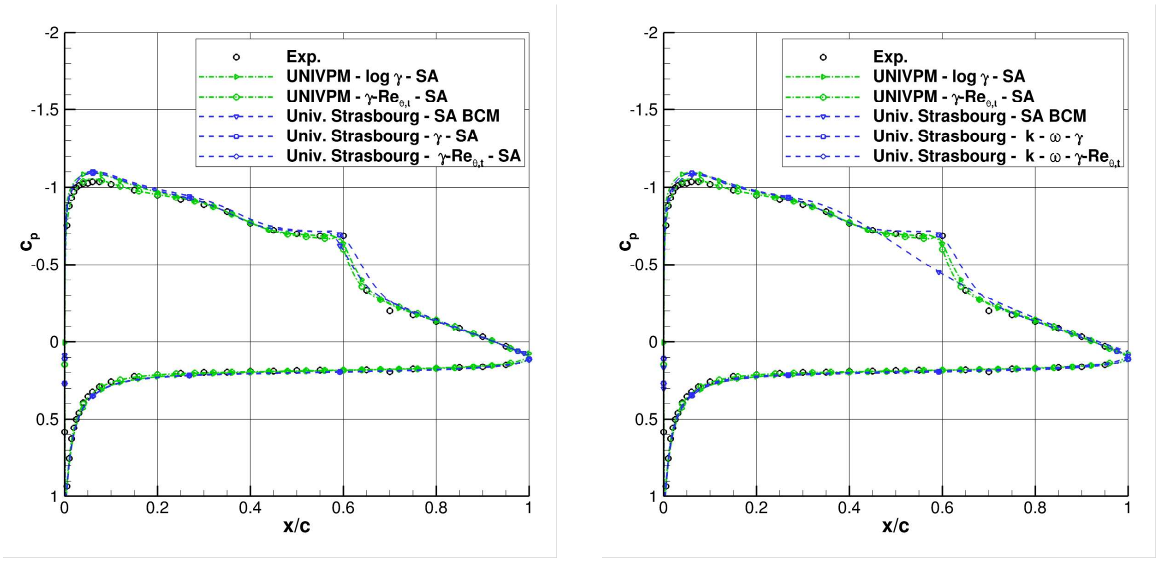

(c) $\alpha = 4°$, SA models. (d) $\alpha = 4°$, SA and k–ω models.

Figure 20: Pressure coefficients over the E387 airfoil at $\mathbf{Re}_\infty = \mathbf{2 \cdot 10^5}$

experimental data. The separation and the reattachment points are slightly shifted, the pressure recovery is fairly good, while a separated region is present in the trailing-edge zone.

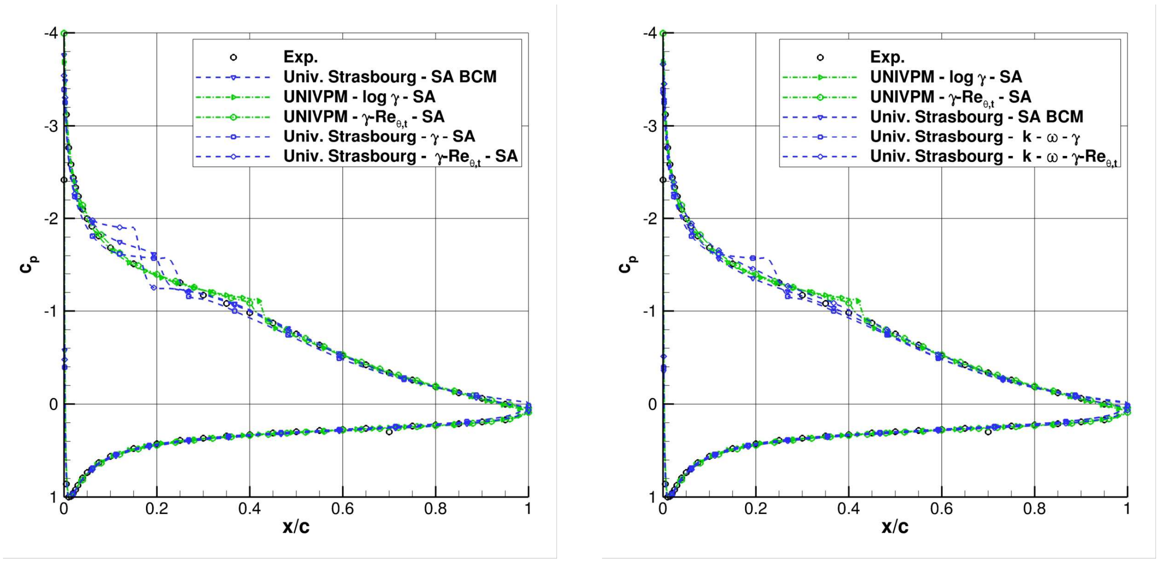

(a) $\alpha = 8°$, SA models.

(b) $\alpha = 8°$, SA and k–ω models.

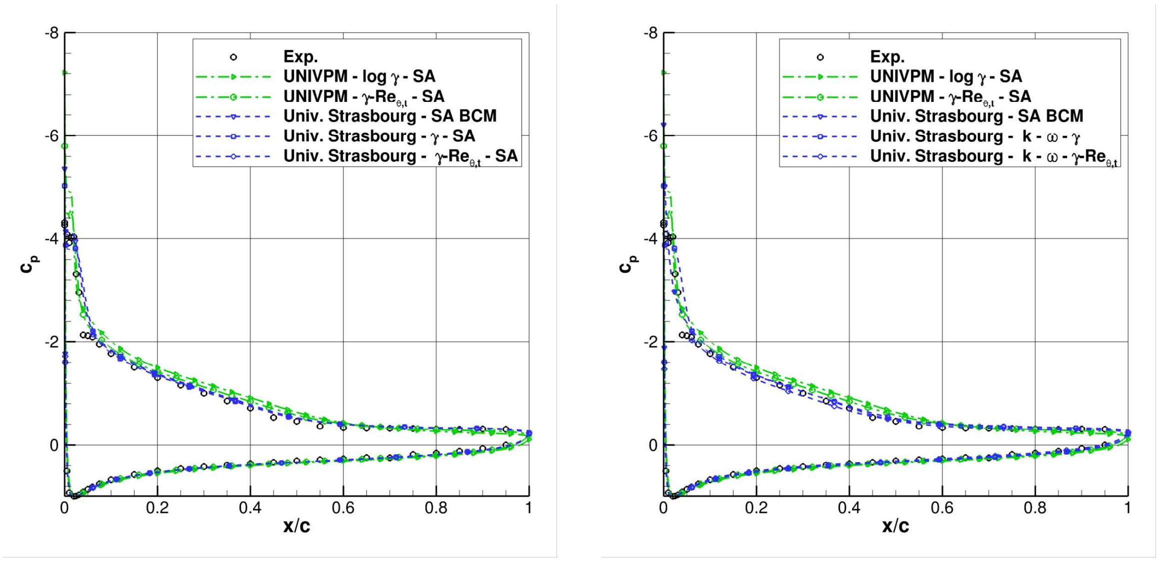

(c) $\alpha = 12°$, SA models.

(d) $\alpha = 12°$, SA and k–ω models.

Figure 21: Pressure coefficients over the E387 airfoil at $\mathbf{Re}_\infty = \mathbf{2 \cdot 10^5}$

4.1.5 NACA0012 airfoil

This test case was built by ONERA in order to investigate low Reynolds number laminar separation bubbles both experimentally and numerically. The experimental tests were conducted in S2L wind tunnel, shown in Fig. 25. S2L is an open circuit low-speed wind tunnel with an operational test velocity $\in (4,\, 45)\,\mathrm{m} \cdot \mathrm{s}^{-1}$. The test section has an octagonal shape of 1 m of diameter and 2 m of length, with a divergence rate of 1.5%. The tested airfoil was a NACA0012 of 0.2m of chord and

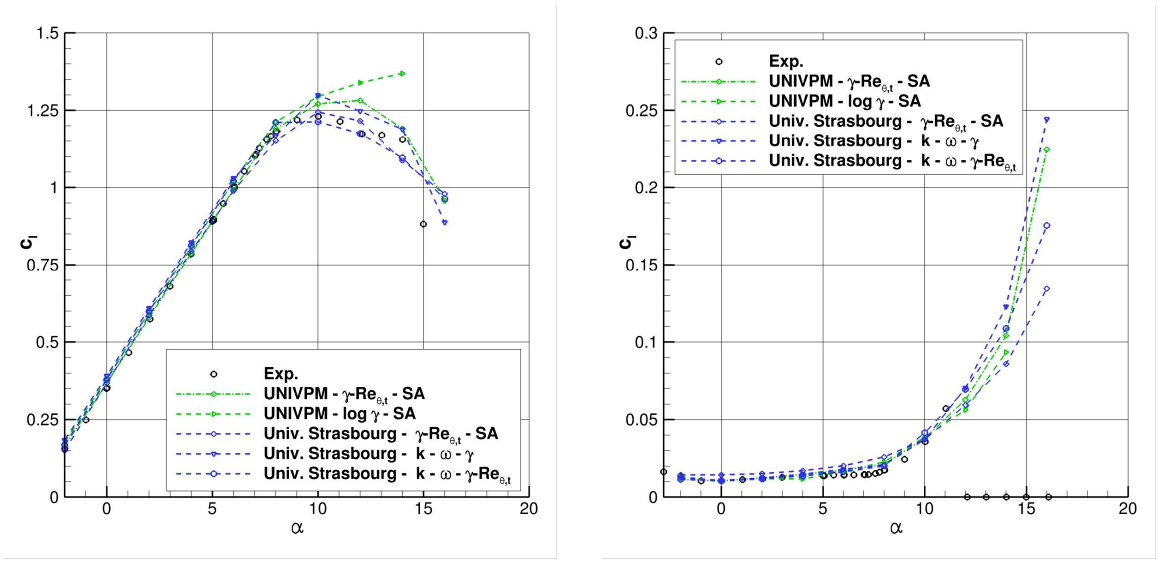

(a) c_l–α

(b) c_d–α

Figure 22: the E387 airfoil at $\mathbf{Re}_\infty = \mathbf{2 \cdot 10^5}$, forces coefficients.

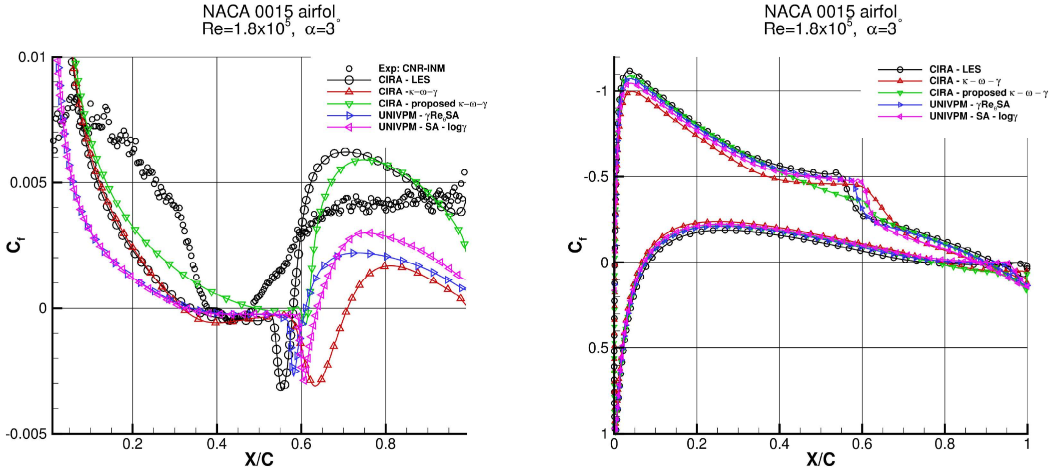

(a) Skin friction coefficient

Figure 23: Pressure and friction coefficients over the NACA 0015 airfoil at $\mathbf{Re}_\infty = \mathbf{1.8 \times 10^5}$ and $\boldsymbol{\alpha} = \mathbf{3}°$.

0.93m of span. The overall configuration is shown in Fig. 26.

The tests were conducted for several angle-of-attack and chord-based Reynolds number, as shown in Fig. 27. A small subset of cases (marked from Ⓐ to Ⓔ in Fig. 27) were chosen in order to investigate the influence of angle-of-attack and Reynolds number compared to numerical simulations.

Fig. 28 shows a comparison of pressure coefficient distributions between experimental data and

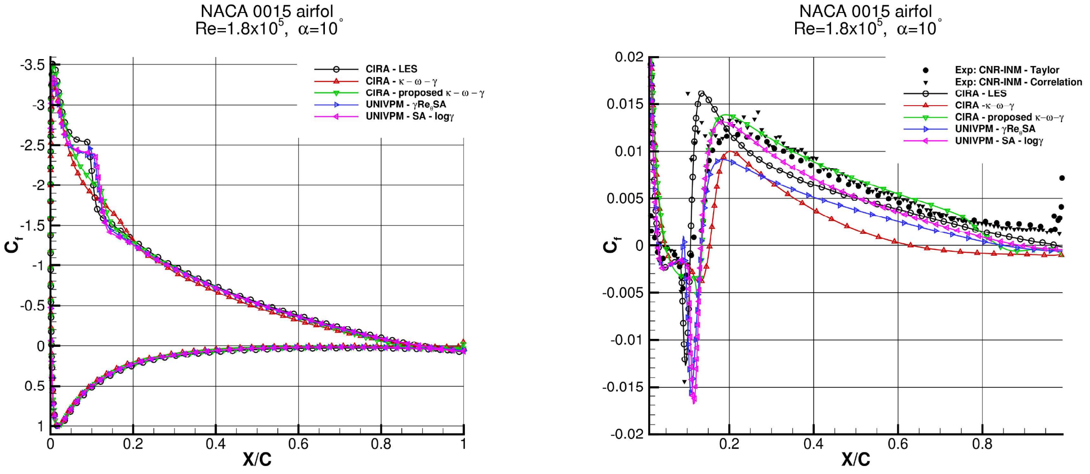

(a) Pressure coefficient

(b) Skin friction coefficient

Figure 24: Pressure and friction coefficients over the NACA 0015 airfoil at $\mathbf{Re}_\infty = \mathbf{1.8} \times \mathbf{10^5}$ and $\boldsymbol{\alpha} = \mathbf{10}^\circ$.

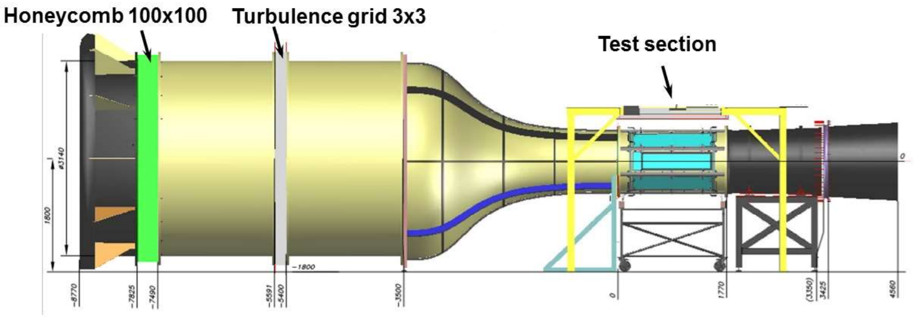

Figure 25: S2L wind-tunnel at ONERA.

numerical simulations. Solid curves labelled *CFD* states for transitional simulations using elsA, $k-\omega$ Wilcox2006-klim model with LSTT activation using automatic computation of transition onset by means of AHD-Gleyzes transition criteria, as presented in §3.4. Curves labelled *XFoil* states for computations using XFoil code from Mark Drela, with automatic transition computation. Several values of N_{cr} were used in order to investigate the influence of the external turbulence level on the position of the transition onset, which in turns impacts the bubble's size and position, possibly including the overall pressure distribution [15]. As shown in Fig. 28, no numerical method was able to accurately predict the entire pressure distribution around the tested airfoil. All numerical methods produced similar pressure distributions outside of the bubble region. Simulations using moderately low turbulence levels ($N_{cr} \in\approx (6, 9)$) exhibit quite similar bubble's size and position, but they are quite far from experimental results. In an attempt to find the N_{cr} value that would produce the best match with respect to experimental measurements, simulations with increasing values of N_{cr} were conducted. However, it was found that CFD computations were unstable and did not converge for $N_{cr} > 9$. XFoil simulations were robust enough to approximately match the

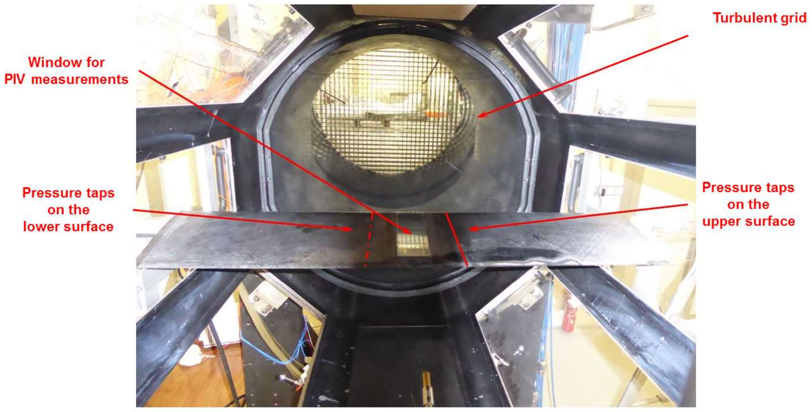

Figure 26: S2L wind-tunnel test section including NACA0012 wing.

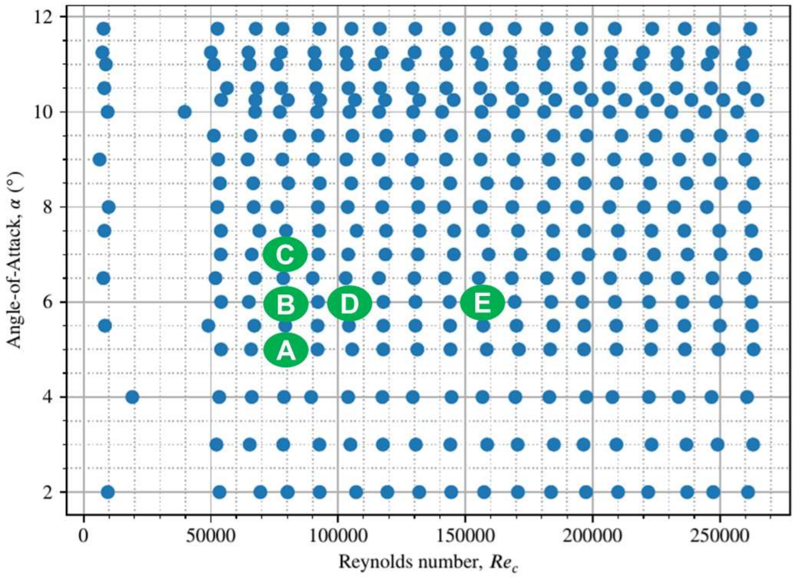

Figure 27: All tests conducted in S2L wind tunnel using NACA0012 airfoil. Markers from A to E designate the subset of cases that were chosen for comparison purposes with respect to CFD simulations.

transition onset location ($x/c \approx 0.47$), but this required an nonphysically high value of $N_{cr} = 16$, which corresponds to an external turbulence value of $T_u \approx 0.0038\%$, following Mack's empirical formula. Although the turbulence level inside of the wind-tunnel test section could not be precisely established, it is assumed that it is unlikely to be lower than 0.1%, which corresponds to $N_{cr} \approx 8$, which is significantly lower than 16. Therefore, the mismatch between experiment and simulations cannot be explained by an inappropriate choice on the value of N_{cr}.

Fig. 29 shows the the time-averaged field of velocity components and the root mean squared

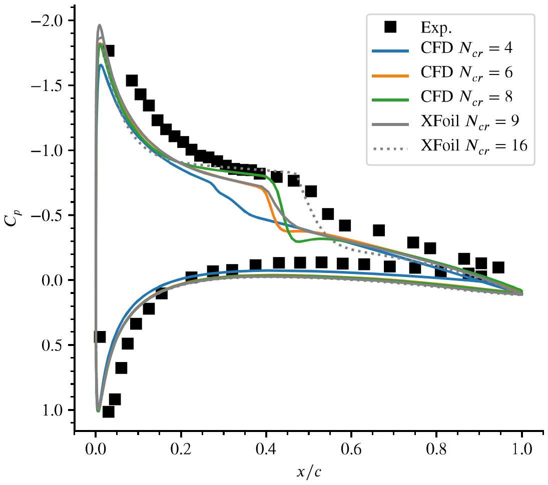

Figure 28: Pressure distributions of Case A with $\alpha = 5°$ and $Re_c = 79610$.

fields of the velocity perturbations. The presence of the bubble, including the transition region, can be observed thanks to the significant levels of $\sqrt{u'u'}$ and $\sqrt{v'v'}$ in the region $0\,\mathrm{mm} < x < 50\,\mathrm{mm}$. However, the spurious noise encountered in this measurements and the coarse resolution of the velocity measurements avoids accurate post-processing of velocity profiles inside the boundary-layer, preventing from extracting relevant boundary-layer quantities such as θ or H.

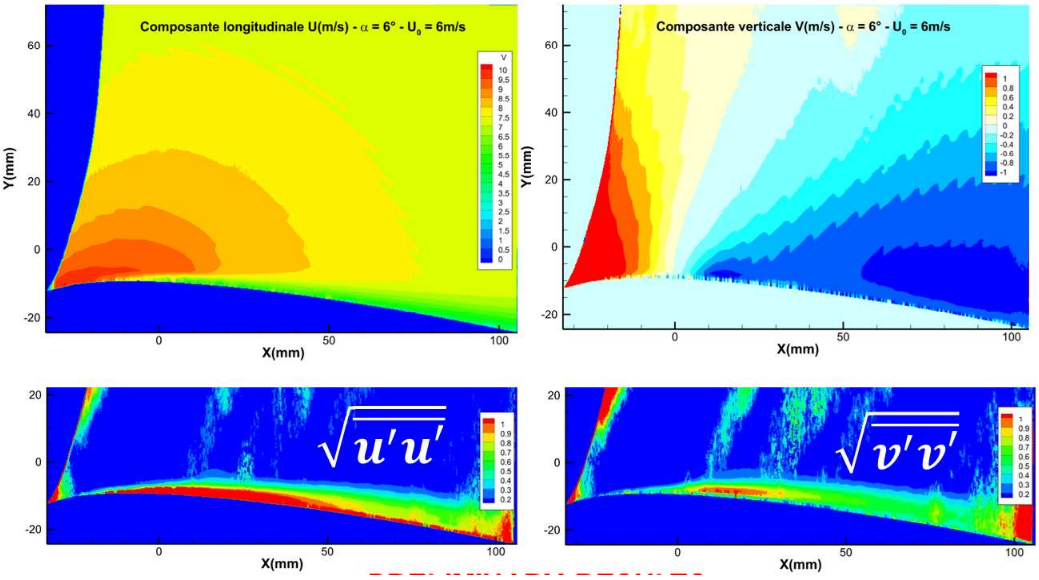

Figure 29: PIV measurements of velocity fields and second-order statistics components of velocity perturbations.

Fig. 30 shows the distributions of boundary-layer momentum thickness and shape factor only for numerical simulations. In line with published work [15] we can observe that decreasing values of turbulence levels (increasing values of N_{cr}) provoke higher values of H, which correlates well with the longer size of the bubble. Similarly, the transition region becomes larger, which can be observed thanks to the sudden increase of θ, which becomes steeper and also it is slightly displaced downstream. It can be observed that $N_{cr} = 4$ simulation essentially exhibits a fully attached boundary-layer (overall value of $H < 3.6$), due to the relatively high value of turbulence level.

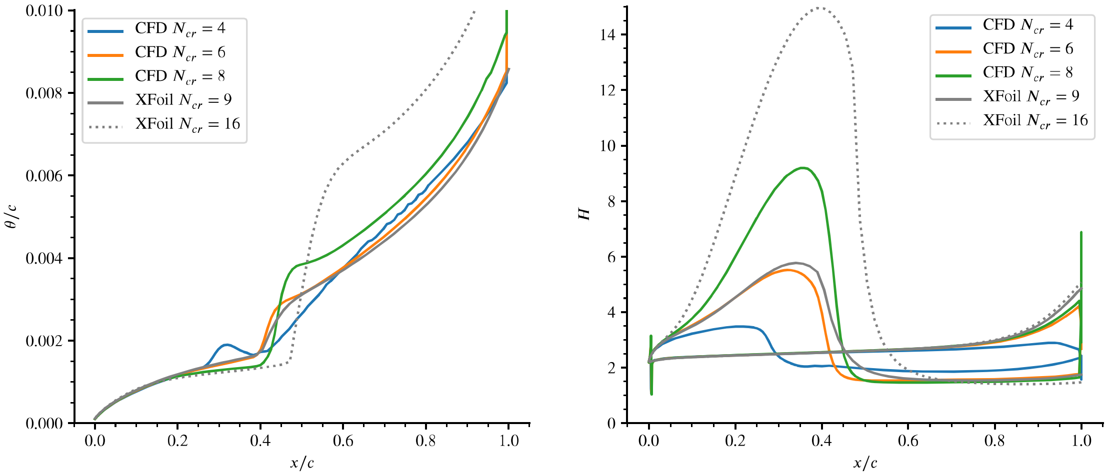

Figure 30: Momentum thickness distribution on suction side (left) and shape factor distribution on both sides (right) of Case A with $\alpha = 5°$ and $Re_c = 79610$.

Numerical predictions were conducted in exactly the same manner for cases Ⓑ to Ⓔ, exhibiting essentially the same behavior as case Ⓐ. This means that no numerical prediction was able to precisely match the bubble size and length and overall C_p distribution. Therefore, a new set of CFD computations was attempted imposing the location of the transition onset, which was taken as the end of the C_p plateau shown in experiments. XFoil computations are presented also as reference, systematically showing that required N_{cr} values to satisfy such downstream location of transition onset are nonphysically high. Results are presented in Fig. 31. It can be observed that cases Ⓐ and Ⓔ show oscillations on the pressure plateau, which may be related to too high values of shape factor H, which provokes an unstable laminar flow. It can be noted that no CFD computation exactly matches the overall pressure distribution measured in the experiment, even imposing the transition onset location. On the other hand, XFoil and CFD computations compare quite well. A possible explanation for this systematic mismatch may be an undesired influence of the walls of the wind tunnel.

4.2 WP 2: Laminar separation bubbles at high Reynolds number

The work package 2 faces with the numerical simulation of laminar separation bubbles at a Reynolds number of order of magnitude 10^6. The following tests cases have been performed by AG59 members.

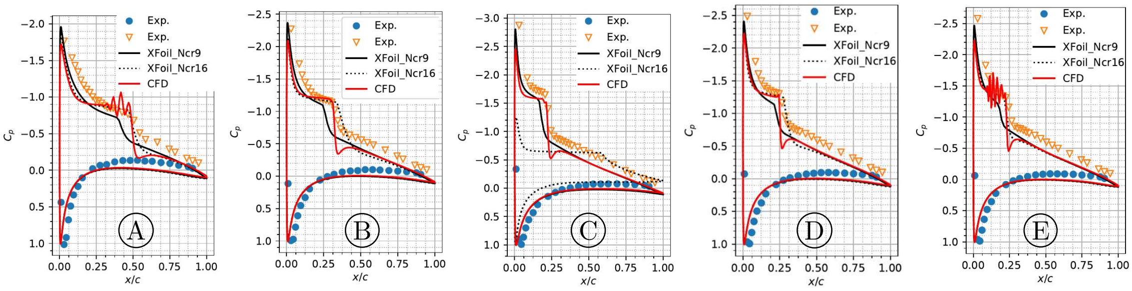

Figure 31: Pressure distributions of cases A to E including CFD simulations with imposed location of transition onset.

4.2.1 Flat plate with adverse pressure gradient

This test case is issued from the work of Laurent et al. [79]. It consists in a flat-plate flow subject to an adverse pressure gradient provoked by a curved slip surface on the top of the wall, as shown in Fig. 32. Arrows indicate direction of flow at domain boundaries. Boundaries ① and ② are inlet farfield conditions, and ⓪ is oultet farfield condition. Dashed lines represent slip walls, hashed contours represent soild walls (no-slip), dash-and-dot lines represent symmetry condition, and double solid lines correspond to farfield conditions.

Reference state for ① is $\rho_1 = 1.216$ kg·m^{-3}, $u_1 = 47.57$ m·s^{-1} and $P = 101500$ Pa. Reference state for ② and ⓪ is $\rho_2 = 1.1318$ kg·m^{-3}, $u_2 = 136.11$ m·s^{-1}. These particular conditions and geometry were chosen [79] to reproduce the laminar separation bubble present on an airfoil OA209 at $\alpha = 15°$, near stall conditions, as shown in Fig. 33.

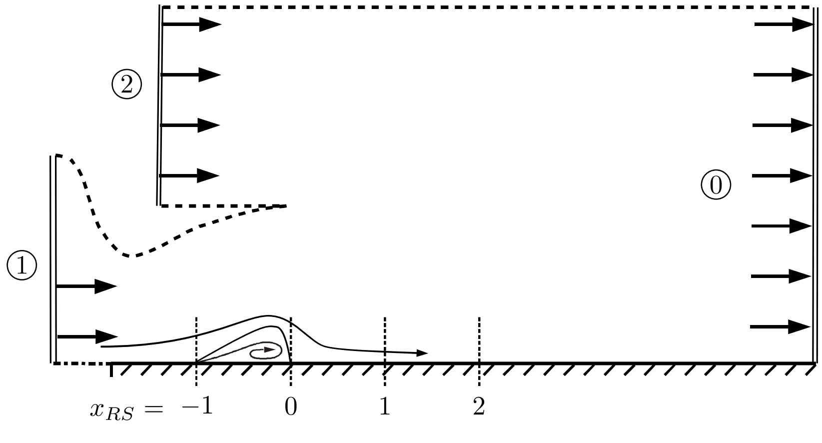

Figure 32: Scheme of the configuration of the reference flowfield (DNS of Laurent et al. [79]), with exagerated scaling.

As reference, in Fig. 34 are shown several relevant boundary-layer quantities around the laminar separation bubble obtained through post-processing of the time-averaged flowfield of the DNS.

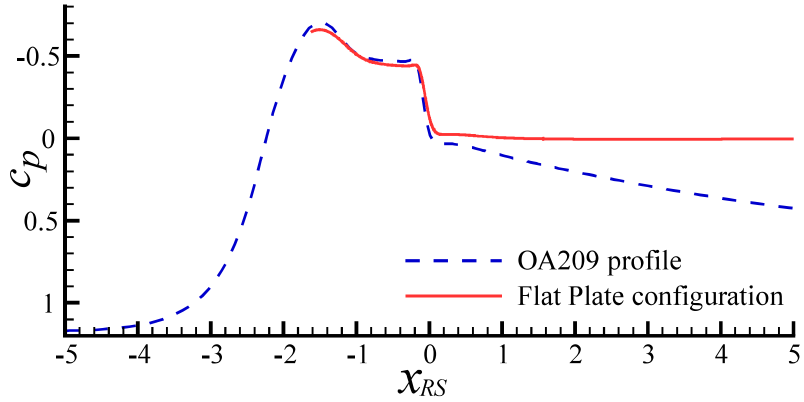

Figure 33: Pressure coefficient C_p distribution around an helicopter blade airfoil OA209 at $\alpha = 15°$ of angle of attack, $Re_c = 1.8 \times 10^6$ and $M_\infty = 0.16$ issued from a RANS/LES hybrid computation [80, 81, 82] (dashed line) and pressure distribution obtained in the flat-plat case constructed by Laurent et al. [79] (solid line). Source: Laurent et al. [79].

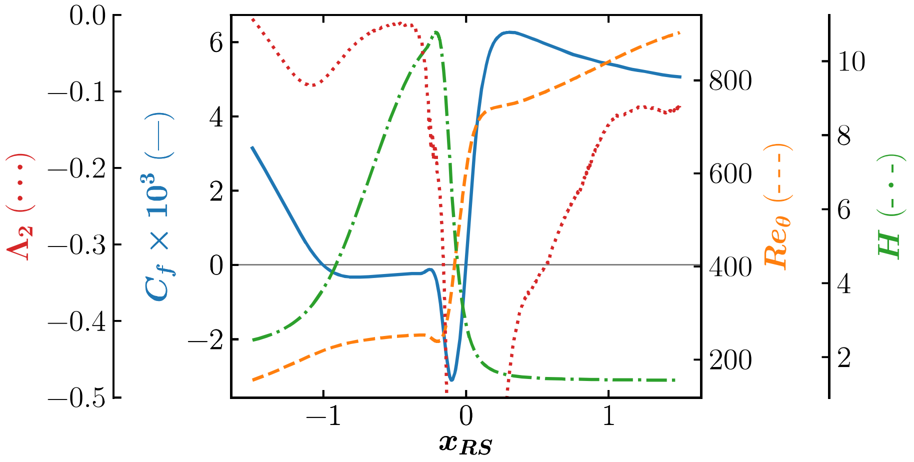

Figure 34: Relevant boundary-layer quantities issued from DNS of Laurent et al. [79].

Calibration of LSTT

In this paragraph we show the calibration of LSTT coefficients using turbulence model $k - \omega$ of Wilcox 2006 [37], following the approach presented in [35]. All details, including calibration using other turbulence models can be found in [83]. In Fig. 35 we can observe an excellent match of the calibrated LSTT model. Without LSTT activation, the turbulence model tends to overestimate the bubble length and separated regions and underestimate the values of Re_θ. In Fig. 36 we can observe also a very good matching of the calibrated LSTT model. Specifically, turbulent regions exhibit better match of the log-law region when using calibrated LSTT activation.

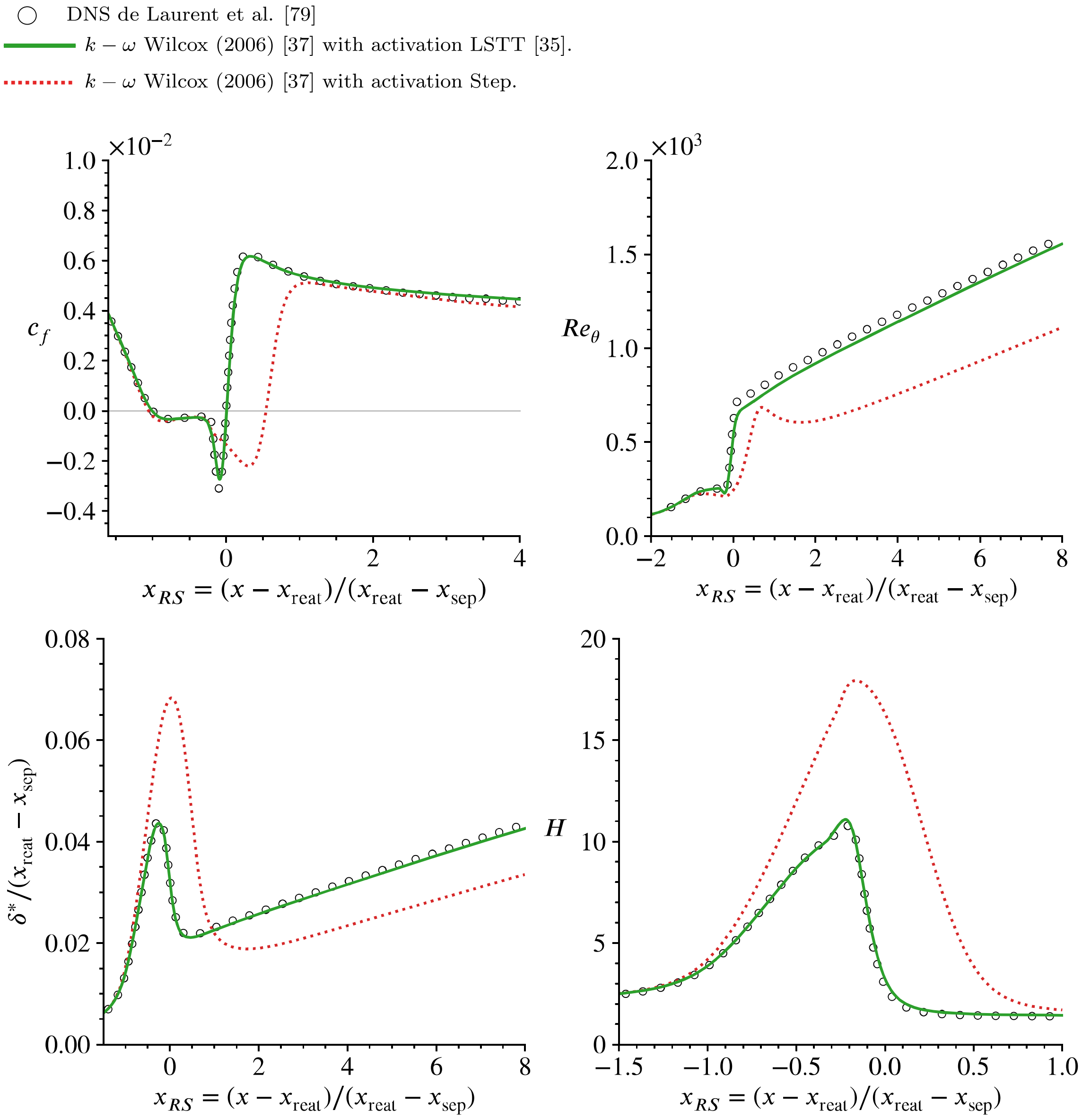

Figure 35: Boundary layer quantities of the calibration of Wilcox 2006 LSTT model with imposed transition onset at $x_{RS} = -0.27$. Comparison of step-like (off/on) in red dashed line and calibration result using LSTT [35], compared to the DNS of Laurent et al. [79].

CIRA Analyses

CIRA performed RANS simulations using the one-equation transition model on the whole domain. The results are compared with the DNS data and the simulations by Laurent and the suite Cassiopee and proved satisfactory. The pressure field in the nozzle region is shown in fig. 37, and a qualitative match can be observed. The pressure contour is highlighted in the bubble region in

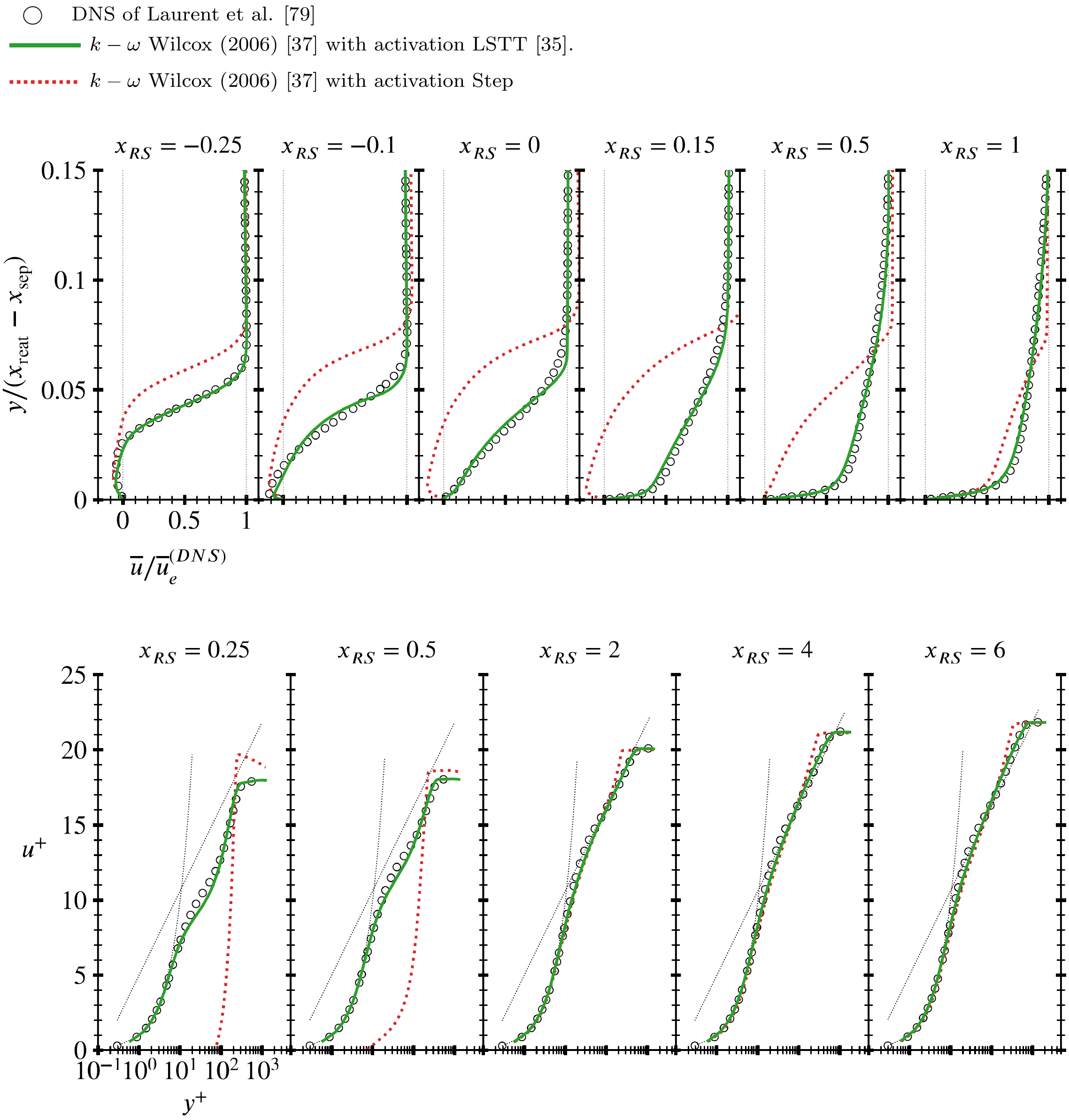

Figure 36: Velocity profiles of RANS predictions using model [37] with imposed transition at $x_{RS} = -0.27$ using Step-like activation (dashed) and using LSTT (solid) [35], compared to DNS of Laurent et al. [79]. Densely dotted curves represent theoretical boundary layer solutions $u^+ = y^+$ and $u^+ = \frac{1}{\kappa}\ln y^+ + C^+$, with $\kappa = 0.41$ and $C^+ = 5$.

fig. 38. The bubble is predicted with a discrete accuracy, as the separation point is coincident with the DNS data, but the compression downstream the reattachment point is smoother, delaying the reattachment of the bubble and increasing the bubble length, as a consequence. Table 7 reports the

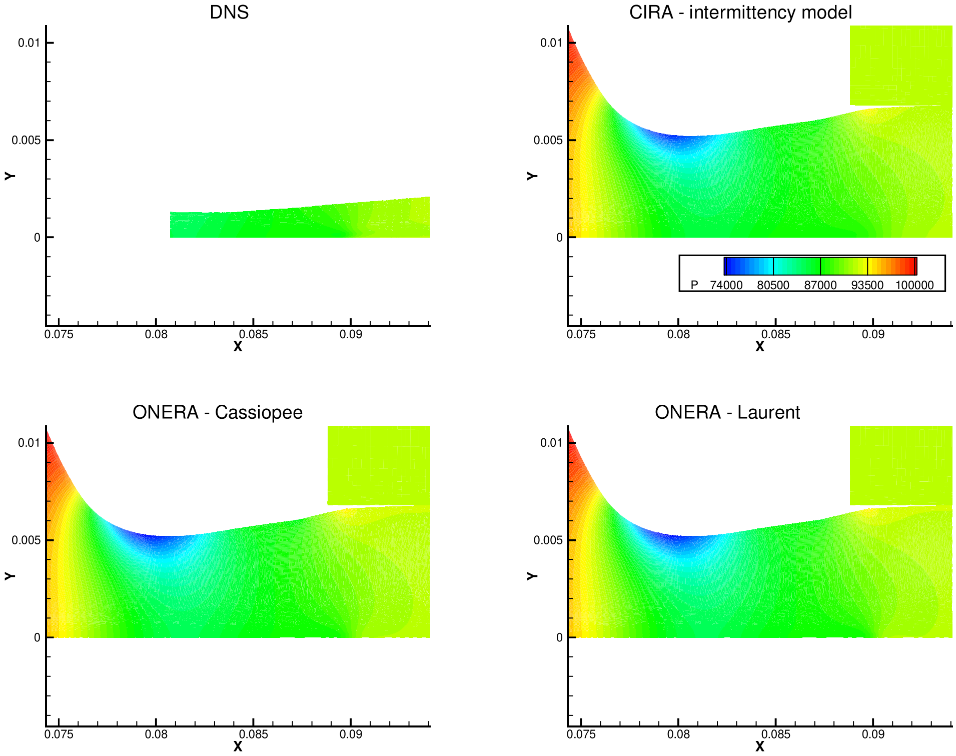

Figure 37: Pressure flow field contour: nozzle region

values for the separation and reattachment point returned by DNS and UZEN. The skin friction is shown in fig. 39. The variable $x_{RS}\frac{x-x^S}{x^R-x^S}$ is computed on the DNS separation and reattachment values. The development of the skin friction in the separated region is well modelled, even tough the reattachment point is computed downstream. The skin friction in the laminar region presents a different slope, but it is attributable to the adopted non-dimensional approach. Indeed, UZEN uses the free-stream reference velocity U_∞, while in the DNS and ONERA computations, the skin friction is non-dimensional with reference to the local velocity U_e.

	x^S	x^R
DNS	0.084479	0.0902718
UZEN	0.084335	0.091240

Table 7: Separation and reattachment point for the APGFP case

The momentum in the stream-wise direction and the pressure profiles are compared at the separation location and shown in fig. 40. As the separation point is computed at the same location for all the simulations, the velocity profiles coincide. The pressure profiles are coherent, but an offset is present. The same comparison is carried out at the reattachment point and shown in fig. 41. In this case, the profiles for UZEN solutions are extracted at the local reattachment point, otherwise

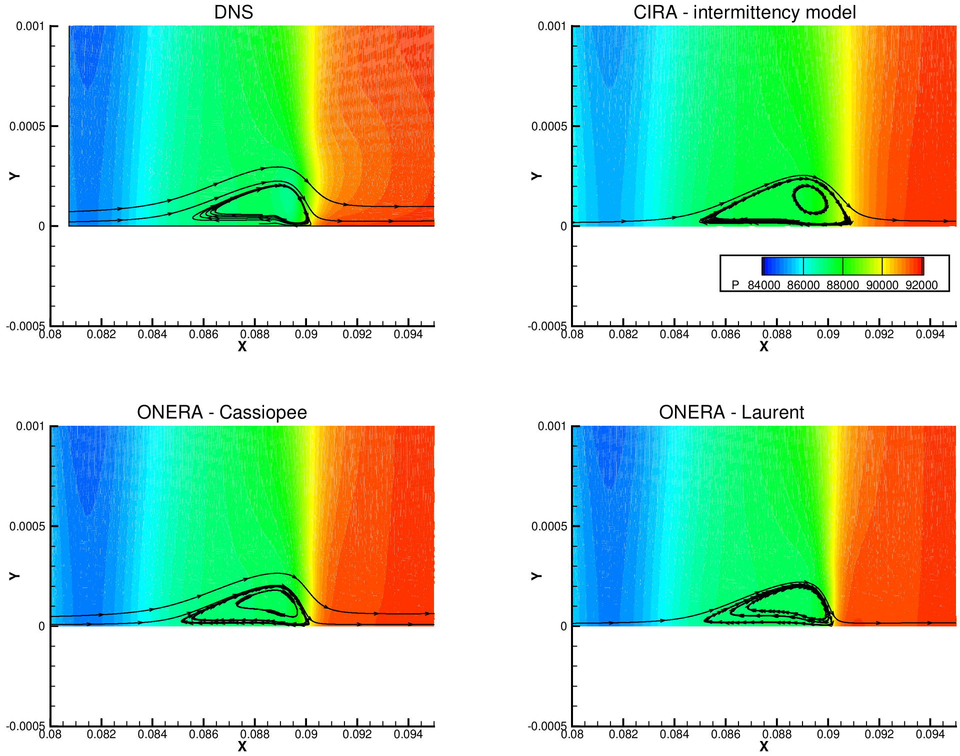

Figure 38: Pressure flow field contour: bubble region (axes not in scale)

they would be in the reverse flow region. The profiles do not compare as well as at the separation location, in particular the pressure profile from DNS is not returned.

4.2.2 S809 airfoil

The optional test case TCO2 deals with the simulation of the flow-field around the S809 airfoil in fig. 42. The airfoil is a 21-percent-thick, laminar-flow airfoil designed for horizontal-axis wind-turbine applications. The airfoil presents two laminar separation bubbles, on both lower and upper side, for Reynolds numbers ranging in $Re = [1.0 \div 3.0] \times 10^6$. Details on the geometry and experimental data are available in [84]. The CFD analyses focused on the $Re = 2.0 \times 10^6$ case.

The adopted transition models are listed in table 8. The simulations were performed on the common grid, a PLOT3D structured type, conveniently transformed by each partner.

	CIRA	UNIVPM	UNISTRA
GRID		Common structured-type grid	
No of cells		$\approx 3.0 \times 10^5$	
Turbulent and transition model	$\kappa - \omega$ SST $+\gamma$	SA$+\gamma$	SA+0-eq. BCM or γ or $\gamma - Re_\theta$ $\kappa - \omega$ SST $+\gamma$ or $\gamma - Re_\theta$

Table 8: BFS settings for turbulent and transition models

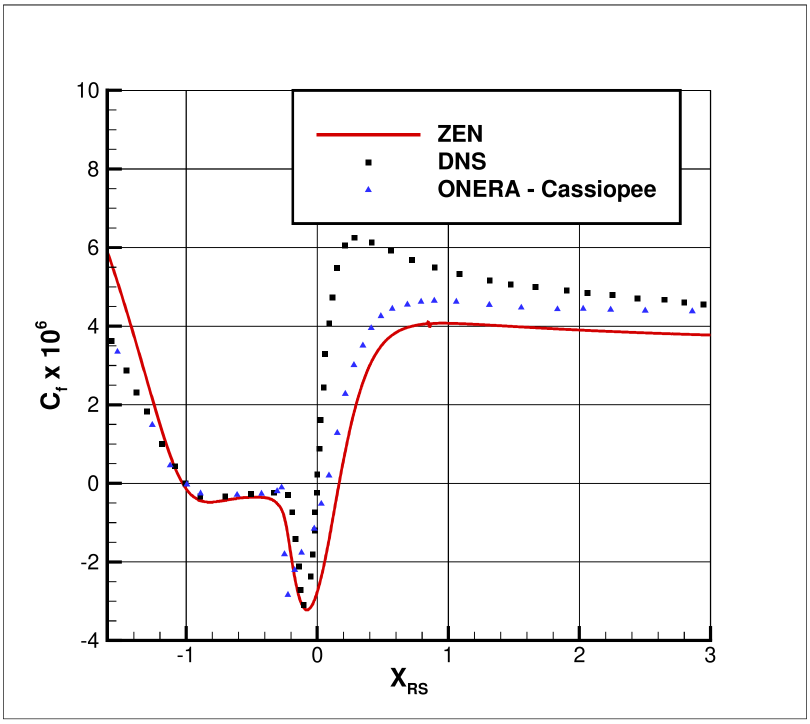

Figure 39: Skin friction coefficient for APGFP case

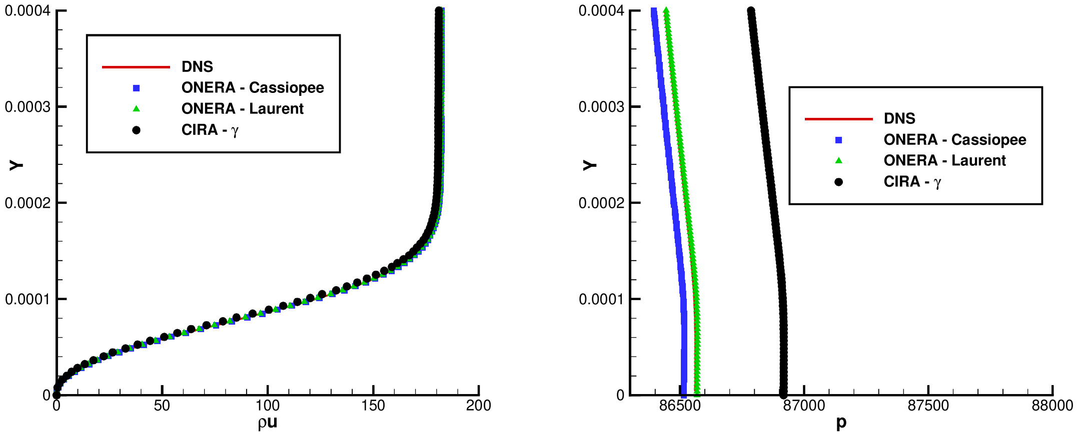

Figure 40: X-Momentum (left) and pressure profile (right) at separation point.

For the comparison, the data of Univ. of Strasbourg refer to the $\kappa - \omega$ SST $+\gamma$ model.

Aerodynamic coefficients are compared in fig. 43 with respect to the experimental data. Data computed by CIRA and UNISTRA with the $\kappa - \omega$ SST model are in good agreement with the

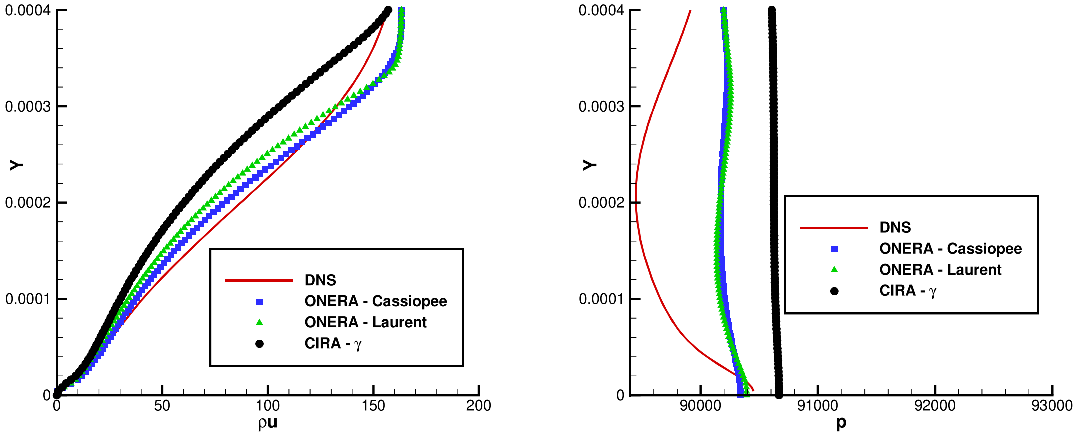

Figure 41: X-Momentum (left) and pressure profile (right) at reattachment point.

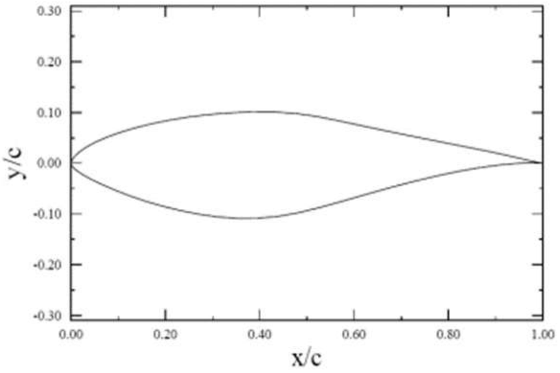

Figure 42: S809 airfoil

experimental data up to the drag increase observed in the experiments at $C_l = 0.8$, while the drag rise is numerically predicted at $C_l = 1.0$ for CIRA and UNISTRA. The results obtained with the Spalart-Allmaras model by UNISTRA are in good agreement at low angles of attack, but they present a “smooth” increase in the drag coefficient that is not returned by the experiments. The results by UNIVPM present a similar “smooth” increase, but with higher drag coefficients. In any case, the improvement with reference to a fully turbulent simulation is evident.

Transition location is compared in fig. 44 for CIRA and UNIVPM computations. A good agreement is achieved for all angles of attack, except in the range $\alpha = [5° \div 9°]$ where the sudden upstream shift is observed on the upper side of the airfoil. CIRA predicts a steep shift at a higher angle of attack ($\alpha = 8°$), while UNIVPM follows the experimental data closer.

Pressure coefficient distribution at three different angles of attack is compared with the experimental data and they are shown in figs. 45 to 47. The general trend among the numerical solutions is a good match on the lower side with a different location of the separation bubble, while some

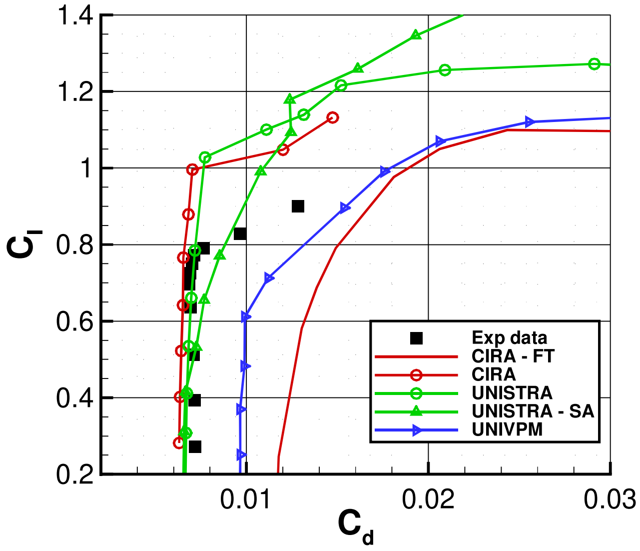

Figure 43: S809 polar curve: γ transition model

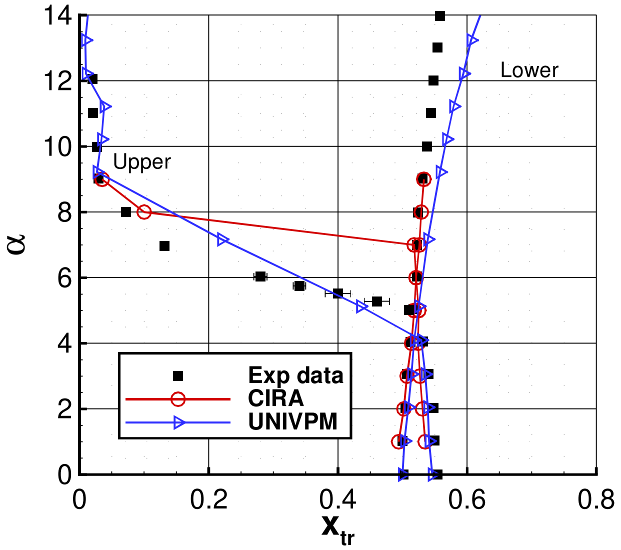

Figure 44: S809 transition location

differences are observed on the expansion region on the upper side. In details, at $\alpha = 1°$ (see fig. 45) the comparison with the experimental data is satisfactory and presents negligible differences in the region of the laminar bubbles. At $\alpha = 5°$ (see fig. 46), the numerical solutions predict a lower c_p on the pressure side of the airfoil with reference to the experimental data, up to the bubble region which is located approximately at $x/c \approx 0.5$. The successive pressure recovery follows the experimental data. On the upper side, different expansion peaks are computed, but the differences are inline with the results observed at $\alpha = 1°$. The experimental values are well matched, except the plateau from $x/c \approx 0.85$. At $\alpha = 9°$ (see fig. 47) the experimental data are well captured, but for this angle, the solution by UNISTRA presents oscillations downstream of the expansion peak.

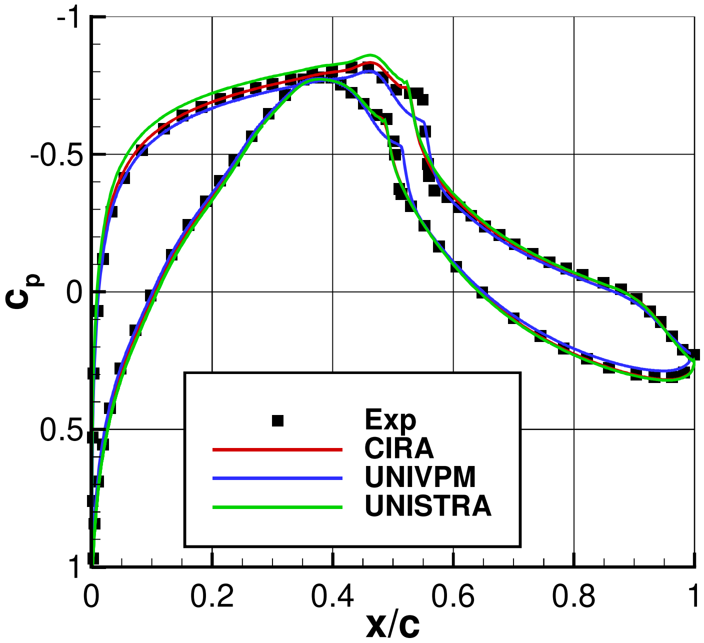

Figure 45: S809 pressure coefficient at $\alpha = 1°$

4.3 WP 3: Transonic flows at low Reynolds numbers

The interest for the compressible aerodynamics of low-Reynolds number flow has recently grown for the possible use of aircrafts for exploring the Martian surface. NASA and JAXA agencies are considering the airplanes as a feasible mean for exploring the Mars surface. In fact airplanes avoiding the morphology of the surface should obtain information wider and more detailed with respect to the ground rovers used in the past missions to Mars.

The design criteria used for the conventional airplanes can not be applied to the design of Mars airplanes because the atmospheric conditions on Mars are quite different from the ones on the Earth. The challenge of this new technological solution lies entirely in the specific environmental conditions these aircraft will be required to operate in. Mars atmosphere is 95% constituted by CO_2 and the force of gravity is about 1/3 than the Earth's. The reduced atmospheric pressure and density, together with the low temperatures, produce flight conditions characterised by very low Reynolds numbers, about 2% of those on the Earth, in combination with high Mach numbers, 1.5 times higher

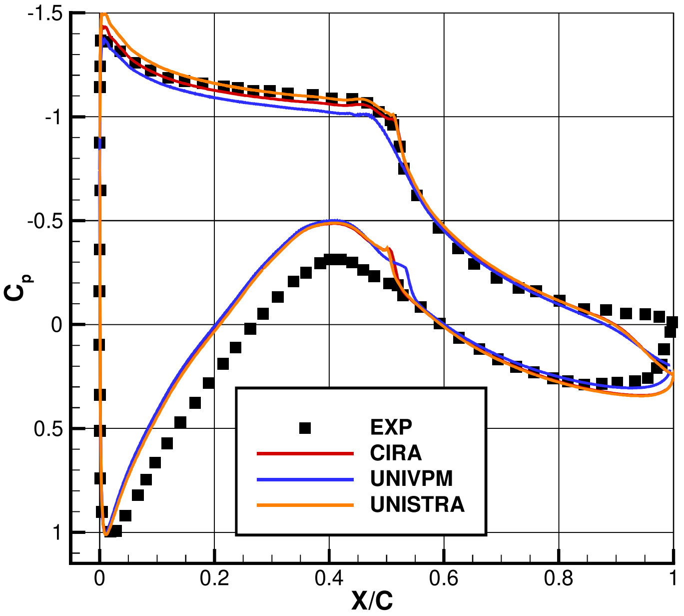

Figure 46: S809 pressure coefficient at $\alpha = 5°$

than the terrestrial ones. Mars airplane is expected to perform a flight at low Reynolds number in the range of $10^4 - 10^5$ at relatively high speed to produce enough lift to sustain its weight as well as to ensure a stable flight in gusty atmosphere. The flight Mach number should range between 0.4 and 0.7.

The evaluation of the aerodynamic characteristics of airfoils and wings in such particular conditions, scarcely investigated so far, is becoming increasingly more important for the understanding of the feasibility of such technological solution. Low-Reynolds number flows exhibit an unique behaviour in the compressible regime compared to the commonly studied high-Reynolds-number compressible flow or to low-Reynolds number incompressiblle flows. It is expected that the flow field on a wing flying in Mars atmosphere is quite complicated with a strong interaction between viscous and compressibility effects. For incompressible low-Reynolds number flows, the separation physics is strongly influenced by the viscous effects and allows for the formation of large-scale vortices. Laminar separation bubbles often occur strongly influencing pressure distributions and aerodynamic characteristics. Compressibility effects can play a role in suppressing the onset of shear-layer instability and the resulting formation of wake vortices.

Moreover, it has also to be considered that the availability of experimental data for the compressible low-Reynolds number regime, useful for the assessment of the numerical codes, is quite limited (figure 48).

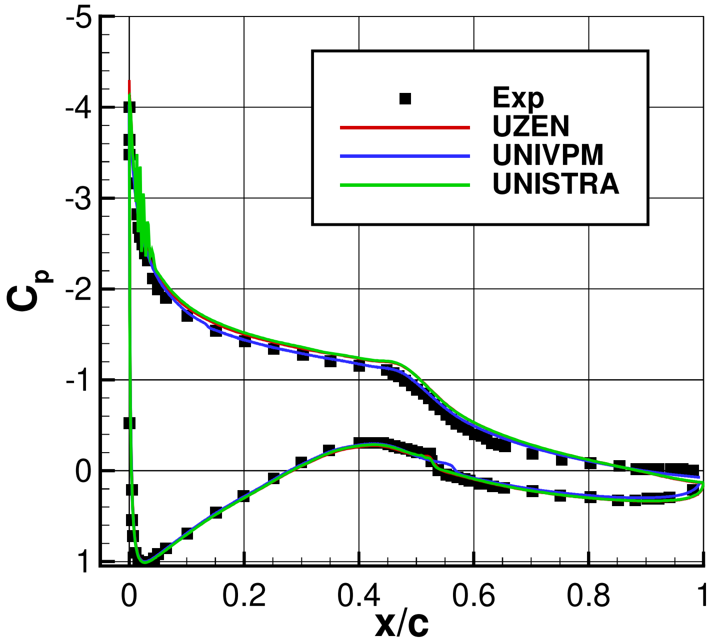

Figure 47: S809 pressure coefficient at $\alpha = 9°$

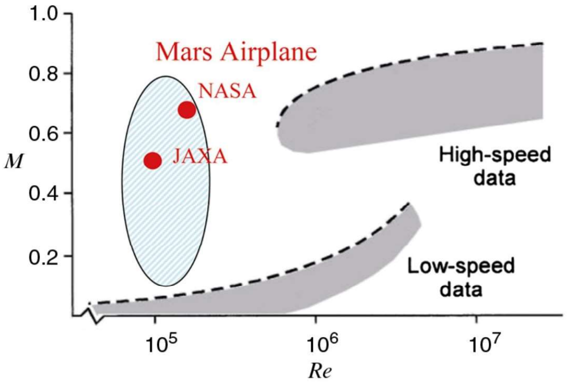

Figure 48: Availabity of experimetal data (from [85])

4.3.1 Triangular airfoil in wind tunnel

The experiment in the low density CO_2 tank wind tunnel of Tohoku University [86, 87] over a triangular airfoil with global forces and local PSP measurements, has been considered for the assessment of the numerical methods.

The Tohoku facility is composed of two chambers and is able to perform experiments with low-density compressible flows (figure 49). The wind tunnel is inside a vacuum chamber driven by an ejector using a high-pressure gas supply. The pressure inside the chamber is regulated by a butterfly valve that release the gas into a second buffer tank. The Mach and Reynolds numbers are regulated by setting the inner pressure and the driving pressure from the ejector [87]. Both air and CO_2 can be used. The specification of the tunnel [86] are reported in the following table. Air has been used in both experiments and numerical simulations to reproduce the flow around the triangular airfoil.

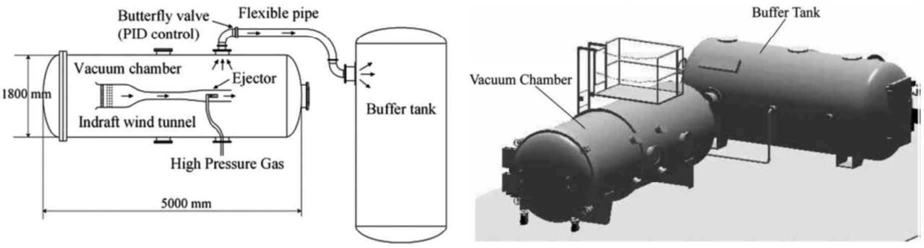

Figure 49: Tohoku wind tunnel

Operation Mode	Air	CO_2
Total pressure	1 to KPa	
Specific heat ratio	1.4	1.3
Mach number (max)	0.74	0.84
Reynolds number (range)	2.6×10^3-1.1×10^5	4.2×10^3-1.3×10^5
Test time	$2 \approx 8s.$	
Test section	100 mm. ×150 mm.	

The numerical simulations have been performed by CIRA and ONERA. CIRA has applied the UZEN and ONERA the elsA code. CIRA has considered both turbulent and laminar conditions, while ONERA has perfomed laminar numerical simulations. Three meshes have been kindly provided by ONERA and represent the airfoil set in the wind tunnel (figure 50) at $\alpha = 5°$, $10°$, and $15°$. The grid has about 15×10^6 cells with 130 cells in the spanwise direction The grids allow for the resolution of the boundary layer on all the tunnel walls.

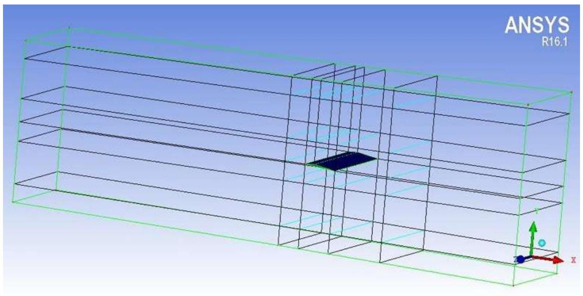

Figure 50: Triangular airfoil in Tohoku wind tunnel. Topology of the grid

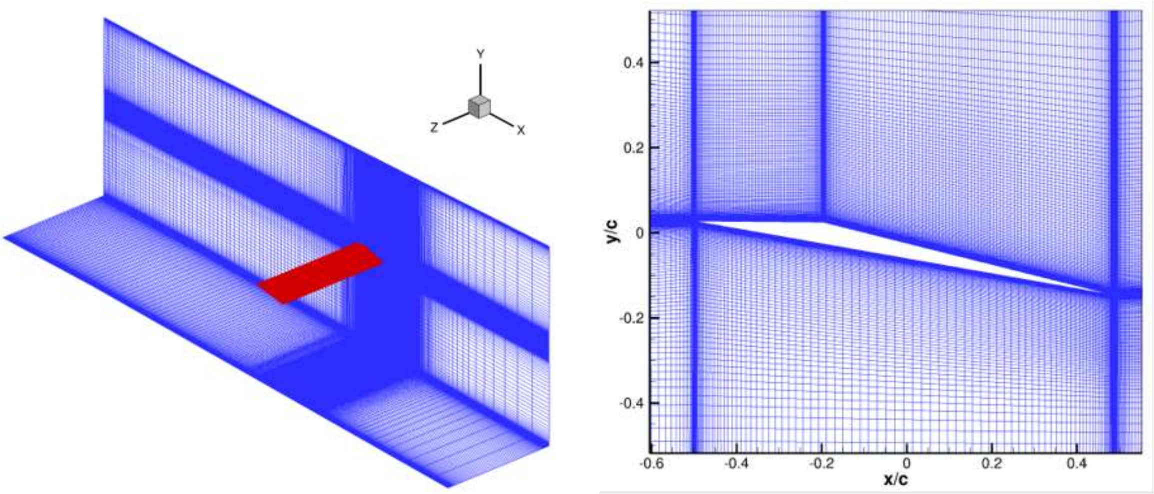

(a) $x - y$ Plane of the grid

(b) Plane around the triangle

Figure 51: Computational grid

Experimental data in terms of aerodynamic and pressure coefficients are available at different Mach and Reynolds numbers [88]. Numerical simulations have been performed at $\alpha = 5°$, $10°$, and $15°$, Mach number 0.15, 0.50, and 0.70, and Reynolds number 3.0×10^3, and 1.0×10^4.

$\alpha = 5°$ The flow field computed by ONERA at Mach=0.50 and Reynolds number=3.0×10^3 is shown in figure 52a. A separated zone on the backside of the airfoil is clearly reported. The pressure coefficient at the mid-span section of the airfoil achieved at Mach=0.50, and Reynolds number=3.0×10^3 is compared to the experimental data in figure 52. A laminar flow and a turbulent flow by four turbulence models, the $\kappa - \omega$ TNT, SST, SSTLR [2] and SST-γ, have been considered. Laminar solution averaged along the span has been obtained by ONERA.

Experimental C_p are available at $\alpha = 4°$ and $6°$. The agreement is not very good with an over-prediction on the rear region of the upper surface. The C_p returned by the $\kappa - \omega - \gamma$ model is very similar to the laminar solution, as expected considering the Reynolds number. The $\kappa - \omega$ SST and SSTLR provide the same result different to the $\kappa - \omega$ TNT. This could be explained by considering that the boundary layer of the WT walls has been taken into account only by the $\kappa - \omega$ TNT model.

The effect of the Mach number is shown in the figure 53 at Reynolds numbers 3.0×10^3 and figure 54 at Reynolds 1.0×10^4. The effect is more remarkable on the upper surface and is the same at both the Reynolds numbers. The flow expands more in the front part and less in the rear part of the airfoil as the Mach number decreases. All the turbulence models return the same effect in the same way as when the condition of laminar flow is assumed.

The effect of the Reynolds number is shown in the figures 55 at the three Mach numbers investigated. The Reynolds number has influence on the pressure levels on the upper surface of the airfoil. The flow tends to have a greater expansion peak as the Reynolds number increases. This effect is returned by all the models and more clearly by the $\kappa - \omega$ TNT model. It is evident in all the plots that the compression downstream the leading-edge expansion becomes stronger at the highest Reynolds number. A stronger compression occurs in the rear zone as the Reynolds number

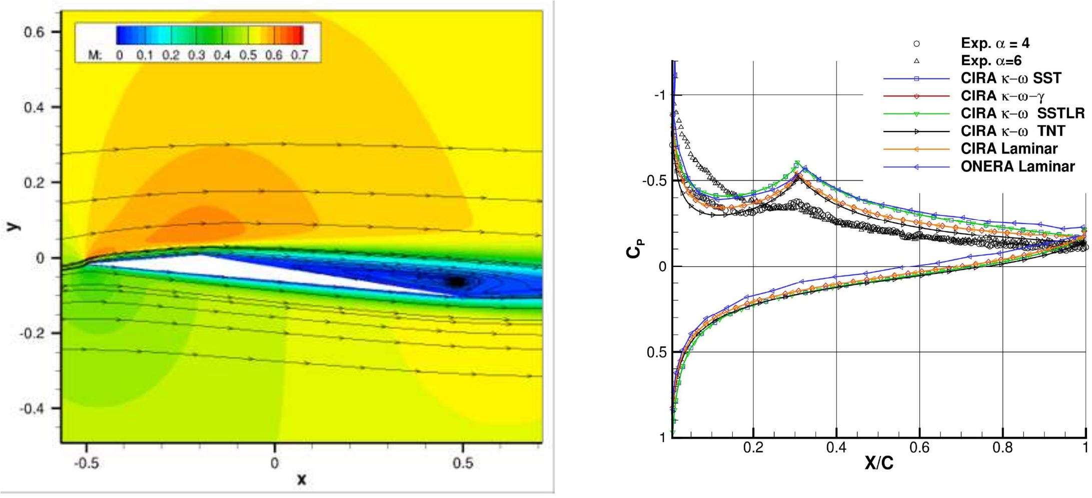

(a) Flow field (b) Pressure coefficient

Figure 52: Flow field and pressure coefficient on the triangular airfoil. Mach=0.50, Reynolds number=3.0×10^3, $\alpha = 5°$

increases.

$\alpha = 10°$ The pressure coefficient at Mach=0.50, and Reynolds number=3.0×10^3 is presented in figure 56. The comparison with the experimental data is not good. The flow is separated in the experiments on a large portion of the airfoil, while the $\kappa - \omega$ TNT and SST provide an attached flow at the mid-span section of the model. This is confirmed in figure 57 that shows the pressure distribution and the skin friction lines on the upper surface of the airfoil. The flow is fully attached in the central region of the model while some 3D effects can be noted at the side-ends of the model. This has been confirmed also by visualizing flow structures by the Q criterion as can be seen in figure 58.

The C_P by ONERA has been obtained by averging the flow in the spanwise direction while CIRA results are in the mid-span section. The difference between the averaging process and the mid-span data has been evidenced by ONERA (figure 59).

At this incidence, some turbulence models have shown poor convergence, and time-accurate simulations should have been necessary. However, the $\kappa - \omega$ SST model has provided results with an acceptable level of convergence at all the flow conditions taken into consideration. Therefore, the effect of Mach and Reynolds number has been investigated by this model.

The effect of the Mach number is shown in figure 60 and is similar to the one observed at $\alpha = 5°$. The expansion in the front part and the compression in the rear region increases with the Mach number.

The effect of the Reynolds number is presented in figure 61. The flow tends to expands more as the Reynolds number increases. This is much more evident in the front part, and becomes almost negligible in the rear region of the airfoil.

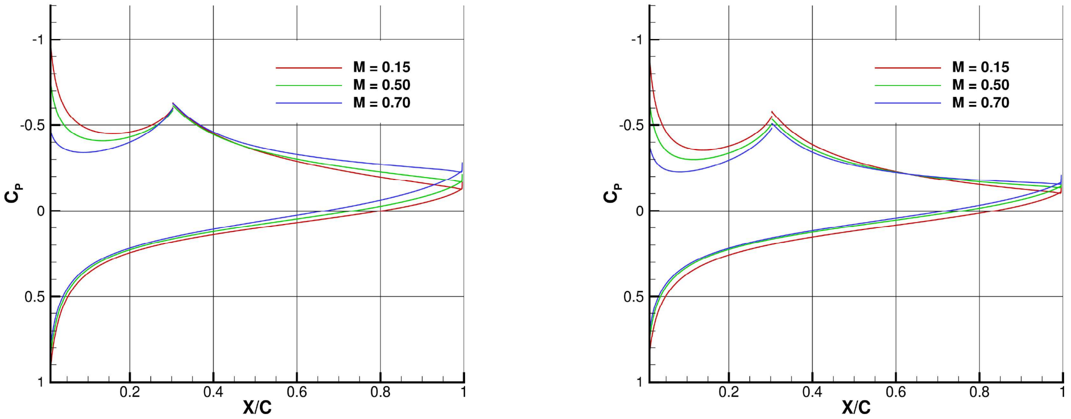

(a) $\kappa - \omega$ SST

(b) $\kappa - \omega$ TNT

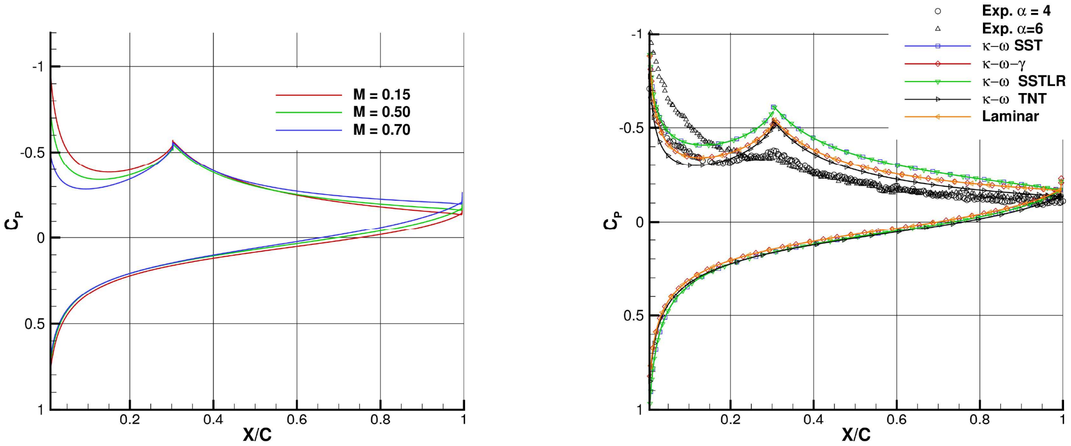

(c) $\kappa - \omega - \gamma$ SST

(d) LAMINAR

Figure 53: Pressure coefficient at $\alpha = 5°$. Effect of Mach number at Reynolds number 3.0×10^3

$\alpha = 15°$ Time-accurate simulations have been needed at this incidence. This has turned out to be necessary at the lowest Mach and Reynolds numbers, while a reasonable convergence has been obtained at the highest Mach numbers and Reynolds of 1.0×10^5 by steady RANS computations.

Time-accurate simulations have been performed by CIRA aaplying the $\kappa - \omega$ TNT model. The flow has shown a predominant frequency as shown in figure 62 that reports the power spectral density of lift and drag coefficients at Mach 0.15 and 0.50 and Reynolds number 3.0×10^3 and 1.0×10^4. The resulting Strouhal number is about 0.680 at Mach 0.15 and Reynolds 3.0×10^3, 0.609 at Mach number 0.50, and Reynolds number 3.0×10^3, and 0.704 at at Mach 0.15 and Reynolds 1.0×10^4.

The flow field provided by the numerical simulations is quite complex. Figure 63 reports the

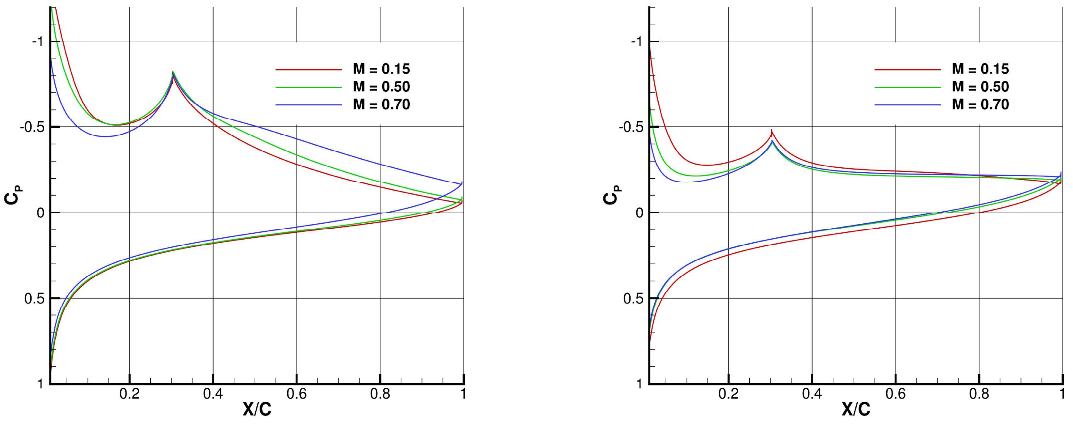

(a) $\kappa - \omega$ SST

(b) $\kappa - \omega$ TNT

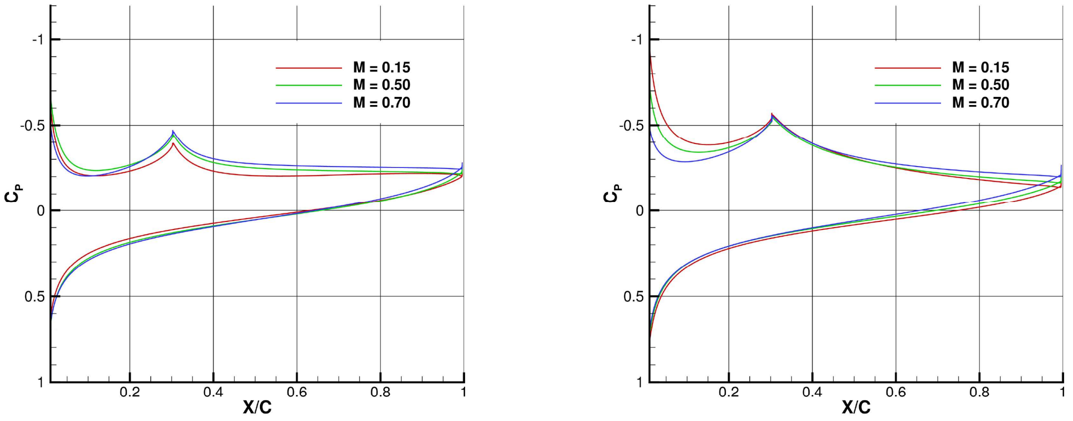

(c) $\kappa - \omega - \gamma$ SST

(d) LAMINAR

Figure 54: Pressure coefficient at $\alpha = 5°$. Effect of Mach number at Reynolds number 1.0×10^4

flow field in terms of surface pressure distribution and skin friction lines as provided by the $\kappa - \omega$ TNT turbulence model. Side-ends effects and separation regions in the central part of the model downstream the vertex of the triangle are visible at all the flow conditions. The trace of a horseshoe-shaped vortex can be discerned at M=0.50 and Re=3.0×10^3. The flow structures forming at the side-ends of the body and developing in the wake can be also appreciated in figure 64 that reports an iso-surface of $Q = \frac{1}{2}\Big(\Omega_{i,j}\Omega_{i,j} - S_{i,j}S_{i,j}\Big)$ coloured by the Mach number. The vortex regions in the central part are visible. It can be also noted as the side-end structures tend to disappear at the highest Reynolds number. //

The time-averaged pressure coefficient achieved by CIRA applying the $\kappa - \omega$ TNT turbulence

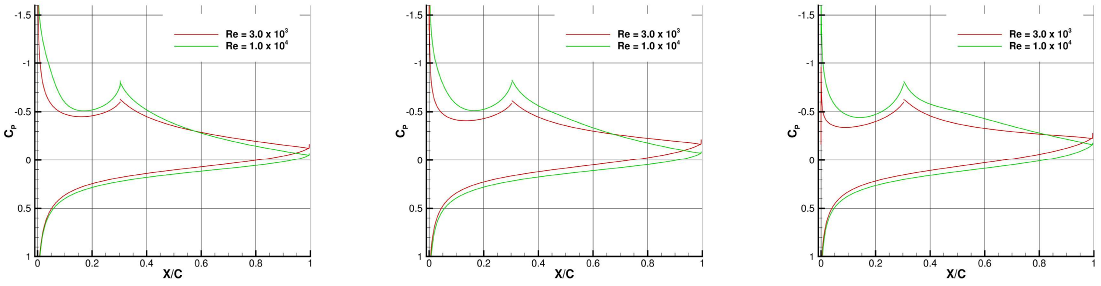

(a) Mach = 0.15, $\kappa - \omega$ SST (b) Mach = 0.50, $\kappa - \omega$ SST (c) Mach = 0.70, $\kappa - \omega$ SST

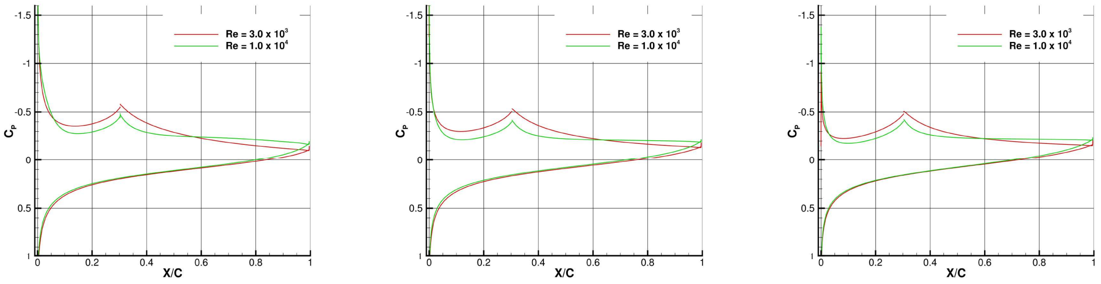

(d) Mach = 0.15, $\kappa - \omega$ TNT (e) Mach = 0.50, $\kappa - \omega$ TNT (f) Mach = 0.70, $\kappa - \omega$ TNT

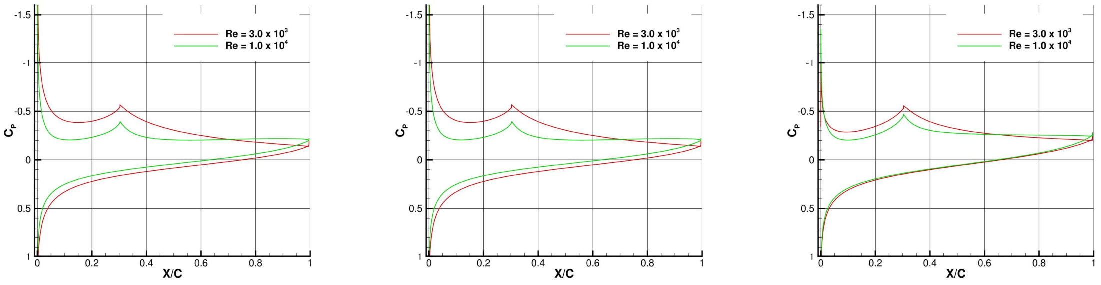

(g) Mach = 0.15, $\kappa - \omega - \gamma$ SST (h) Mach = 0.50, $\kappa - \omega - \gamma$ SST (i) Mach = 0.70, $\kappa - \omega - \gamma$ SST

Figure 55: Pressure coefficient at $\alpha = 5°$. Effect of Reynolds number.

model and by Onera with the laminar assumption is compared to the experimental data in figure 65. A fully separated flow on the upper surface is returned by both experiments and numerical simulations. The level of C_p is overestimated in both turbulent and laminar simulation.

The effect of the Mach number is shown in figure 66. The flow is separated at all the Mach numbers but the levels of pressure on the upper surface become lower as the Mach increases.The effect is more evident between Mach 0.15 and Mach 0.50. At Mach number 0.70, the effect of a vortex seems to be present in the rear region of the airfoil.

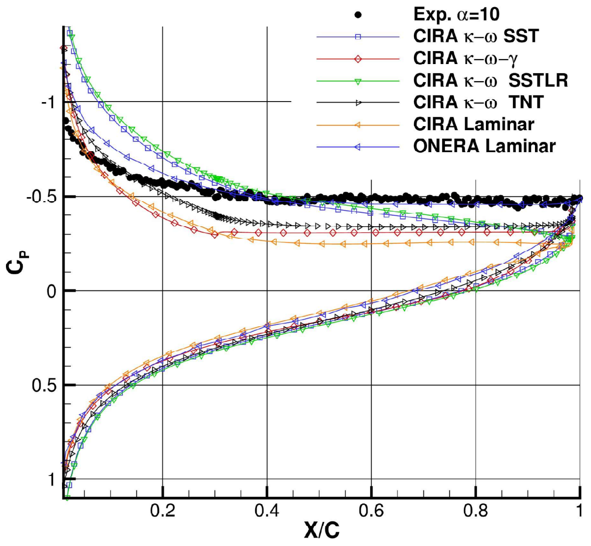

Figure 56: Pressure coefficient at $\alpha = 10°$, Mach=0.50, and Reynolds number $=3.0 \times 10^3$

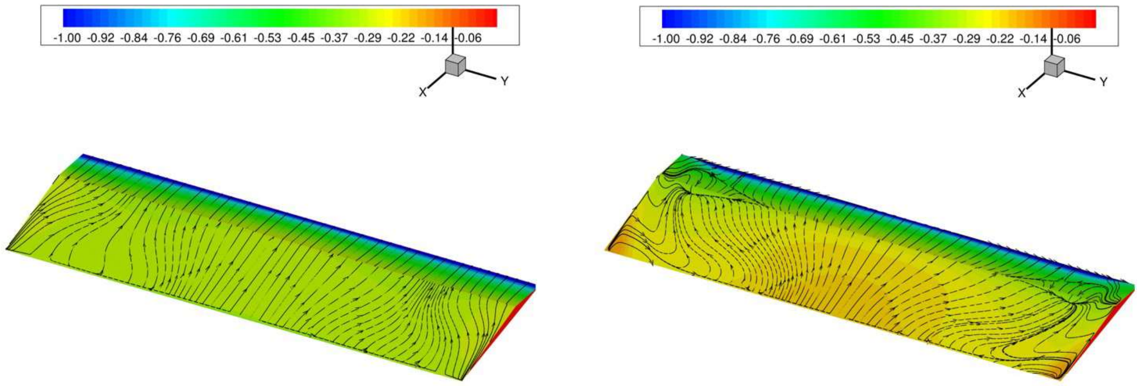

(a) $\kappa - \omega$ SST (b) $\kappa - \omega$ TNT

Figure 57: Pressure coefficient and skin friction lines on the upper surface of the airfoil at Mach 0.50, Reynolds 3.0×10^3 and $\alpha = 10°$.

Aerodynamic Coefficients The lift curves and the drag polars achieved by CIRA are shown in figure 67 and 68 for Reynolds number 3.0×10^3 and 1.0×10^4 respectively. Only the numerical results achieved by simulations with a good level of convergence are reported in the plots.

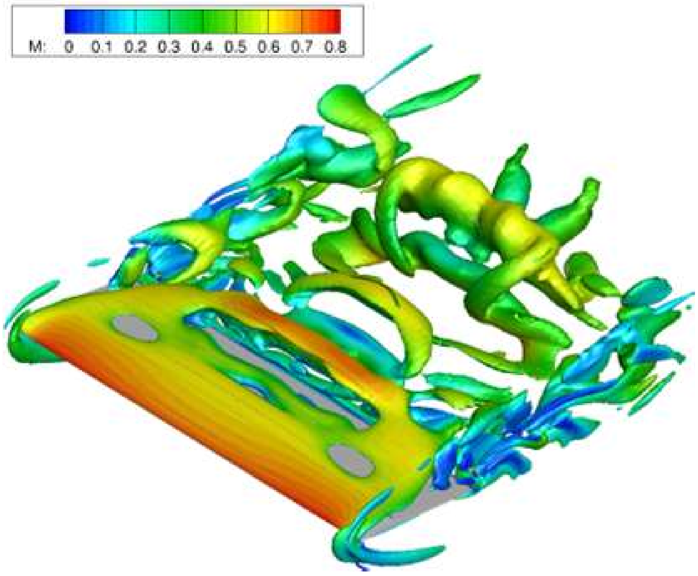

Figure 58: Isosurface of $Q = 1.42$ coloured by Mach number. Mach=0.50 Reynolds number $=3.0 \times 10^3$, and $\alpha = 10°$

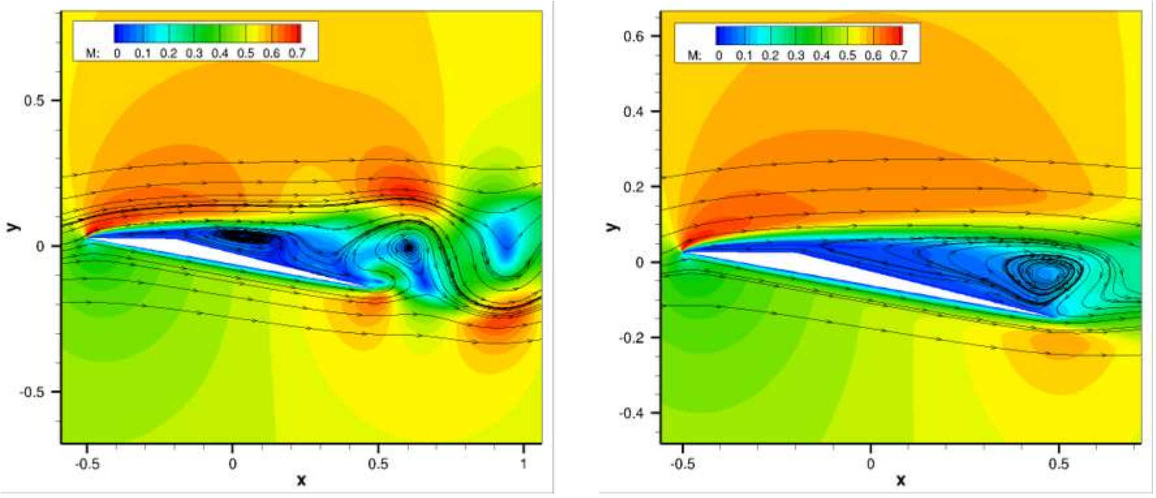

(a) Flow in the mid-span section

(b) Spanwise-averaged flow

Figure 59: Flw in the mid-span section and apnwise-averagedMach 0.50, Reynolds 3.0×10^3 and $\alpha = 10°$.

At Reynolds number 3.0×10^3, all the numerical models have provided lift coefficients in good agreement with the experiments at $\alpha = 5°$ for all the three Mach numbers considered. As the incidence increases, the comparison gets worse as expected. At $\alpha = 10°$, only the lift coefficient

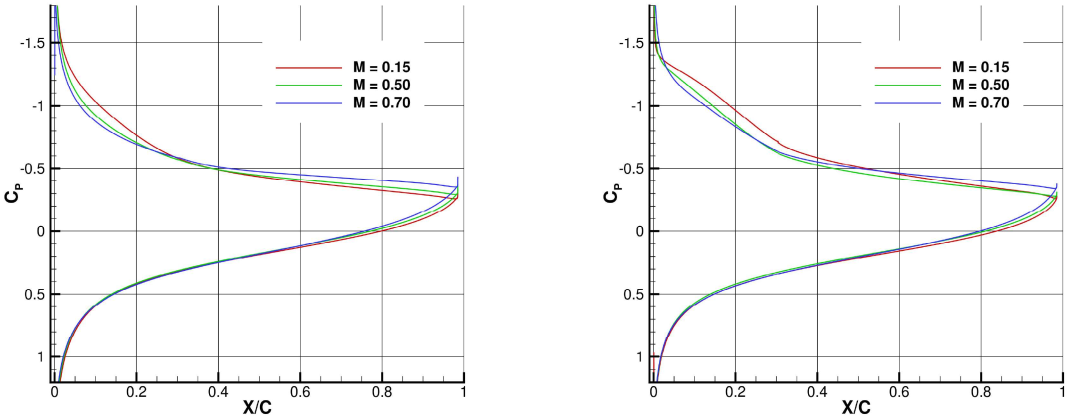

(a) Re = 3.0×10^3

(b) Re = 1.0×10^4

Figure 60: Pressure coefficient at $\alpha = 10°$. Effect of Mach number by the $\kappa - \omega$ SST turbulence model

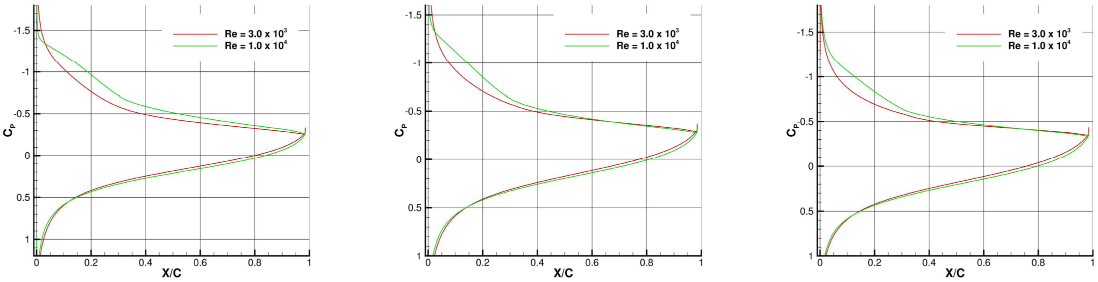

(a) Mach = 0.15

(b) Mach = 0.50

(c) Mach = 0.70

Figure 61: Pressure coefficient at $\alpha = 10°$. Effect of Reynolds number by the $\kappa - \omega$ SST model.

returned by the $\kappa - \omega$ SSTLR is acceptable, while a large discrepancy is obtained at $\alpha = 15°$. The $\kappa - \omega$ SST provides a C_L in very good agreement with the experiments at Mach 0.70 and $\alpha = 15°$.

The analysis of the drag polars is very interesting. The agreement between numerical and experimental data is quite good except for Mach 0.15 at the high values of the lift coefficient. The behaviour and the trend of the polars is well reproduced at all the Mach numbers.

At Reynolds number 1.0×10^4, laminar simulations have not been performed because the hypothesis of laminar flow has been assumed only at Reynolds number 3.0×10^3. The agreement with the experimental data is better than at $Re = 3.0 \times 10^3$. The comparison for the lift coefficient is more than acceptable at all the incidences and Mach numbers with some more discrepancy at Mach 0.70. The non linearity and the behaviour of the C_L curves seems to be captured by the numerical simulations.

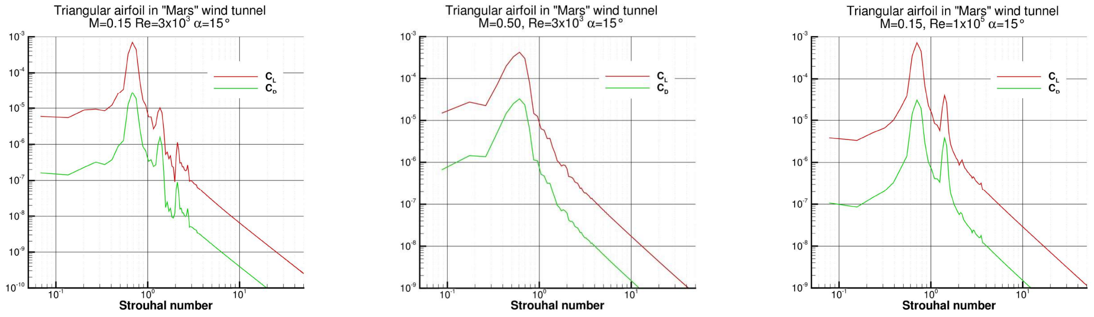

(a) M=0.15, Re=3.0 × 10^3 (b) M=0.50, Re=3.0 × 10^3 (c) M=0.15, Re=1.0 × 10^4

Figure 62: PSD of aerodynamic coefficients at $\alpha = 15°$

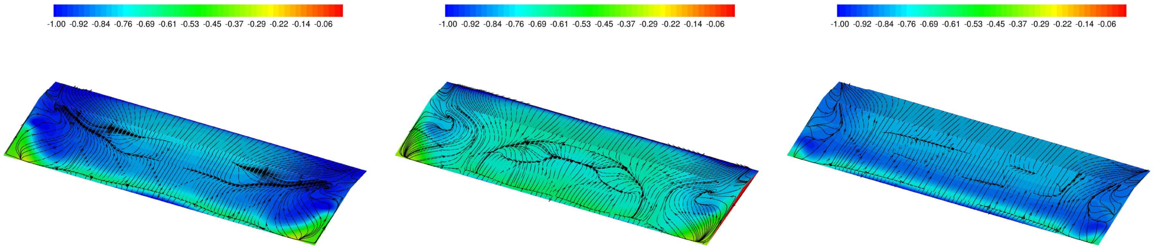

(a) M=0.15, Re=3.0 × 10^3 (b) M=0.50, Re=3.0 × 10^3 (c) M=0.15, Re=1.0 × 10^4

Figure 63: Pressure distribution and skin friction lines at $\alpha = 15°$

A good comparison with the experiments is shown for the drag polars. At $M = 0.15$, the agreement is very good, while some discrepancy can be noted at Mach 0.50 and 0.70 at the high values of C_L and C_D. However, behaviour and trend of the curves are well reproduced at all the Mach numbers.

A comparison between the results achieved by CIRA applying the $\kappa - \omega$ TNT model and by ONERA assuming laminar flow conditions is presented in figure 69. The coefficients returned by two solvers by two different flow modelling are quite similar with a general underprediction of the CIRA data.

Both the numerical simulations show a good comparison with the experimental results at low/medium incidence ($\alpha = 5°, 10°$) where the flow is not fully separated. A large discrepancy is, instead, visible at $\alpha = 15°$.

4.4 WP 4: Instability Analysis of laminar separation bubbles

4.4.1 Objectives and data preprocessing

In section 3.3 the capabilities and limitations of several numerical approaches for linear stability analysis of convectively unstable geometry-induced laminar separation bubbles (LSB) have been

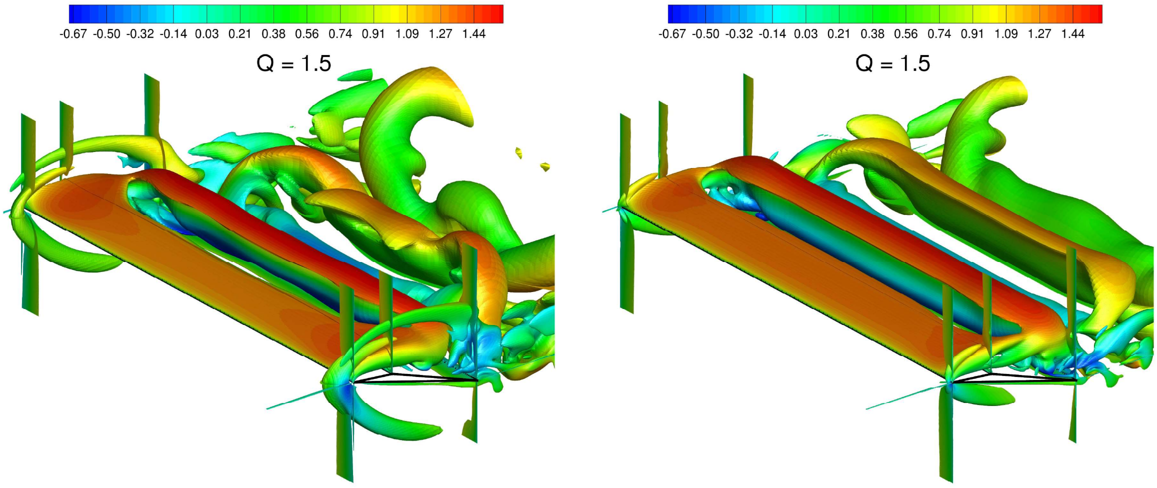

(a) CIRA: M=0.15, Re=3.0×10^3

(b) CIRA: M=0.15, Re=1.0×10^4

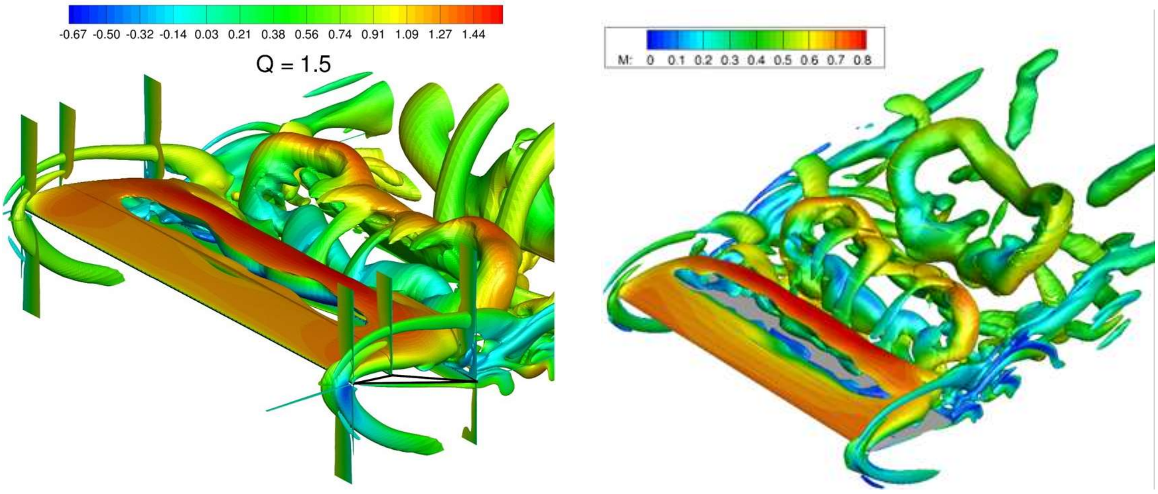

(c) CIRA: M=0.50, Re=3.0×10^3

(d) ONERA ($Q = 1.41$): M=0.50, Re=3.0×10^3

Figure 64: Isosurface of Q at $\alpha = 15°$

presented. In this section, we focus on the application of these approaches for stability analysis and transition prediction of pressure-induced laminar separation bubbles. The objectives of these studies were to further test the applicability of boundary-layer stability analysis tools to laminar boundary-layer flows with recirculation bubbles encompassed and to compare the resulting N-factor data with the transition onset predicted in the corresponding LES simulations. Pressure-induced laminar separation bubbles are typically less challenging from a stability analysis point of view than geometry-induced separation bubbles due to the usually less pronounced streamwise gradients in the flow field data.

In [89] it had been demonstrated for the first time that the PSE methodology is well suited for linear and nonlinear stability analysis of convectively unstable pressure-induced separation bubbles

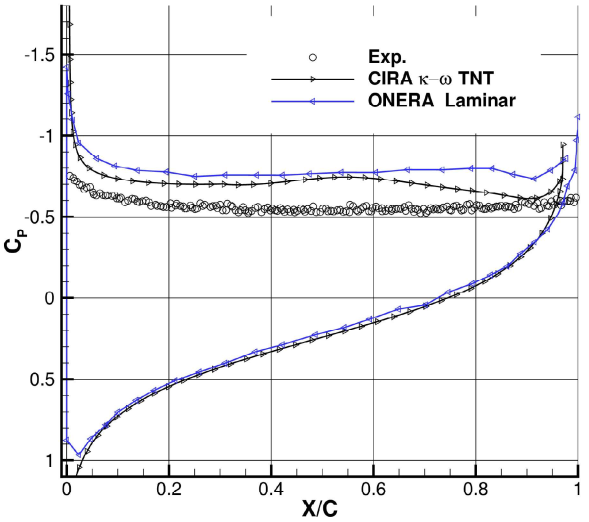

Figure 65: Pressure coefficient at Mach 0.50, Re=3.0×10^3, and $\alpha = 15°$

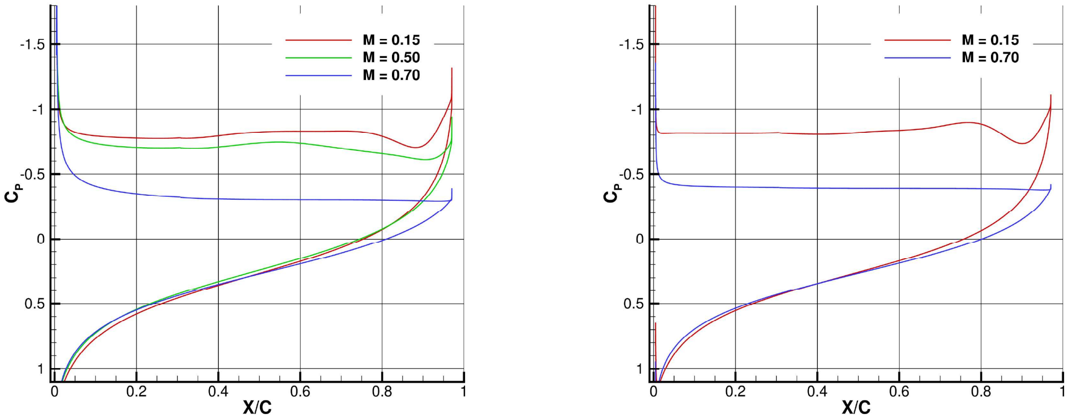

(a) Re = 3.0×10^3 (b) Re = 1.0×10^4

Figure 66: Pressure coefficient at $\alpha = 15°$. Effect of Mach number by the $\kappa - \omega$ TNT turbulence model

with its reverse flow region, despite the PSE are solved by a marching procedure in chord-wise direction. However, the maximum amount of reverse flow was lower than in the test cases considered here. Moreover, in [89] the basic flow used as input for the stability analyses was still laminar in the reattachment region, whereas in the present WP 4 test cases laminar-turbulent transition occurs

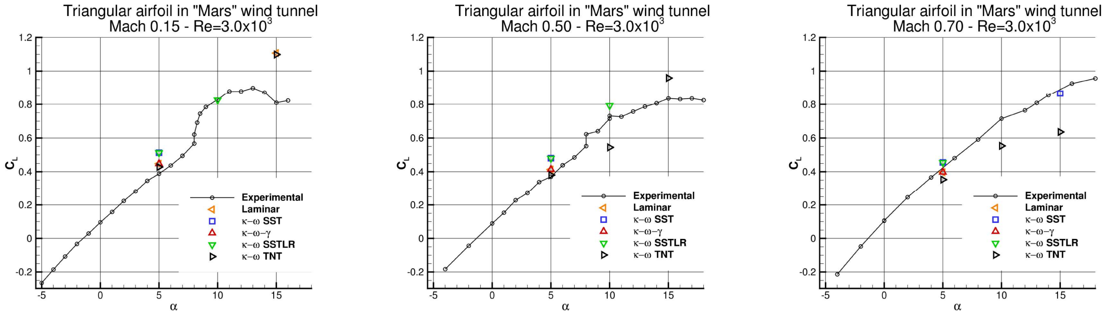

(a) Lift Coefficient - Mach = 0.15 (b) Lift Coefficient - Mach = 0.50 (c) Lift Coefficient - Mach = 0.70

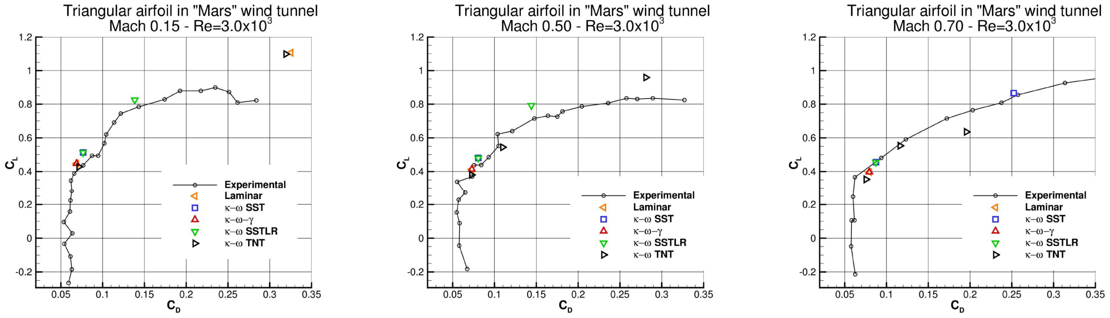

(d) Drag Polar - Mach = 0.15 (e) Drag Polar - Mach = 0.50 (f) Drag Polar - Mach = 0.70

Figure 67: Lift coefficients and drag polars at Reynolds number 3.0×10^3

in the separated flow region prior to the reattachment, i.e. strictly speaking transitional separation bubbles are considered. From a physical point of view, the application of the stability analysis tools should be restricted to the laminar region and not applied to the fully turbulent region in particular, where the basic flow provided corresponds to the time- and spanwise-averaged flow field. Proceeding with the stability analyses well into the transitional flow region nevertheless will be instructive.

Both WP 4 test cases, the SD7003 and the NACA 0015 airfoils, had been considered also in WP 1. The time- and spanwise-averaged flow field data taken as basic flow for the subsequent instability analyses were computed by CIRA using LES and made available to all partners. Further details about those test cases and the numerical approach used by CIRA can be found in [14]. DLR post-processed these time- and spanwise-averaged LES data and made the resulting wall-normal boundary-layer profile data available to all partners in the so-called 'EUROTRANS' format. This data format had been defined within the EU project EUROTRANS. Moreover, it was subsequently used in several other EU projects for the exchange of laminar basic flow data between the partners. Therefore, several IMOLA partners had well-tested interfaces to their own stability analysis tools available already. The EUROTRANS data format contains all relevant information on the boundary-layer profiles including their first/second wall-normal and the first streamwise derivatives together with information about the surface curvature of the airfoil. Hence, it is suitable for both LST- and PSE-based stability analysis of laminar boundary-layer data.

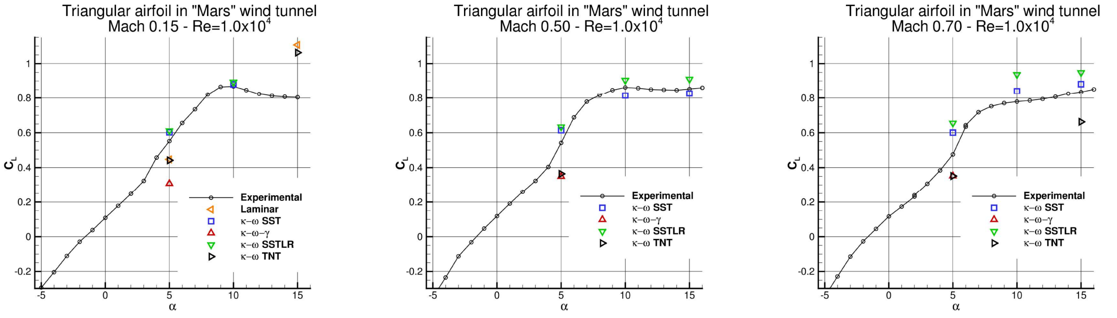

(a) Lift Coefficient - Mach = 0.15 (b) Lift Coefficient - Mach = 0.50 (c) Lift Coefficient - Mach = 0.70

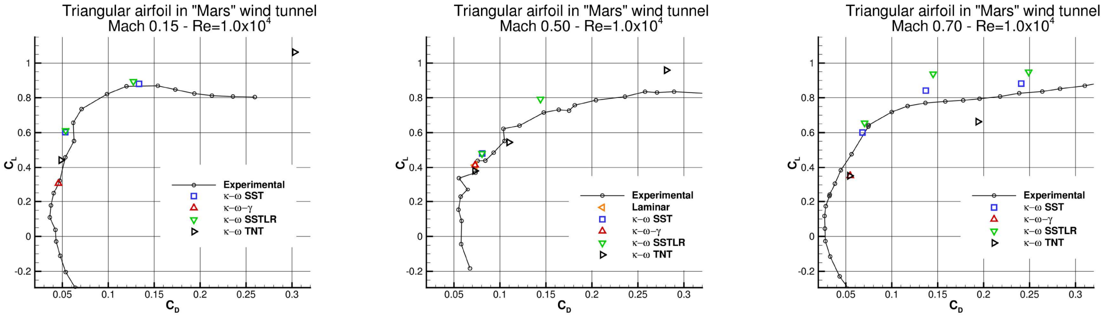

(d) Drag Polar - Mach = 0.15 (e) Drag Polar - Mach = 0.50 (f) Drag Polar - Mach = 0.70

Figure 68: Lift coefficients and drag polars at Reynolds number 1.0×10^4

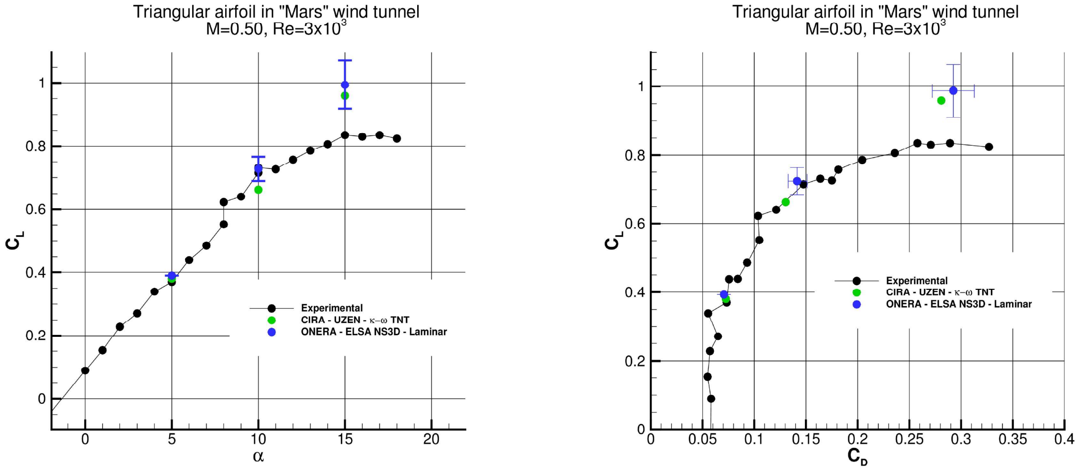

(a) Lift Coefficient (b) Drag Polar

Figure 69: Aerodynamic coefficients at Mach 0.50 and Reynolds 3.0×10^3

4.4.2 SD 7003 airfoil

The freestream conditions chosen for the SD7003 airfoil were $Ma = 0.1$, $Re_\infty = 6.0 \times 10^4$ and $\alpha = 4°$. The time- and spanwise-averaged flow field from the LES of CIRA with the shallow pressure-induced separation bubble is visualized in Fig. 70. Flow separation occurs at $x/c \approx 0.2$, where the boundary layer is still laminar, and then undergoes laminar-turbulent transition further downstream in the separated flow region prior to the reattachment at $x/c \approx 0.6$. The skin-friction coefficient data are shown in Fig. 71 and compared to corresponding results from other numerical approaches (from [14]).

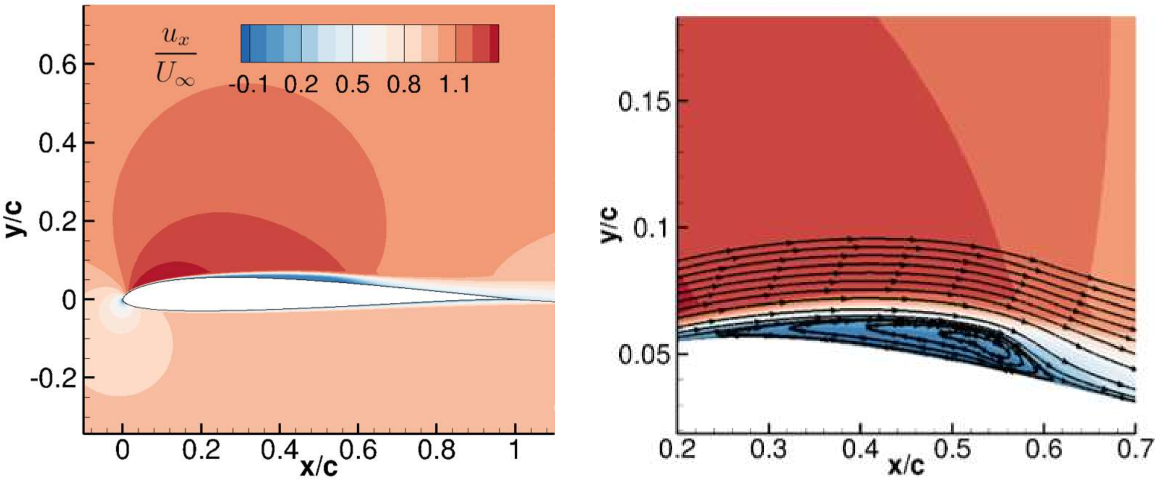

(a) Overview.

(b) Separation bubble region.

Figure 70: Basic flow x-velocity component of the SD7003 airfoil for $Ma = 0.1$, $Re_\infty = 6.0 \times 10^4$ and $\alpha = 4°$.

Figure 72 summarizes the N-factor results obtained by DLR for two-dimensional Tollmien-Schlichting waves of different frequencies f. Figure 72a compares the corresponding N-factor envelope computed by DLR based on LST with that from PSE. The locations of separation and reattachment are marked on the x/c-axis by a red line, respectively. The N-factor data obtained by PSE are based on the total kinetic energy and denoted by N_{tke}. Surface curvature effects were taken into account in the PSE computations, whereas they were neglected in LST in order to be consistent with other assumptions inherent to the LST approach. However, it is well-known that surface curvature effects are negligible for two-dimensional Tollmien-Schlichting waves in two-dimensional basic flows of typical airfoils. For a more detailed discussion on surface curvature effects see section 4.4.3. The LST results are complemented by individual N-factor curves for different frequencies that contribute to the LST-based N-factor envelope, i.e. two-dimensional Tollmien-Schlichting waves with frequencies between $f = 230Hz$ and $f = 600Hz$. Actually, a much wider range of frequencies and also oblique Tollmien-Schlichting waves were considered in the stability analyses, but those modes do not contribute to the N-factor envelope and thus these data are not presented here. Noteworthy is the fact that all modes which could be traced downstream in the stability analysis beyond the reattachment point, i.e. into the region where the time- and spanwise-averaged basic flow provided by LES is no longer laminar, tend to become almost neutrally stable.

Figure 72b compares the envelopes from LST and PSE of Figure 72a with corresponding data

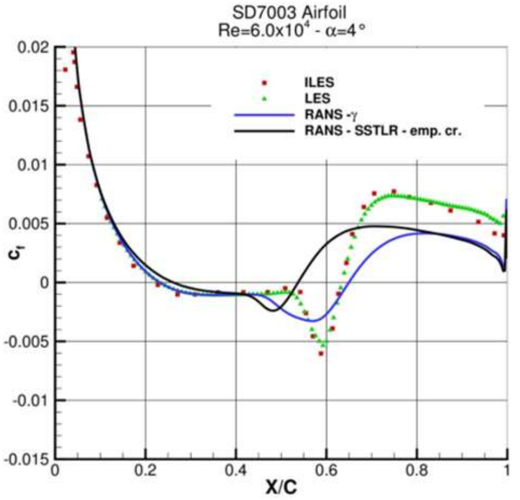

Figure 71: Comparison of the skin-friction coefficients from different numerical approaches for the SD7003 airfoil for $Ma = 0.1$, $Re_\infty = 6.0 \times 10^4$ and $\alpha = 4°$ (from [14]).

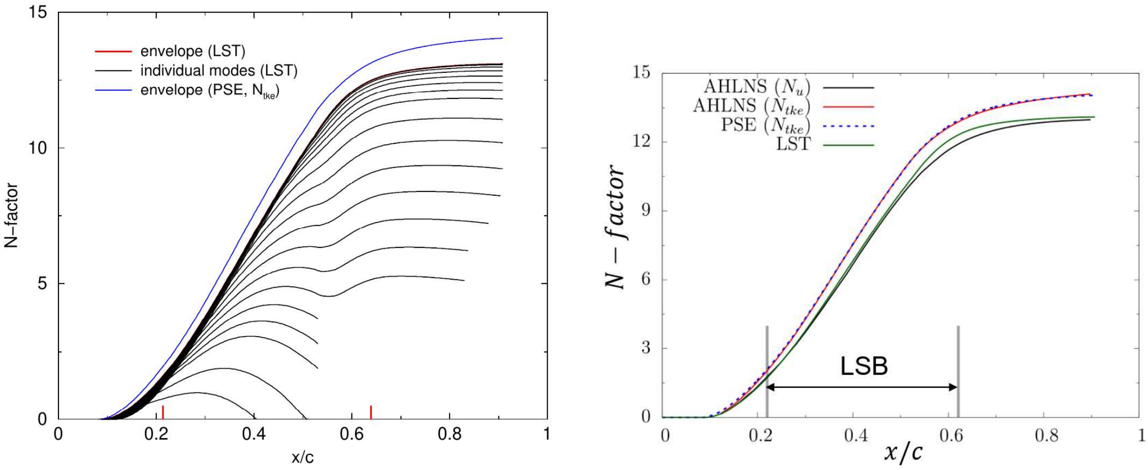

(a) N-factor results from LST and PSE. The x/c-coordinates of separation and reattachment points are marked by the red lines.

(b) Comparison of AHLNS, PSE and LST N-factor envelopes.

Figure 72: DLR's N-factor results for the SD7003 airfoil for $Ma = 0.1$, $Re_\infty = 6.0 \times 10^4$ and $\alpha = 4°$.

from AHLNS based on two different definitions of the N-factor. The AHLNS computations did take into account surface curvature effects. The agreement within line thickness between PSE and AHLNS when using the same definition of the N-factor confirms the findings of [89] that PSE is well suited for the linear stability analysis of convectively unstable laminar separation bubbles and that there is no need to perform more time-consuming AHLNS or linear DNS computations for such configurations. Moreover, the comparison of the AHLNS N-factor results based on total kinetic disturbance energy (N_{tke}) with those using an alternative definition based on the wall-normal maximum of the chordwise disturbance velocity component N_u shows that these differences are of the same order of magnitude as the differences between LST and PSE for such configurations.

Figure 73 shows CIRA's N-factor results for two-dimensional Tollmien-Schlichting waves of various frequencies computed by LST. The N-factor values obtained from CIRA's LST computations are in good agreement with the ones of DLR's LST. Surface curvature effects were not taken into account in both sets of LST computations.

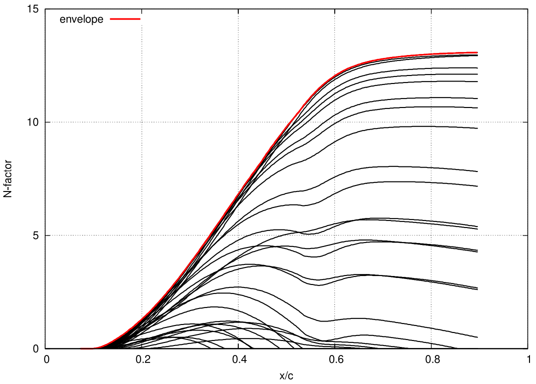

Figure 73: CIRA's N-factor results for the SD7003 airfoil for $Ma = 0.1$, $Re_\infty = 6.0 \times 10^4$ and $\alpha = 4°$.

4.4.3 NACA0015 airfoil

The NACA 0015 airfoil was studied in the incompressible regime at $Re_\infty = 1.8 \times 10^5$ and three different angles of attack, i.e. $\alpha = 3°$, $5°$ and $10°$. The corresponding pressure coefficient distributions and skin-friction coefficient distributions are shown in Fig. 74. The separation bubble located on the suction side of the airfoil is moving upstream with increasing angle of attack. The minimum value in wall-normal direction of the streamwise velocity component at each chord position normalized by the local boundary-layer edge velocity Q_e is plotted in Fig. 75, indicating that the separation bubbles of the present test cases feature a pronounced reverse flow.

Figure 76 summarizes the N-factor results for two-dimensional Tollmien-Schlichting waves of different frequencies f from LST and PSE computations performed by DLR. As in section 4.4.2, surface curvature effects are taken into account in the PSE computations but neglected in the LST computations. The locations of separation and reattachment are marked on the x/c-axis by a red line, respectively, indicating that growth of boundary-layer instabilities sets in upstream of separation bubble in the adverse pressure gradient region and the maximum N-factors are reached close to the location where the time- and spanwise-averaged transitional flow reattaches in CIRA's LES. Similar to the SD 7003 test case of section 4.4.2, the N-factor envelopes tend to level off in the reattachment region, in particular those from the PSE computations. The time- and spanwise-averaged turbulent kinetic energy data κ from the LES computations are shown in Fig. 77. The x/c-locations where the production of κ sets in in the LES computations correlate rather well with the chord positions where N-factor values of about 10 are reached in the stability analyses for the three angles of attack. Note that similar N-factor vales at transition were reached in section 4.4.2 for the SD 7003 test case. Hence, the transition onset as predicted by the models used in CIRA's LES computations are consistent with an N-factor based transition prediction for the test cases considered in WP 4.

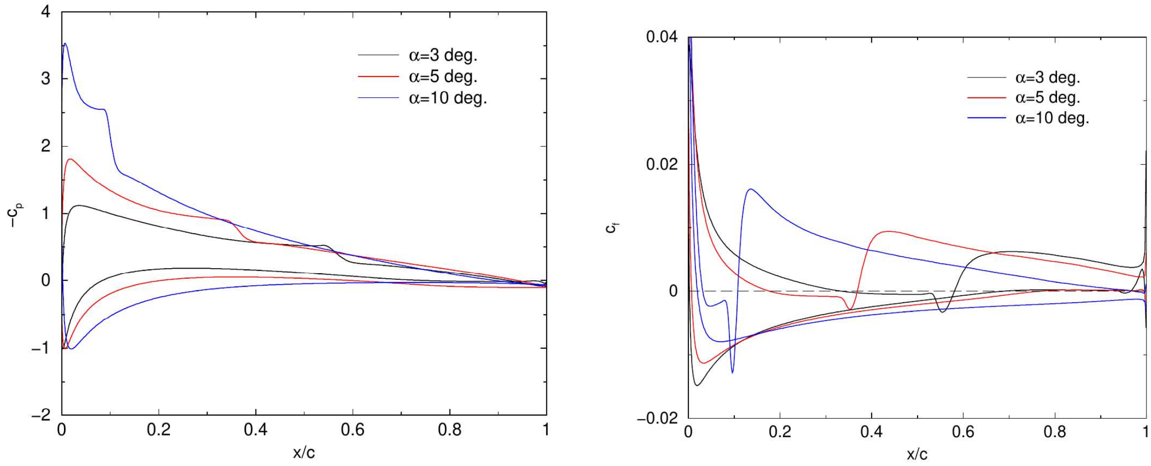

(a) Pressure coefficient.

(b) Skin-friction coefficient.

Figure 74: Pressure and skin-friction coefficients over the NACA 0015 airfoil at $Re_\infty = 1.8 \times 10^5$ and different angles of attack α.

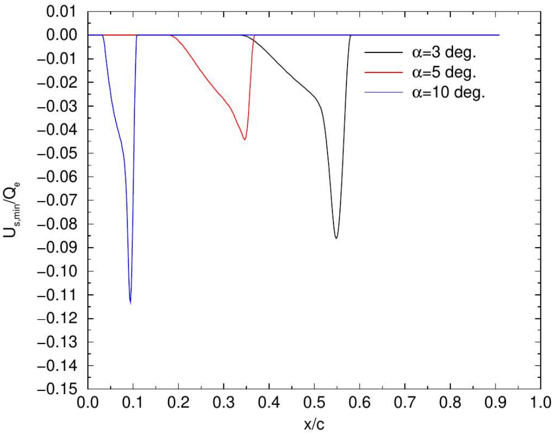

Figure 75: Maximum reverse flow velocity in the transitional separation bubble over the NACA 0015 airfoil at $Re_\infty = 1.8 \times 10^5$ and different angles of attack α.

Figure 78 shows the N-factor results of CIRA for two-dimensional Tollmien-Schlichting waves of various frequencies computed by LST with surface curvature neglected. The envelope of DLR's LST is also superimposed for comparison. The results compare well.

In order to verify that surface curvature effects are indeed irrelevant in the present test case, DLR performed additional LST computations for both two-dimensional and oblique Tollmien-Schlichting waves with surface curvature effects taken into account. The results for a selected two-dimensional and an oblique wave are shown in Fig. 79. As expected, the convex surface curvature of the airfoil is negligible for two-dimensional Tollmien-Schlichting waves and has a slightly stabilizing effect on oblique Tollmien-Schlichting waves only. Since oblique waves do not contribute to the N-factor

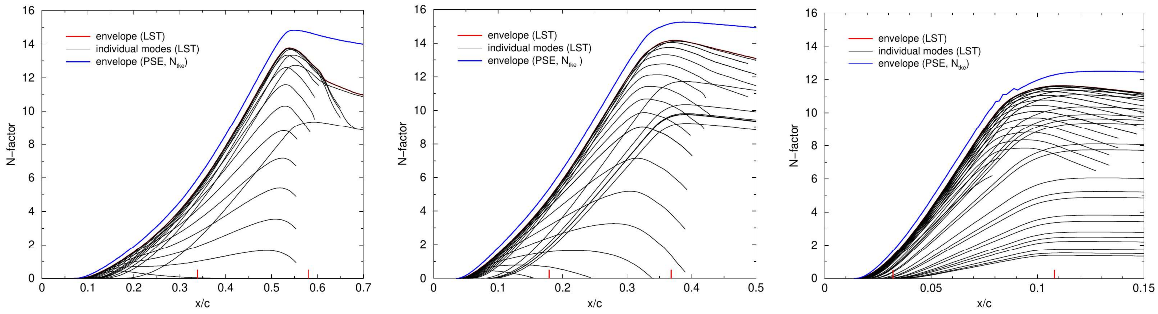

(a) $\alpha = 3°$. (b) $\alpha = 5°$. (c) $\alpha = 10°$.

Figure 76: DLR's N-factor results based on LST without curvature and PSE with curvature for NACA 0015 airfoil at $Re_\infty = 1.8 \times 10^5$ and different angles of attack α.

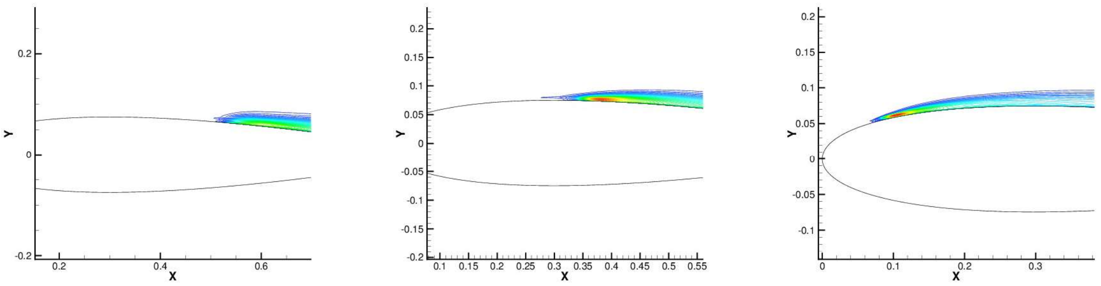

(a) $\alpha = 3°$. (b) $\alpha = 5°$. (c) $\alpha = 10°$.

Figure 77: Isocontours of the time- and spanwise-averaged turbulent kinetic energy κ in CIRA's LES computations for NACA 0015 airfoil at $Re_\infty = 1.8 \times 10^5$ and different angles of attack α.

envelopes, however, the envelopes remain unaffected in practice.

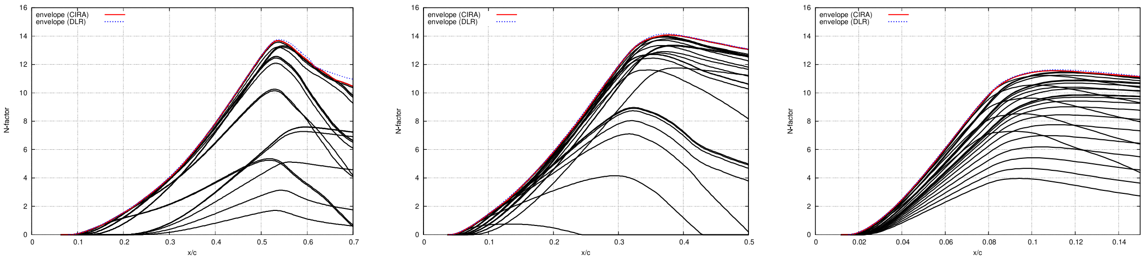

(a) $\alpha = 3°$. (b) $\alpha = 5°$. (c) $\alpha = 10°$.

Figure 78: CIRA's N-factor results based on LST for the NACA 0015 airfoil at $Re_\infty = 1.8 \times 10^5$ and different angles of attack α.

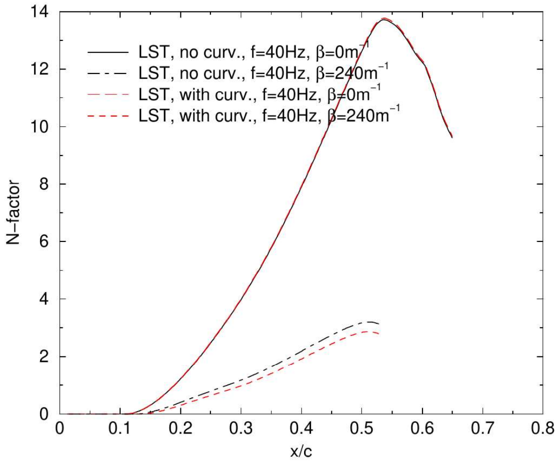

Figure 79: Comparison of DLR's N-factor results based on LST without and with surface curvature for a selected 2D Tollmien-Schlichting wave of $f = 40Hz$ and an oblique wave with a spanwise wavenumber $\beta = 240m^{-1}$, respectively, for the NACA 0015 airfoil case at $Re_\infty = 1.8 \times 10^5$ and $\alpha = 3°$.

5 Conclusions

The action group 59 of the GARTEUR association started its activities in February 2019 with the main aim of improving the numerical modelling of laminar separation bubbles. The focus has been placed on RANS methods and turbulence modelling. Several test cases covering laminar separation bubbles at low and high Reynolds numbers and also in the compressible flow regime have been considered.

The importance of employing turbulence models making use of transition functions (γ, and/or Re_Θ) has been highlighted. Interesting approaches based on functions for the boost of the turbulent kinetic energy have been proposed. Good results have been achieved by employing the Spalart-Allmaras model with transition functions, especially the version modified for decreasing the destruction term of the model. This has as a consequence the enhancement of the skin friction levels in the recovery region of the flow. The same effect can be obtained by a function that multiplies the production term of the kinetic turbulence equation as shown by the $\kappa - \omega$ LSST model. A function for the boost of the turbulent kinetic energy has also been coupled to the transition $\kappa - \omega$ SST model retrieving the beneficial effect of a transition function and, at the same time, ensuring the enhancement of the friction levels. These remarks apply to the laminar bubbles analyzed at low Reynolds numbers. At high Reynolds number the use of transition functions has allowed to obtain satisfactory results in good agreement with the experimental data.

The study of laminar separation bubbles in the compressible regime has evidenced the same issues encountered by the numerical methods for incompressible flows. In fact, the main troubles are related to the reproduction of the bubbles and of separated regions. The Mach number does not critically influence the flow field. It seems, on the contrary, that the increase of Mach energizes the flow that is more able to withstand with the adverse pressure gradients and becomes less prone to the separation. It is worth noting that this regime is of particular interest for the flight in the Martian atmosphere whose conditions of low pressure, density, and temperatures produce flight conditions characterized by very low Reynolds numbers, about 2% of those on the Earth, in combination with high Mach numbers, about 1.5 times higher than the terrestrial ones.

A further work package has been devoted to explore the use of instability analysis methods for pressure-induced laminar separation bubbles and to assess their capability for predicting the transition. The methods have been applied to two airfoils also in the turbulent flow region. LES data have been used as basic flow. It has been shown that the PSE methodology is well suited for the linear stability analysis of convectively unstable LSBs. The N-factor envelope curves by PSE well compare with the more expensive AHLNS ones. The N-factor based prediction of the transition is consistent with the field of the turbulent kinetic energy coming from the large eddy simulations. The N-factor envelopes reach a maximum close to the reattachment point (averaged in time and space) where in the LES the turbulent kinetic energy starts to increase and tend to become neutrally stable downstream.

References

[1] Carmichael, B. H., "Low Reynolds Number Airfoil Survey," Tech. Report NASA-CR-165803, NASA, 1981.

[2] Catalano, P. and Tognaccini, R., "Turbulence modeling for low-Reynolds-number flows," *AIAA Journal*, Vol. 48, No. 8, 2010, pp. 1673–1685.

[3] Catalano, P. and Tognaccini, R., "Numerical analysis of the flow around the SD7003 airfoil," *48th AIAA Aerospace Sciences Meeting*, 2010.

[4] Catalano, P. and Tognaccini, R., "RANS analysis of the low-Reynolds number flow around the SD7003 airfoil," *Aerospace Science and Technology*, Vol. 15, No. 8, 2011, pp. 615 – 626.

[5] Catalano, P., Mele, B., and Tognaccini, R., "A numerical method to detect laminar separation bubbles over airfoils," *31st AIAA Applied Aerodynamics Conference*, 2013.

[6] Menter, F. R., Smirnov, P. E., Liu, T., and Avancha, R., "A One-Equation Local Correlation-Based Transition Model," *Flow, Turbulence and Combustion*, Vol. 95, No. 4, 2015, pp. 583–619.

[7] Catalano, P. and Amato, M., "An evaluation of RANS turbulence modelling for aerodynamic applications," *Aerospace Science and Technology*, Vol. 7, No. 7, 2003, pp. 493–509.

[8] Catalano, P., Mele, B., and Tognaccini, R., "On the implementation of a turbulence model for low Reynolds number flows," *Computers and Fluids*, Vol. 109, 2015, pp. 67–71.

[9] Langtry, R. and Menter, F., "Transition Modeling for General CFD Applications in Aeronautics," *43rd AIAA Aerospace Sciences Meeting and Exhibit*, American Institute of Aeronautics and Astronautics (AIAA), jan 2005.

[10] Langtry, R. B. and Menter, F. R., "Correlation-Based Transition Modeling for Unstructured Parallelized Computational Fluid Dynamics Codes," *AIAA Journal*, Vol. 47, No. 12, Dec 2009, pp. 2894–2906.

[11] Colonia, S., Leble, V., Steijl, R., and Barakos, G., "Calibration of the γ-Equation Transition Model for High Reynolds Flows at Low Mach," *Journal of Physics: Conference Series*, Vol. 753, 2016.

[12] Colonia, S., Leble, V., Steijl, R., and Barakos, G., "Assessment & calibration of the γ-equation transition model at low Mach," *AIAA Journal*, Vol. 55, No. 4, 2017.

[13] Menter, F. R., "Two-equation eddy-viscosity turbulence models for engineering applications," *AIAA Journal*, Vol. 32, No. 8, aug 1994, pp. 1598–1605.

[14] Catalano, P. and de Rosa, D., "Large Eddy Simulations and RANS models for airfoils at low Reynolds number." *AIAA 2020 Aviation Forum*, June 15 –June 19 2020, AIAA paper 2020-2990.

[15] Bernardos, L., Richez, F., Gleize, V., and Gerolymos, G., "Prediction of Separation-Induced Transition on the SD7003 Airfoil Using Algebraic Transition Triggering," *AIAA Journal*, Vol. 57, No. 9, 2019, https://doi.org/10.2514/1.J058288.

[16] De Santis, C., Catalano, P., and Tognaccini, R., "Model for Enhancing Turbulent Production in Laminar Separation Bubbles," *AIAA Journal*, Vol. 60, No. 1, jan 2022, pp. 473–487.

[17] Del Álamo, J. C. and Jiménez, J., "Estimation of Turbulent Convection Velocities and Corrections to Taylor's Approximation," *Journal of Fluid Mechanics*, Vol. 640, 2009, pp. 5–26.

[18] Miozzi, M., Di Felice, F., Klein, C., and Costantini, M., "Taylor Hypothesis Applied to Direct Measurement of Skin Friction Using Data From Temperature Sensitive Paint," *Experimental Thermal and Fluid Science*, Vol. 110, 2020, pp. 109913.

[19] Eckelmann, H., "The Structure of the Viscous Sublayer and the Adjacent Wall Region in a Turbulent Channel Flow," *Journal of Fluid Mechanics*, Vol. 65, No. 3, 1974, pp. 439–459.

[20] Kim, J. and Hussain, F., "Propagation Velocity of Perturbations in Turbulent Channel Flow," *Physics of Fluids A*, Vol. 5, No. 3, 1993, pp. 695–706.

[21] Hetsroni, G., Tiselj, I., Bergant, R., Mosyak, A., and Pogrebnyak, E., "Convection Velocity of Temperature Fluctuations in a Turbulent Flume," *Journal of Heat Transfer*, Vol. 126, No. 5, 2004, pp. 843–848.

[22] Liu, T., Sullivan, J. P., Asai, K., Klein, C., and Egami, Y., *Pressure and Temperature Sensitive Paints*, Springer International Publishing, Cham, 2021.

[23] Ondrus, V., Meier, R., Klein, C., Henne, U., Schäferling, M., and Beifuss, U., "Europium 1,3-di(thienyl)propane-1,3-diones with Outstanding Properties for Temperature Sensing," *Sensors and Actuators A: Physical*, Vol. 233, 2015, pp. 434–441.

[24] Bitter, M., Hilfer, M., Schubert, T., Klein, C., and Niehuis, R., "An Ultra-Fast TSP on a CNT Heating Layer for Unsteady Temperature and Heat Flux Measurements in Subsonic Flows," *Sensors*, Vol. 22, No. 2, 2022.

[25] Miozzi, M., Capone, A., Costantini, M., Fratto, L., Klein, C., and Di Felice, F., "Skin Friction and Coherent Structures Within a Laminar Separation Bubble," *Experiments in Fluids*, Vol. 60, 2019, pp. 13.

[26] Herbert, T., "Parabolized stability equations," *Annual Review of Fluid Mechanics*, Vol. 29, No. 1, 1997, pp. 245–283.

[27] Hein, S., Bertolotti, F., Simen, M., Hanifi, A., and Henningson, D., "Linear nonlocal instability analysis - the linear NOLOT code," Tech. Rep. IB 223-94 A56, DLR, 1995.

[28] Franco Sumariva, J. A. and Hein, S. J., "Adaptive Harmonic Linearized Navier-Stokes equations used for boundary layer instability analysis in the presence of large streamwise gradients," *2018 AIAA Aerospace Sciences Meeting*, American Institute of Aeronautics and Astronautics, Reston, Virginia, jan 2018.

[29] Fischer, P., Lottes, J., and Kerkemeier, S., "Nek5000 web page," `http://nek5000.mcs.anl.gov`, 2008.

[30] Nenni, J. P. and Gluyas, G. L., "Aerodynamic design and analysis of an LFC surface," *Astronautics & Aeronautics*, Vol. 4, No. 7, 1966, pp. 52–57.

[31] Franco, J. A. and Hein, S., "Numerical Studies on the Influence of Step-Like Surface Irregularities on the Development of Tollmien-Schlichting Waves," *IUTAM Laminar-Turbulent Transition*, edited by S. Sherwin, P. Schmid, and X. Wu, Springer International Publishing, Cham, 2022, pp. 737–748.

[32] Franco, J. A., Hein, S., and Valero, E., "On the influence of two-dimensional hump roughness on laminar–turbulent transition," *Physics of Fluids*, Vol. 32, No. 034102, 2020.

[33] Tocci, F., Franco, J. A., Hein, S., Chauvat, G., and Hanifi, A., "The Effect of 2-D Surface Irregularities on Laminar-Turbulent Transition: A Comparison of Numerical Methodologies," *New Results in Numerical and Experimental Fluid Mechanics XIII*, edited by A. Dillmann, G. Heller, E. Krämer, and C. Wagner, Springer International Publishing, Cham, 2021, pp. 246–256.

[34] Tocci, F., Chauvat, G., Hein, S., and Hanifi, A., "Direct Numerical Simulations of Tollmien-Schlichting Disturbances in the Presence of Surface Irregularities," *IUTAM Laminar-Turbulent Transition*, edited by S. Sherwin, P. Schmid, and X. Wu, Springer International Publishing, Cham, 2022, pp. 805–814.

[35] Bernardos, L., Richez, F., Gleize, V., and Gerolymos, G. A., "Algebraic Nonlocal Transition Modeling of Laminar Separation Bubbles using k-ω Turbulence Models," *AIAA Journal*, Vol. 57, No. 2, Feb. 2019, pp. 553–565.

[36] Cambier, L., Heib, S., and Plot, S., "The Onera elsA CFD software: input from research and feedback from industry," *Mechanics & Industry*, Vol. 14, No. 3, 2013, pp. 159–174.

[37] Wilcox, D. C., "Formulation of the k-ω Turbulence Model Revisited," *AIAA Journal*, Vol. 46, No. 11, November 2008, pp. 2823–2838.

[38] Menter, F., Langtry, R., Likki, S., Suzen, Y., Huang, P., and Volker, S., "A correlation-based transition model using local variables - Part 1: Model formulation," *J Turbomach*, Vol. 128, No. 3, 2006, pp. 413–422.

[39] Medida, S. and Baeder, J., "Application of the Correlation–based γ–$\widetilde{\mathrm{Re}_{\theta,t}}$ transition model to the Spalart–Allmaras turbulence model," Honolulu, HI, June, 2011 2011.

[40] Malan, P., Suluksna, K., and Juntasaro, E., "Calibrating γ–$\widetilde{\mathrm{Re}_{\theta,t}}$ Transition Model for Commercial CFD," *47th AIAA Aerospace Sciences Metting*, Orlando, FL, January 5–8 2009.

[41] Spalart, P.R. and Allmaras, S.R., "A one-equation turbulent model for aerodynamic flows," *La Recherche Aérospatiale*, Vol. 1, 1994, pp. 5–21.

[42] Spalart, P. R. and Garbaruk, A. V., "Correction to the Spalart–Allmaras Turbulence Model, Providing More Accurate Skin Friction," *AIAA Journal*, Vol. 58, No. 5, 2020, pp. 1903–1905.

[43] Ilinca, F. and Pelletier, D., "Positivity preservation and adaptive solution of two-equation models of turbulence," *International Journal of Thermal Sciences*, Vol. 38, No. 7, 1999, pp. 560 – 571.

[44] Kang L. and Yue W. and Wen-Ping S. and Zhong-Hua H., "A two–equation local–correlation–based laminar–turbulent transition modeling scheme for external aerodynamics," *Aerospace Science and Technology*, Vol. 106, 2020, pp. 106128.

[45] Hoarau, Y., Pena, D., Vos, J. B., Charbonnier, D., Gehri, A., Braza, M., Deloze, T., and Laurendeau, E., "Recent Developments of the Navier Stokes Multi Block (NSMB) CFD solver," *54th AIAA Aerospace Sciences Meeting*, 2016.

[46] Vos, J. B., Charbonnier, D., Ludwig, T., Merazzi, S., Gehri, A., and Stephani, P., "Recent Developments on Fluid Structure Interaction Using the Navier Stokes Multi Block (NSMB) CFD Solver," *35th AIAA Applied Aerodynamics Conference*, American Institute of Aeronautics and Astronautics, June 2017.

[47] Hoarau, Y., *Analyse physique par simulation numérique et modélisation des écoulements décollés instationnaires autour de surfaces portantes*, Ph.D. thesis, Toulouse, France, 2002, Thèse de doctorat dirigée par Braza, Marianna Dynamique des fluides.

[48] Martinat, G., Braza, M., Hoarau, Y., and Harran, G., "Turbulence modelling of the flow past a pitching NACA0012 airfoil at and Reynolds numbers," *Journal of Fluids and Structures*, Vol. 24, No. 8, nov 2008, pp. 1294–1303.

[49] Barbut, G., Braza, M., Hoarau, Y., Barakos, G., Sévrain, A., and Vos, J. B., "Prediction of Transonic Buffet around a Wing with Flap," *Progress in Hybrid RANS-LES Modelling*, Springer Berlin Heidelberg, 2010, pp. 191–204.

[50] Grossi, F., Braza, M., and Hoarau, Y., "Prediction of Transonic Buffet by Delayed Detached-Eddy Simulation," *AIAA Journal*, Vol. 52, No. 10, oct 2014, pp. 2300–2312.

[51] Bourguet, R., Braza, M., Harran, G., and Akoury, R. E., "Anisotropic Organised Eddy Simulation for the prediction of non-equilibrium turbulent flows around bodies," *Journal of Fluids and Structures*, Vol. 24, No. 8, 2008, pp. 1240–1251.

[52] Marouf, A., Tekap, Y. B., Simiriotis, N., Tô, J.-B., Rouchon, J.-F., Hoarau, Y., and Braza, M., "Numerical investigation of frequency-amplitude effects of dynamic morphing for a high-lift configuration at high Reynolds number," *International Journal of Numerical Methods for Heat & Fluid Flow*, Vol. 31, No. 2, Jan. 2020, pp. 599–617.

[53] Simiriotis, N., Jodin, G., Marouf, A., Elyakime, P., Hoarau, Y., Hunt, J., Rouchon, J., and Braza, M., "Morphing of a supercritical wing by means of trailing edge deformation and vibration at high Reynolds numbers: Experimental and numerical investigation," *Journal of Fluids and Structures*, Vol. 91, Nov. 2019, pp. 102676.

[54] Tô, J.-B., Simiriotis, N., Marouf, A., Szubert, D., Asproulias, I., Zilli, D., Hoarau, Y., Hunt, J., and Braza, M., "Effects of vibrating and deformed trailing edge of a morphing supercritical airfoil in transonic regime by numerical simulation at high Reynolds number," *Journal of Fluids and Structures*, Vol. 91, Nov. 2019, pp. 102595.

[55] Truong, H. D., Marouf, A., Chouippe, A., Hoarau, Y., Charbonnier, D., Gehri, A., and Vos, J. B., "Flow analysis around a VTOL aircraft near stall conditions and application of Active Flow Control to enhance the aerodynamic performances at real flight conditions," *AIAA AVIATION 2022 Forum*, American Institute of Aeronautics and Astronautics, June 2022.

[56] Donea, J., Giuliani, S., and Halleux, J., "An arbitrary lagrangian-eulerian finite element method for transient dynamic fluid-structure interactions," *Computer Methods in Applied Mechanics and Engineering*, Vol. 33, No. 1-3, sep 1982, pp. 689–723.

[57] Spalart and Allmaras, "A one-equation turbulence model for aerodynamic flows," American Institute of Aeronautics and Astronautics, 1992.

[58] Menter, F., "Zonal Two Equation k-w Turbulence Models For Aerodynamic Flows," *23rd Fluid Dynamics, Plasmadynamics, and Lasers Conference*, American Institute of Aeronautics and Astronautics, July 1993.

[59] Cakmakcioglu, S. C., Bas, O., Mura, R., and Kaynak, U., "A Revised One-Equation Transitional Model for External Aerodynamics," *AIAA AVIATION 2020 FORUM*, American Institute of Aeronautics and Astronautics, June 2020.

[60] Menter, F. R., Smirnov, P. E., Liu, T., and Avancha, R., "A One-Equation Local Correlation-Based Transition Model," *Flow, Turbulence and Combustion*, Vol. 95, No. 4, 2015, pp. 583–619.

[61] Langtry, R. and Menter, F., "Transition Modeling for General CFD Applications in Aeronautics," *43rd AIAA Aerospace Sciences Meeting and Exhibit*, AIAA, American Insitute of Aeronautics and Astronautics, Reno, Nevada, USA, Jan. 2005.

[62] Xiao, H. and Cinnella, P., "Quantification of model uncertainty in RANS simulations: A review," *Progress in Aerospace Sciences*, Vol. 108, 2019, pp. 1–31.

[63] Duraisamy, K., Iaccarino, G., and Xiao, H., "Turbulence modeling in the age of data," *Annual Review of Fluid Mechanics*, Vol. 51, 2019, pp. 357–377.

[64] Mishra, A. A., Mukhopadhaya, J., Iaccarino, G., and Alonso, J., "Uncertainty estimation module for turbulence model predictions in SU2," *AIAA Journal*, Vol. 57, No. 3, 2019, pp. 1066–1077.

[65] Iaccarino, G., Mishra, A. A., and Ghili, S., "Eigenspace perturbations for uncertainty estimation of single-point turbulence closures," *Physical Review Fluids*, Vol. 2, No. 2, 2017, pp. 024605.

[66] Launder, B., Tselepidakis, D., and Younis, B., "A second-moment closure study of rotating channel flow," *Journal of Fluid Mechanics*, Vol. 183, 1987, pp. 63–75.

[67] Speziale, C. G., "On nonlinear kl and k-ε models of turbulence," *Journal of Fluid Mechanics*, Vol. 178, 1987, pp. 459–475.

[68] Emory, M., Larsson, J., and Iaccarino, G., "Modeling of structural uncertainties in Reynolds-averaged Navier-Stokes closures," *Physics of Fluids*, Vol. 25, No. 11, 2013, pp. 110822.

[69] Banerjee, S., Krahl, R., Durst, F., and Zenger, C., "Presentation of anisotropy properties of turbulence, invariants versus eigenvalue approaches," *Journal of Turbulence*, , No. 8, 2007, pp. N32.

[70] Armaly, B. F., Durst, F., Pereira, J. C. F., and Schönung, B., "Experimental and theoretical investigation of backward-facing step flow," *Journal of Fluid Mechanics*, Vol. 127, No. -1, feb 1983, pp. 473.

[71] Galbraith, M. C. and M. R. Visbal, "Implicit Large Eddy Simulation of Low Reynolds Number Flow past the SD 7003 Airfoil," 46^{th} *AIAA Aerospace Sciences Meeting and Exhibit*, Jan. 7 –Jan. 10 2008, AIAA paper 2008-225.

[72] Galbraith, M. C. and Visbal, M. R., "Implicit Large Eddy Simulation of Low-Reynolds-Number Transitional Flow Past the SD7003 Airfoil," *40th Fluid Dynamics Conference and Exhibit*, AIAA, Chicago, Illinois, USA, July 2010.

[73] Selig, M. S., Donovan, J. F., and Fraser, D. B., "Airfoils at Low Speeds," *Soartech 8*, H. A. Stokely, Soartech publications, Virginia Beach, VA, USA, 1989.

[74] Selig, M. S., Guglielmo, J. J., Groeren, A. P., and Giguere, P., "Summary of Low-Speed Airfoil Data," H. A. Stokely, Soartech Aero publications, Virginia Beach, VA, USA, 1995.

[75] McGhee, R., Walker, B., and Millard, B., "Experimental Results for Eppler 387 Airfoil at low Re numbers in Langley Low Turbulence pressure tunnel," Tech. Rep. TM 4062, NASA, 1988.

[76] Miozzi, M., Di Felice, F., Klein, C., and Costantini, M., "Taylor hypothesis applied to direct measurement of skin friction using data from Temperature Sensitive Paint," *Experimental Thermal and Fluid Science*, Vol. 110, 2020.

[77] Miozzi, M., Di Felice, F., Klein, C., and Costantini, M., "Taylor hypothesis applied to direct measurement of skin friction using data from Temperature Sensitive Paint," *Experimental Thermal and Fluid Science*, Vol. 110, 1 2020, https://doi.org/10.1016/j.expthermflusci.2019.109913.

[78] Miozzi, M., Capone, A., Costantini, M., Fratto, L. Klein, C., and Di Felice, F., "Skin friction and coherent structures within a laminar separation bubble," *Experiments in Fluids*, Vol. 60, 2019, https://doi.org/10.1007/s00348-018-2651-8.

[79] Laurent, C., Mary, I., Gleize, V., Lerat, A., and Arnal, D., "DNS database of a transitional separation bubble on a flat plate and application to RANS modeling validation," *Computers & Fluids*, Vol. 61, May 2012, pp. 21–30.

[80] Richez, F., *Simulation et Modélisation de la Transition par Bulbe de Décollement Laminaire. Application au Décrochage Dynamique*, Ph.D. thesis, Université Paris 13, 2008.

[81] Richez, F., Mary, I., Gleize, V., and Basdevant, C., "Near stall simulation of the flow around an airfoil using zonal RANS/LES coupling method," *Computers & Fluids*, Vol. 37, No. 7, 2008, pp. 857 – 866.

[82] Richez, F., Mary, I., Gleize, V., and Basdevant, C., *Simulation and Modelling of a Laminar Separation Bubble on Airfoils*, Springer Netherlands, Dordrecht, 2009, pp. 457–469.

[83] Bernardos, L., *Modélisation de la transition vers la turbulence d'une couche limite décollée*, Ph.D. thesis, Sorbonne Université, Paris, France, Oct. 2019.

[84] Somers, D. M., "Design and Experimental Results for the S809 Airfoil," Tech. Rep. NREL/SR-440-6918, National Renewable Energy Laboratory, Golden, Colorado, USA, January 1997.

[85] Koning, W. J. F., Romander, E. A., and Johnson, W., "Optimization of Low Reynolds Number Airfoils for Martian Rotor Applications Using an Evolutionary Algorithm." *AIAA 2020 Scitech Forum*, Orlando, FL, Jan. 6 –Jan. 20 – 2020, AIAA paper 2020-0084.

[86] Anyoji, M., Nose, K., Ida, S., Numata, D., Nagai, H., and Asai, K., "Low Reynolds Number Airfoil Testing in a Mars Wind Tunnel," 40th *Fluid Dynamics Conference and Exhibit*, Chicago, Illinois, June 28 –July 1 – 2010, AIAA paper 2010-4627.

[87] Anyoji, M., Numata, D., Nagai, H., and Asai, K., "Effects of Mach Number and Specific Heat Ratio on Low-Reynolds-Number Airfoil Flows," *AIAA Journal*, Vol. 53, No. 6, June 2015, pp. 1640–1654.

[88] Munday, P., Taira, K., Suwa, T., Numata, D., and Asai, K., "Nonlinear Lift on a Triangular Airfoil in Low-Reynolds-Number Compressible Flow," *Journal of Aircraft*, Vol. 55, No. 3, May 2015.

[89] Hein, S., "Linear and Nonlinear Nonlocal Instability Analyses for Two–Dimensional Laminar Separation Bubbles," *Laminar–Turbulent Transition*, edited by H. F. Fasel and W. S. Saric, Springer Verlag, Berlin Heidelberg New York, 2000, pp. 681–686.